Alma Mater Studiorum · University of Bologna

School of Science
Department of Physics and Astronomy
Master Degree in Physics

Particle Tracking in the DUNE-SAND detector: an Extended Kalman Filter approach

Supervisor:

Dr. Gabriele Sirri

Co-Supervisor:

Dr. Valerio Pia
Dr. Michele Pozzato
Dr. Matteo Tenti

Submitted by:

Giulia Lupi

Academic Year 2023/2024

Contents

Introduction **1**

1 Neutrino Physics **3**

1.1 Neutrino in the Standard Model 3

1.2 Dirac vs. Majorana theories 6

1.3 Oscillation's probability 8

1.3.1 Two-family neutrino mixing 13

1.3.2 Three-family neutrino mixing 14

1.3.3 CP violation 16

1.4 MSW Effect 19

1.4.1 Two-family neutrino mixing in matter 20

1.4.2 Matter-Antimatter asymmetry 24

1.5 State of the art 25

1.6 Mass Ordering 31

2 DUNE **35**

2.1 DUNE Design 36

2.1.1 Neutrino beam 36

2.1.2 Near Detector 36

2.1.3 Far Detector 40

2.2 Physics Program 43

2.2.1 Standard neutrino oscillation 43

3 SAND **46**

3.1 Design 46

3.1.1 Magnet 46

3.1.2 ECAL 47

3.1.3 Straw Tube Tracker 48

3.2 Physics program 51

3.2.1 Systematics uncertainties constrains 52

3.2.2 Searches for New Physics 53

4 An Extended Kalman Filter for SAND **54**
4.1 The Kalman Filter algorithm 55
4.2 KF implementation for SAND 58
4.2.1 Trajectory model in a magnetic field 59
4.2.2 Energy loss 61
4.2.3 System Equation 62
4.2.4 Measurement prediction 64
4.3 Test and Validation 65
4.3.1 Standard consistency checks 65
4.3.2 Lossless trajectory model 66
4.3.3 Energy loss and Multiple Coulomb Scattering 67
4.3.4 Complete trajectory model 69

5 Reconstruction of ν_μ CC events in the target/tracker **72**
5.1 Simulation Framework 72
5.1.1 Flux spectrum 73
5.1.2 Geometry 73
5.1.3 Neutrino event generation and particle propagation 74
5.1.4 Digitization 75
5.2 Trajectory reconstruction 76
5.2.1 Position and angle reconstruction 77
5.2.2 Momentum reconstruction 78
5.3 Vertex reconstruction 79
5.4 Future Prospects 80

Conclusion **80**

A Results for π^+ and p **87**

Bibliography **90**

Introduction

The intricate journey of understanding neutrino physics spans pivotal moments in history, tracing its roots to the groundbreaking theorization by W. Pauli in 1930. The landscape of neutrino physics witnessed a transformative shift in 1998 when B.Pontecorvo proposed the theory of neutrino oscillations, providing the compelling evidence that neutrinos have small but non-zero masses and that arise from the mixing of mass and flavour eigenstates. The field of neutrino physics has seen rapid advancements, largely due to the measurements of neutrino oscillations parameters. Next generation experiments are dedicated to address the unresolved questions surrounding the nature of neutrinos. Their objectives include precise determination of oscillation parameters, comprehension of neutrino mass nature, assessment of potential CP violation in the leptonic sector, and establishment of the neutrino mass ordering.

The Deep Underground Neutrino Experiment (DUNE), currently being built, is emerging as one of the main references in neutrino research aiming to achieve the sensitivity required to address these open questions. DUNE will be a dual-site experiment featuring the most powerful neutrino beam at Fermilab (US) and will consists of a Far Detector (FD) and a Near Detector (ND). The FD, situated 1300 km away from the ND, will utilize four 17 kTon Liquid-Argon Time Projection Chambers (LAr-TPCs) to perform precise measurements of neutrino oscillations. The ND, located a few hundred meters from the beam source, comprises three distinct detectors. Its primary objectives are to constrain systematic uncertainties for FD analyses and to search for new physics, including light-dark matter and heavy neutrinos. The Near Detector is therefore essential in assessing the precision needed to achieve DUNE objectives, providing corrections for extrapolating the beam to the FD site, measuring -Ar cross-sections, and modelling nuclear effects.

The SAND (System for on-Axis Neutrino Detection) apparatus is one of the ND components, serving as the primary beam monitor for the DUNE experiment. It is a magnetized detector equipped with a high-resolution tracker to measure particle momentum and a high-performance electromagnetic calorimeter. SAND will also include various targets to study neutrino interactions on different nuclei, including a ~ 1 ton liquid argon cryostat called GRAIN (GRanular Argon for Interaction of Neutrinos) to enable direct comparison with the Far Detector.

The purpose of this thesis is to develop a comprehensive track reconstruction algorithm based on the Extended Kalman filter approach and evaluate its performance in reconstructing ν_μ-CC interactions in SAND. A Kalman filter is an iterative algorithm that uses a system's physical laws of motion, known control inputs, and multiple sequential measurements to estimate the system's varying quantities. At each iteration, it produces an estimate of the system's state as a weighted average of the predicted state and the new measurement. The Extended Kalman filter expands this technique to non-linear systems, such as tracking moving charged particles in a magnetized detector.

First, the algorithm is validated by reconstructing ideal trajectories in magnetic fields with varying momentum. Then, energy loss and multiple scattering effects are introduced to address challenges within the SAND inner tracking volume. The final stage involves a full simulation of the SAND detector using the GEANT4 toolkit to study the algorithm's performance in reconstructing ν_μ CC events within the energy range expected at LBNF.

Chapter 1

Neutrino Physics

The Standard Model proposes the description of elementary fermions through a gauge theory based on $SU(2)_L \times U(1)_Y$ group's symmetry. The twelve known fermions (six leptons and six quarks) are grouped as doublets for the chiral left-handed field Ψ_L and singlets for right-handed fields Ψ_R

$$\Psi_L = \begin{pmatrix} e \\ \nu_e \end{pmatrix}; \begin{pmatrix} \mu \\ \nu_\mu \end{pmatrix}; \begin{pmatrix} \tau \\ \nu_\tau \end{pmatrix} \qquad \Psi_R = e_R, \mu_R, \tau_R$$

Both quarks and leptons are all endowed with mass through the Higgs mechanisms in which the gauge scalar boson combines with the fermion field to conserve the isospin invariance. However, neutrinos have no right-handed singlet states, and the mass-generating mechanism does not occur for these particles. Consequently, neutrinos are considered mass-less particles within the Standard Model framework, presented in three distinct flavours depending on the charged lepton they are emitted with. A clear distinction between particles and anti-particles occurs, as their helicity Is always left-handed and right-handed respectively: in a two-component description of neutrinos (Weyl's theory), the massless nature guarantees a permanent chirality state which in this limit coincides with the helicity for both neutrinos and anti-neutrinos.

Conceiving experiments to detect neutrinos is inherently challenging and requires to maximize as possible the interaction cross-section as with a large and highly precise detectors. However, progress in experiments over the last decade has revealed neutrino mixing, indicating a non-zero mass for these particles. This discovery has sparked a surge in Beyond Standard Model (BSM) Physics research, aiming to develop a more accurate theoretical framework to describe neutrino properties.

1.1 Neutrino in the Standard Model

Before delving into the theory of neutrino oscillations, it is crucial to understand the origin of the problems associated with neutrino masses and their incompatibility with the Standard Model (SM).

Dirac's spinor, which comprises two components, each transforms according to a reducible representation of the Lorentz transformations. It is possible to define a smaller, irreducible representation to describe particles with spin 1/2. This reduction leads to two distinct theoretical frameworks: Weyl's theory, which accounts for massless fermions, and Majorana's theory, which aligns with Weyl's in the limit of massless particles but also encompasses neutrinos with non-zero masses, thereby distinguishing between Dirac and Majorana theories as physically distinct alternatives.

The recent discovery of very small neutrino masses required a debate over which theoretical description more accurately reflects the properties of these particles. In this section, we will explore the fundamental properties of neutrinos under the assumption $m_\nu = 0$ of the SM. Specifically, we will focus on two main distinctions between neutrinos: one based on helicity, which enables the differentiation between neutrinos and anti-neutrinos, and another related to electroweak interactions, which implies the observation of only the left-handed neutrinos and the right-handed anti-neutrinos in the experiments.

The Dirac equation in the limit of massless particles becomes:

$$i\partial\!\!\!/\Psi(x) = 0 \tag{1.1}$$

wich allows an invariant operation represented by the γ^5 matrix, that is if Ψ is a solution of the equation then $\gamma^5\Psi$ is a solution too. Using Dirac-Pauli representation of the gamma matrices , γ^5 is recognizable as the *chirality* operator and since is hermitian and has the property $(\gamma^5)^2 = 1$ the possible eigenvalues are ± 1. Then the solution to Dirac's equation can be separated into two invariant equations since the eigenvectors of γ^5 have the form:

$$\Psi = \begin{pmatrix} \chi \\ h\chi \end{pmatrix} \qquad \text{where } h = \frac{\bar{\sigma}\cdot\bar{p}}{|p|} \qquad \text{is the helicity}$$

The generic spinor Ψ can be split into two irreducible and independent components as $\Psi = \Psi_L + \Psi_R$ using respectively the *left-handed* and *right-handed* Weyl's spinors defined through the projector operators P_L and P_R

$$\Psi_L = P_L\Psi(x) \qquad \Psi_R = P_R\Psi(x) \qquad \text{with } P_R = \frac{1+\gamma_5}{2} \qquad P_L = \frac{1-\gamma_5}{2}$$

so the eigenvectors of the chirality operator γ^5 become

$$\gamma^5\Psi_L = -1\Psi_L \qquad \gamma^5\Psi_R = +1\Psi_R$$

Let us examine the explicit solutions to Eq. (1.1) defining spinors with positive

energy $E > 0$ and momentum $\mathbf{p}$ as

$$u_+(p) = \frac{1}{\sqrt{2}}\begin{pmatrix}\chi^+\\ \chi^+\end{pmatrix}$$

$$u_-(p) = \frac{1}{\sqrt{2}}\begin{pmatrix}\chi^-\\ -\chi^-\end{pmatrix}$$

while spinors with negative energy solution $E < 0$ and momentum -$\mathbf{p}$ are

$$u_+(-p) = v_-(p) = \frac{1}{\sqrt{2}}\begin{pmatrix}\chi^+\\ \chi^+\end{pmatrix}$$

$$u_-(p) = v_+(p) = \frac{1}{\sqrt{2}}\begin{pmatrix}\chi^-\\ -\chi^-\end{pmatrix}$$

These are representations of massless fermions with different helicity spinors

- $u_+(p)$ and $v_-(p)$ are eigenvectors of γ^5 with eigenvalues $+1$
- $u_-(p)$ and $v_+(p)$ are eigenvectors of γ^5 with eigenvalues -1

Taking as a reference the *hole* theory to clarify the exchange of the signs between $u(p)$ and $v(p)$, the spinors $u_\pm(-p)$ are associated to the destruction of a neutrino in a negative energy state with momentum -$\mathbf{p}$ and spin $s = \pm 1/2$ which correspond to the creation of a hole i.e creation of an anti-neutrino with momentum $\mathbf{p}$ and spin $s = \mp 1/2$ described by $v(p)$. Thus the matrix element of the invariant density $\overline{\Psi}\Psi$ which compared to Dirac's equation can be rewritten in terms of the two components $\overline{\Psi}\Psi = \overline{\Psi}_L\Psi_R + \overline{\Psi}_R\Psi_L$ and it can be shown that the matrix element between the vacuum state and a state with a neutrino anti-neutrino pair is different from zero, in fact using the spinors with momentum -$\mathbf{p}$ and helicity ± 1

$$u_\pm(-p) = \frac{1}{\sqrt{2}}\begin{pmatrix}\chi^\mp\\ \pm\chi^\mp\end{pmatrix} v_\pm(-p) = \frac{1}{\sqrt{2}}\begin{pmatrix}\mp\chi^\pm\\ \chi^\pm\end{pmatrix}$$

keeping only the terms different from zero one obtain

$$\langle v(p)\bar{v}(-p)|\overline{\Psi}_R\Psi_L|0\rangle = \bar{u_+}(p)v_+(-p)e^{-ip\cdot x+ip'\cdot x}$$

$$\langle v(p)\bar{v}(-p)|\overline{\Psi}_L\Psi_R|0\rangle = \bar{u_-}(p)v_-(-p)e^{-ip\cdot x+ip'\cdot x}$$

We have determined that a neutrino and an anti-neutrino are produced with opposite helicities. Specifically, neutrino exhibits negative helicity, meaning is generated with spin opposite to the direction of its motion, while anti-neutrino displays positive helicity, with spin aligned in the direction of its motion.

This distinction provides a means to differentiate between neutrinos and anti-neutrinos. However, it is important to note that this differentiation is valid only under the assumption that $m_\nu = 0$. Since helicity is not Lorentz invariant, for massive particle is always possible to transofrm into a frame in which the the momentum direction is reversed. This raises a critical question: what occurs if the neutrino has

non-zero mass and the direction of the momentum is reversed? It becomes necessary to understand if is possible to retain a distinction between neutrinos and antineutrinos without this constriction.

The other relevant observation is that anti-fermions interact only with the opposite component of the helicity to one of the fermions.This is supported by experimental observations related to the electroweak coupling of leptons, where the following statements hold:

- Only the left-handed of the spinors $u(p)$ (fermions) and the right-handed of the spinors $v(p)$ (anti-fermions) partecipate in the charged weak current processes, violating the parity.
- Electromagnetic interaction does not allow any distinction between left and right components of the charged leptons.

These findings imply that the left components of the spinors form a doublet under isospin, whereas the right components form a singlet. The corresponding density currents (particularly for neutrinos) are detailed as follows:

$$J_\mu^+(CC) = \bar{\nu}_L \gamma_\mu e_L$$

$$J_\mu^-(CC) = \bar{e}_L \gamma_\mu \nu_L$$

$$J_\mu^3(NC) = \frac{1}{2}(\bar{\nu}_L \gamma_\mu \nu_L - \bar{e}_L \gamma_\mu e_L)$$

where $\mu = 0, 1, 2, 3$ and the left-handed chiral components of the spinors $\nu_L = \frac{1}{2}(1-\gamma_5)\nu$ and $e_L = \frac{1}{2}(1-\gamma_5)e$.
Only the left-handed neutrinos ν_L and right-handed anti-neutrinos $\bar{\nu}_R$ can couple with the respective leptons. The other two states $\bar{\nu}_L$ and ν_R are not included in the SM since they interact neither through electroweak interactions nor strong ones means they couple with any of the gauge fields of the Standard Model.

1.2 Dirac vs. Majorana theories

The problem of neutrino oscillation underscores the need to extend the Standard Model to account for the existence of three distinct mass states. This challenge represents one of the principal issues in modern physics, with multiple theories currently under development. The questions raised in the previous section suggest two primary theoretical responses regarding the representation of the neutrino field: through Dirac or Majorana formulations.

Dirac Neutrinos with definite masses are Dirac particles if the total lepton number is conserved. In this case, neutrino and anti-neutrino will have the identical mass (CPT conservation) but carry opposite lepton number $L(\nu_i) = -L(\bar{\nu}_i) = 1$. In the rest frame, the particle will be described as a quadruplet: two spin states for the neutrino and two spin states for the anti-neutrino.
At ultrarelativistic velocity and in the direction of the spin, one of these states will be allowed to react with the matter through weak interactions, whereas the other state will not, thus excluding the existence of ν_R and $\bar{\nu_L}$ states.

Majorana Neutrinos with definite masses are Majorana particles if there's no conserved lepton number,meaning there is no quantum number to distinguish between particles and antiparticles. In 1937 Majorana proposed a framework in which $\nu_i = \bar{\nu}_i$ simplifying the field representation to just two spin states. This is not in agreement with electroweak interaction theories and the properties that we have seen, particularly because, in the case of massive particles, helicity is no longer an invariant property under any of the gauge fields of the Standard Model.

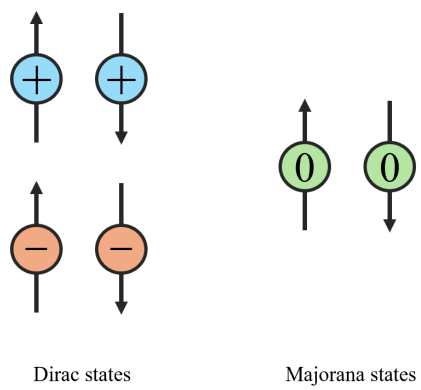

Figure 1.1: Massive fields at rest frame. The arrows show the possible directions of the spin. (Left) Dirac field has four states. The signs indicate a conventional charge to distinguish particles from anti-particles. (Right) The only two possible states for Majorana's massive field where the "zero" indicates the absence of any U(1) charge meaning that there is no distinction between particles and antiparticles.

It is clear nowadays that at least an extension of the SM is necessary. We will not see deeply the possible theories beyond the Standard Model in this thesis, but at the moment the two main possibilities to describe neutrino states considering the existence of neutrino masses are offered by Dirac theory and Majorana theory.

If the Lagrangian is invariant under global phase transformation a conserved quantity must exist. In field theory, the mass is determined by the mass terms in the Lagrangian which have to be Lorentz invariant. As we have seen previously neutrino only exists in one state of helicity ν_L and $\overline{\nu_R}$. In the context of the Standard Model,

this implies that no mass terms are allowed. The neutrino masses can be induced by applying the mass term of the Dirac equation to neutrinos.

In the case of Dirac Lagrangian even if is manifestly invariant and could be possible to associate a conserved quantum number, the mass term is identical to zero since contrary to the Standard Model, this requires having both left and right-handed neutrinos:

$$\mathcal{L}_D = m_D \bar{\Psi}\Psi = m_D(\bar{\nu}_L \nu_R + \bar{\nu}_R \nu_L)$$

While the mass term of Majorana, which involves only the helicity state that is observable,

$$\mathcal{L}_M = \frac{1}{2} m_M \bar{\Psi}\Psi^C + h.c. = m_M((\bar{\nu}_L)^C \nu_R + \bar{\nu}_L(\nu_L)^C)$$

is not invariant since contains terms which are not Lorentz invariants such as $\overline{\Psi}$ Ψ^C $\overline{\Psi}^C$ and is not acceptable in the SM also due to the violation of the Lepton number's conservation and the absence of any coupling terms through Higgs fields and fermions. There's no quantum number which allows the distinction between neutrino and anti-neutrino. This can be written also in terms of its chiral components considering m_L and m_R the real Majorana masses:

$$\mathcal{L}_L = \frac{1}{2} m_L \bar{\Psi}_L \Psi_R^C + h.c. \tag{1.2}$$

$$\mathcal{L}_R = \frac{1}{2} m_R \bar{\Psi}_L^C \Psi_R + h.c. \tag{1.3}$$

where Ψ_L and Ψ_R^C represent the known neutrino interaction (active neutrinos) while Ψ_L^C and Ψ_R represent the never-observed state of neutrino that are supposed to not interact (sterile neutrinos).

A third option could be considering the most general mass term as a combination of $\mathcal{L}_D$ and $\mathcal{L}_M$ of the form:

$$\mathcal{L}_{DM} = -\frac{1}{2} \sum_{i=1}^{6} m_i \bar{\nu}_i \nu_i$$

where the mass eigenstate can be obtained after a proper diagonalization of the mass matrix:

$$m_{1,2} = \frac{1}{2}[(m_L + m_R) \pm \sqrt{(m_L - m_R)^2 + 4m_D^2}]$$

it can be seen how the case with $m_L = m_R = 0$ corresponds to a pure Dirac case, while for $m_D = 0$ it returns the pure Majorana model.

1.3 Oscillation's probability

Flavour oscillations of neutrino is a quantum-mechanics phenomenon for which a neutrino created with an initial flavour ν_α is going to assume a different value ν_β

with $\alpha \neq \beta$ during its propagation.

According to the standard theory of neutrino oscillation, a neutrino (anti-neutrino) υ_α created in a charged current weak interaction is emitted or absorbed concurrently with one of the leptons $e^\pm \mu^\pm \tau^\pm$ from which it derives its leptonic family

If neutrinos were massless, the different flavour states of neutrinos would be degenerate, allowing for a basis in which both the Hamiltonian and the lepton flavours could be simultaneously diagonalized. This will be equivalent to aligning the neutrino states with the basis of the associated charged lepton states.

However, if neutrinos are massive, it is no longer true that the mass matrices of leptons and neutrinos are concurrently diagonalizable, leading to the potential for neutrino mixing and the violation of lepton number conservation.

From the 1960s, systematic observations of neutrinos from various sources, facilitated by the development of large-scale detectors, revealed that electrons and muons resulting from neutrino interactions with detectors correspond to two different types of neutrinos ν_e and ν_μ.respectively.

Oscillation theory supported by experimental evidence foresees that each flavour state does not correspond bijectively to a single mass eigenstate but is instead a superposition of the three different mass eigenstates. To provide a formal description of the oscillation phenomenology let's define two orthonormal bases in Hilbert's space

$$\begin{array}{lll} |\boldsymbol{\upsilon_\alpha}\rangle & \alpha = e, \mu, \tau & \text{flavour} \\ |\boldsymbol{\upsilon_i}\rangle & i = 1, 2, 3 & \text{mass} \end{array}$$

Then a neutrino created in a weak interaction from a charged lepton l_α^- or together with a charged anti-lepton l_α^+ is described in a flavour basis that is expressed as a linear combination of the flavour one and vice versa as

$$|\boldsymbol{\upsilon_\alpha}\rangle = \sum_i U^*_{\alpha,i} |\boldsymbol{\upsilon_i}\rangle \qquad |\boldsymbol{\upsilon_i}\rangle = \sum_\alpha U_{\alpha,i} |\boldsymbol{\upsilon_\alpha}\rangle \tag{1.4}$$

where $U_{\alpha,i}$ is the Pontecorvo-Maki-Nakagawa-Sakata (**PMNS**) unitary mixing matrix that describes the flavour changing of leptons.

If this matrix were equal to the identity $U = \mathbf{1}$ for each flavour would correspond only one mass eigenstate (as in the SM). Furthermore, note that the unitarity of the matrix and the orthonormality of the mass eigenstates $\langle \upsilon_k | \upsilon_i \rangle = \delta_{ki}$ implies the orthonormality also for flavour eigenstates $\langle \upsilon_\beta | \upsilon_\alpha \rangle = \delta_{\alpha\beta}$.

If neutrinos with definite mass are Dirac particles the PMNS matrix 3×3 is parametrized in the following form:

$$U_{PMNS} = \begin{pmatrix} c_{12}c_{13} & s_{12}c_{13} & s_{13}e^{-i\delta} \\ -s_{12}c_{23} - c_{12}s_{23}s_{13}e^{i\delta} & c_{12}c_{23} - s_{12}s_{23}s_{13}e^{i\delta} & s_{23}c_{13} \\ s_{12}s_{23} - c_{12}c_{23}s_{13}e^{i\delta} & -c_{12}s_{23} - s_{12}c_{23}s_{13}e^{i\delta} & c_{23}c_{13} \end{pmatrix} \tag{1.5}$$

with $s_{ij} = \sin\theta_{ij}$ $c_{ij} = \cos\theta_{ij}$ $ij = 12, 13, 23$. where the independent parameters are:

- *Three mixing angles* $\theta_{12}, \theta_{13}, \theta_{23}$ whose values are in the interval $[0, \pi]$. These parameters have been measured giving the peculiar result $\theta_{13} << \theta_{12,23}$. Attending the SM instead one would expect angles with similar order of magnitude that decrease as for CKM quarks mixing matrix.

- *One phase* δ_{CP} defined in the interval $[0, 2\pi]$ account for the CP symmetry conservation. If this symmetry is conserved the only phase space physically possible would be $\delta_{CP} = 0$ resulting in a real matrix. Over the years this scenario has been increasingly discredited by evidence suggesting a non-zero phase. Furthermore, if neutrinos are identified as Majorana particles, two additional complex phases would emerge

The determination of matrix elements $|U_{\alpha,i}|^2$ allowed to establish the specific flavours content in each mass eigenstate hence how ν_i has or not the probability to interact with a specific lepton l_α. The relative fractions are inferred from experimental measurements and can be approximately expressed as follow[1]

$$
\begin{aligned}
|\boldsymbol{\upsilon_1}\rangle &= \sqrt{\frac{2}{3}}|\boldsymbol{\upsilon_e}\rangle + \sqrt{\frac{1}{6}}|\boldsymbol{\upsilon_\mu}\rangle + \sqrt{\frac{1}{6}}|\boldsymbol{\upsilon_\tau}\rangle \\
|\boldsymbol{\upsilon_2}\rangle &= \sqrt{\frac{1}{3}}|\boldsymbol{\upsilon_e}\rangle + \sqrt{\frac{1}{3}}|\boldsymbol{\upsilon_\mu}\rangle + \sqrt{\frac{1}{3}}|\boldsymbol{\upsilon_\tau}\rangle \\
|\boldsymbol{\upsilon_3}\rangle &= \sqrt{\frac{2}{20}}|\boldsymbol{\upsilon_e}\rangle + \sqrt{\frac{9}{20}}|\boldsymbol{\upsilon_\mu}\rangle + \sqrt{\frac{9}{20}}|\boldsymbol{\upsilon_\tau}\rangle
\end{aligned}
$$

To demonstrate that direct observation of neutrino flavour oscillations necessitates the existence of distinct mass states, the propagation can be analyzed using the principles of wave-particle duality.This allows each neutrino state to be interpreted as a wave propagating into vacuum with varying frequencies. Therefore, the neutrino flavour oscillates because of the changing phase.

The probability of this oscillation depends directly on the squared-mass difference between the final and initial state. To give a proper calculation whose formalism is indeed quite clear and simple ,is necessary to define some preliminary assumption:

i) Neutrinos are treated as ultra-relativistic particles, which is possible since the upper limit on neutrino's mass is $m_i < 1.1$ eV being much lower than the involved energies[2].

ii) Each initial neutrino propagates as a plane wave whose wavelength is $\lambda = \frac{\hbar}{p_i}$, where p_i is the momentum of the neutrino with mass m_i, that can be obtained

from the relativistic relation $p_i^2 = \frac{(E^2 - m_i^2)}{c^2}$.

iii) As a consequence of the previous conditions is it possible to approximate $|\boldsymbol{p_i}| \simeq E - \frac{m_i^2}{2E_i^2} \simeq E_i$

Given a neutrino in an initial state $|\boldsymbol{\upsilon_\alpha}\rangle$ with known flavour, the probability that after a certain time t will be in a different flavour eigenstate $|\boldsymbol{\upsilon_\beta}\rangle$ can be computed by solving the Schr$\ddot{o}$edinger's equation. Massive neutrino states are eigenstate of the Hamiltonian so

$$i\frac{d}{dt}|\boldsymbol{\upsilon_i(t)}\rangle = H|\boldsymbol{\upsilon_i(t)}\rangle$$

whose generic solution is given by

$$|\boldsymbol{\upsilon_i(t)}\rangle = e^{-iE_it}|\boldsymbol{\upsilon_i(0)}\rangle$$

to change into a basis of the flavour eigenstates we can use the relation (1.4)

$$\begin{aligned}|\boldsymbol{\upsilon_\alpha(t)}\rangle &= \sum_{i=1}^{3} U^*_{\alpha,i} e^{-iEit}|\boldsymbol{\upsilon_i}\rangle \\ &= \sum_{\beta}(\sum_{i=1}^{3} U^*_{\alpha,i} e^{-iEit} U_{\beta,i})|\boldsymbol{\upsilon_\beta}\rangle\end{aligned}$$

To express the transition amplitude from iniital state $|\boldsymbol{\upsilon_\alpha}\rangle$ to a final state $|\boldsymbol{\upsilon_\beta}\rangle$

$$\mathcal{A}(\boldsymbol{\upsilon_\alpha} \longrightarrow \boldsymbol{\upsilon_\beta}) = \langle \boldsymbol{\upsilon_\beta}|\boldsymbol{\upsilon_{\alpha(t)}}\rangle = \sum_{i,j} U^*_{\alpha,i} U_{\beta,i} U_{\alpha,j} U^*_{\beta,j} e^{-i(E_i - E_j)t} \tag{1.6}$$

where:

- $U^*_{\alpha,i}$ express the transition from an initial flavour state $\boldsymbol{\upsilon_\alpha}$ to an undefined mass state $\boldsymbol{\upsilon_i}$

- e^{-iEt} is the time evolution of $\boldsymbol{\upsilon_i}$

- $U_{\beta,i}$ express the transition from the i-mass state to the final flavour state $\boldsymbol{\upsilon_\beta}$

Is then possible to compute the probability that a neutrino produced with a flavour α could be detected with a different flavour β after travelling for a time t in the vacuum, as $|\mathcal{A}|^2$:

$$\mathcal{P}_{\upsilon_\alpha \to \upsilon_\beta} = \left| \sum_{i,j} U^*_{\alpha,i} U_{\beta,i} U_{\alpha,j} U^*_{\beta,j} e^{-i(E_i - E_j)t} \right|^2$$

using the former approximations for which

$$p_i^2 \simeq p \text{ and } E_i = \sqrt{p^2 + m_i^2} \Rightarrow E_i - E_j \simeq \frac{\Delta m_{ij}^2}{2E}$$

where $\Delta m_{ij}^2 = m_i^2 - m_j^2$, then

$$\mathcal{P}_{\upsilon_\alpha \to \upsilon_\beta} = \left| \sum_{i,j} U^*_{\alpha,i} U_{\beta,i} U_{\alpha,j} U^*_{\beta,j} e^{\frac{-i\Delta m_{i,j}^2 t}{2E}} \right|^2 \tag{1.7}$$

If $\alpha = \beta$ it will be called *survival* probability, otherwise for $\alpha \neq \beta$ it represents the probability of oscillations. We can finally observe how the probability that a flavour change occurs is determined by the element of the mixing matrix and is directly dependent on the mass square difference. If no different mass states exist, no oscillation phenomenon will be possible. From the point of view of the experimental purposes, Eq. 1.7 contains only a term related to a squared-mass splitting which means that from the point of view of the experimental results we are not able to find out the single absolute value for each mass eigenstate explicitly.

Time t represents the difference between the neutrino's production moment and the observation. Ss we have said for a relativistic particle this can be approximated to the path length L i.e $t \simeq L$. We can rewrite 1.7 as:

$$\mathcal{P}_{\upsilon_\alpha \to \upsilon_\beta}(L, E) = \sum_i |\boldsymbol{U_{\alpha,i}}|^2 |\boldsymbol{U_{\beta,i}}|^2 + 2\Re \sum_{i>j} \boldsymbol{W_{i,j}^{\alpha\beta}} e^{-\frac{i\Delta m_{ij}^2 L}{2E}}$$

where the following notation has been used:
$\boldsymbol{W_{i,j}^{\alpha\beta}} = \boldsymbol{U^*_{\alpha,i} U_{\beta,i} U_{\alpha,j} U^*_{\beta,j}}$
Note the following properties related to the transition probability expression:

- Probability conservation must be true

$$\sum_\beta \mathcal{P}_{\upsilon_\alpha \to \upsilon_\beta} = \sum_\alpha \mathcal{P}_{\upsilon_\alpha \to \upsilon_\beta} = 1$$

- The independent $\Delta m_{i,j}^2$ are two since there are three families of neutrino.

- $\frac{L}{E}$ is the parameter under experimental control. L is the distance between the source and the detector, and E is the neutrino energy. For a given $\Delta m_{i,j}^2$ the

probability of oscillation will change as one moves away from the detector or scans over different neutrino energies. Experimentally, if a particular value of mass splitting between two states is hypothesized, these two quantities can be adjusted to maximize sensitivity to the oscillation events.

The derivation of the transition probability has been significantly simplified by assuming that each neutrino possesses a definite energy and propagates as a plane wave. However, this assumption is not entirely realistic from a quantum mechanics perspective. It is, in fact, impossible to guarantee a state with fixed and definite energy unless one can experiment over infinitely long times. To address this issue, a computation based on wave packets should be necessary, introducing additional corrections. Neverthless, in a first approximation, this aligns with the results we have already observed.[1]

1.3.1 Two-family neutrino mixing

Given that many experiments are not sensitive to the complexities of three-neutrino mixing, data from these studies are often analyzed using an effective two-neutrino mixing model. This simplified approach involves only two neutrino families, reducing the number of parameters: the mixing angle will be only one $\theta_{1,2} = \theta$ and the two generic flavour states will be a linear combination of the mass state υ_1 and υ_2 whose coefficients are given by the elements of 2×2 reduced form of the U_{PMNS} matrix.

$$|\boldsymbol{\upsilon_\alpha}\rangle = \cos\theta|\boldsymbol{\upsilon_1}\rangle + \sin\theta|\boldsymbol{\upsilon_2}\rangle$$

$$|\boldsymbol{\upsilon_\beta}\rangle = \cos\theta|\boldsymbol{\upsilon_1}\rangle - \sin\theta|\boldsymbol{\upsilon_2}\rangle$$

where each mass state evolves as :

$$|\boldsymbol{\upsilon_i}(t)\rangle = e^{\frac{i}{\hbar}(\boldsymbol{p_i x} - Et)}|\boldsymbol{\upsilon_i}(0)\rangle$$

After a lenght $x = L$ and time $t \simeq L$ neutrino with initial flavour α will be:

$$|\boldsymbol{\upsilon_\alpha}(t)\rangle = \cos\theta e^{-iE_1 t}|\boldsymbol{\upsilon_1}\rangle + \sin\theta e^{-iE_2 t}|\boldsymbol{\upsilon_2}\rangle$$

as sen before, the probability that the state has changed the flavour and will be detected as υ_β is given by $|\langle\boldsymbol{\upsilon_\beta}|\boldsymbol{\upsilon_\alpha}(t)\rangle|^2$:

$$\mathcal{P}_{\upsilon_\alpha \to \upsilon_\beta} = \frac{1}{2}\sin^2 2\theta \left[1 - \cos\left(\frac{\Delta m^2_{1,2} L}{2E}\right)\right]$$

[1] It has been assumed the natural units system $\hbar = c = 1$

using the trigonometric formula $\cos x = 1 - 2\sin^2 x$ allows to find the final form:

$$\mathcal{P}_{\upsilon_\alpha \to \upsilon_\beta}(E, L) = \sin^2 2\theta \sin^2 \left(\frac{\Delta m_{12}^2 L}{4E} \right) \tag{1.8}$$

As already mentioned before, the amplitude of oscillation depends on the ratio L/E. Since in reactor oscillation experiments $E \sim 1$ MeV, and in accelerator experiments $E \sim 1$ GeV, the Eq. 1.8 can be rewritten in more convenient units using:

$$\frac{\Delta m_{ijL}^2}{4E} = \frac{\Delta m_{ij}^2 L}{4\hbar c E} = 1.27 \frac{\Delta m_{ij}^2 (eV^2) L(km)}{E(GeV)} = 1.27 \frac{\Delta m_{ij}^2 (eV^2) L(m)}{E(MeV)}$$

Is it often used to rewrite this equation in terms of the oscillation length defined as $L_{osc} = 4\pi \frac{E}{\Delta m^2}$ which corresponds to the distance after which the probability of transition is maximal

$$\mathcal{P}_{\upsilon_\alpha \to \upsilon_\beta}(E, L) = \sin^2 2\theta \sin^2 \left(\pi \frac{L}{L_{osc}} \right)$$

For $\alpha = \beta$ the *survival* probabiliyty is easily obtained from Eq.1.8 to search for neutrino deficit in the incident flux

$$\mathcal{P}_{\nu_\alpha \to \nu_\alpha} = 1 - \mathcal{P}_{\nu_\alpha \to \nu_\beta} = 1 - \sin^2 2\theta \sin^2 \left(\frac{\Delta m^2 L}{4E} \right)$$

1.3.2 Three-family neutrino mixing

The calculation of neutrino oscillation probability for two flavours shows the fundamental physics aspects of this phenomenon, including the correlation between the weak and mass eigenstates and the oscillatory behaviour due to the phase difference among the mass eigenstates in the time evolution of the wave function. The three-family mixing involves a similar approach, though the mathematical complexity is heightened. In this framework the three weak eigenstates are linked to the masses through a 3×3 unitary PMNS matrix:

$$\begin{pmatrix} \nu_e \\ \nu_\mu \\ \nu_\tau \end{pmatrix} = \begin{pmatrix} U_{e1} & U_{e2} & U_{e3} \\ U_{\mu 1} & U_{\mu 2} & U_{\mu 3} \\ U_{\tau 1} & U_{\tau 2} & U_{\tau 3} \end{pmatrix} \begin{pmatrix} \nu_1 \\ \nu_2 \\ \nu_3 \end{pmatrix}$$

Let's now consider the simplest example of a β^+ decay process where the neutrino is emitted along with an electron in a CC weak interaction. The neutrino is expressed as a coherent linear superposition of mass eigenstates whose wavefunction at time $t = 0$ is:

$$|\Psi(0)\rangle = |\nu_e\rangle = U_{e1}^* |\nu_1\rangle + U_{e2}^* |\nu_2\rangle + U_{e3}^* |\nu_3\rangle$$

and the time evolution of each mass eigenstate brought different phase $\phi_i = p_i \cdot x_i = (E_i T - \boldsymbol{p}_i \cdot \boldsymbol{x})$ as explained in Sec. 1.3

$$|\Psi(\boldsymbol{x},t)\rangle = |U^*_{e1}|\nu_1\rangle e^{-i\phi_1} + U^*_{e2}|\nu_2\rangle e^{-i\phi_2} + U^*_{e3}|\nu_3\rangle e^{-i\phi_3}$$

The interaction, instead, is expressed in terms of weak eigenstates ν_e, ν_μ, ν_τ. Taking into account that the neutrino enters into the interaction vertices as a spinor emitting a charged lepton from which the family is associated, the change of basis occurs through the elements of the PMNS matrix (and not its conjugate complexes).

$$\begin{aligned}|\Psi(\boldsymbol{x},t)\rangle = U^*_{e1}(U_{e1}|\nu_e\rangle + U_{\mu1}|\nu_\mu\rangle + U_{\tau1}|\nu_\tau\rangle)e^{-i\phi_1}\\ + U^*_{e2}(U_{e2}|\nu_e\rangle + U_{\mu2}|\nu_\mu\rangle + U_{\tau2}|\nu_\tau\rangle)e^{-i\phi_2}\\ + U^*_{e3}(U_{e3}|\nu_e\rangle + U_{\mu3}|\nu_\mu\rangle + U_{\tau3}|\nu_\tau\rangle)e^{-i\phi_3}\end{aligned}$$

and collecting the weak eigenstates

$$\begin{aligned}|\Psi(\boldsymbol{x},t)\rangle = (U^*_{e1}U_{e1}e^{-i\phi_1} + U^*_{e2}U_{e2}e^{-i\phi_2} + U^*_{e3}U_{e3}e^{-i\phi_3})|\nu_e\rangle\\ + (U^*_{e1}U_{\mu1}e^{-i\phi_1} + U^*_{e2}U_{\mu2}e^{-i\phi_2} + U^*_{e3}U_{\mu3}e^{-i\phi_3})|\nu_\mu\rangle\\ + (U^*_{e1}U_{\tau1}e^{-i\phi_1} + U^*_{e2}U_{\tau2}e^{-i\phi_2} + U^*_{e3}U_{\tau3}e^{-i\phi_3})|\nu_\tau\rangle\end{aligned}$$

Starting from a known neutrino flavour beam the 3-flavour oscillation probability $\mathcal{P}_{\nu_\alpha \longrightarrow \nu_\beta}$ is obtained as before as

$$|\langle\nu_\beta|\Psi(\boldsymbol{x},\boldsymbol{t})\rangle|^2 = \left|U^*_{\alpha1}U_{\beta1}e^{-i\phi_1} + U^*_{\alpha2}U_{\beta2}e^{-i\phi_2} + U^*_{\alpha3}U_{\beta3}e^{-i\phi_3}\right|^2$$

which can be rewritten using the complex number identity as

$$\begin{aligned}\mathcal{P}_{\nu_\alpha \longrightarrow \nu_\beta} = |U^*_{\alpha1}U_{\beta1}|^2 + |U^*_{\alpha2}U_{\beta2}|^2 + |U^*_{\alpha3}U_{\beta3}|^2\\ + 2\mathfrak{Re}\left\{U^*_{\alpha1}U_{\beta1}U_{\alpha2}U^*_{\beta2}e^{-i(\phi_1-\phi_2)}\right\}\\ + 2\mathfrak{Re}\left\{U^*_{\alpha1}U_{\beta1}U_{\alpha3}U^*_{\beta3}e^{-i(\phi_1-\phi_3)}\right\}\\ + 2\mathfrak{Re}\left\{U^*_{\alpha2}U_{\beta2}U_{\alpha3}U^*_{\beta3}e^{-i(\phi_2-\phi_3)}\right\}\end{aligned}$$

the unitary relation in the U_{PMNS} matrix allows the following simplification

$$\sum_i^3 |U^*_{\alpha1}U_{\beta1}|^2 + 2\mathfrak{Re}\left\{[U^*_{\alpha1}U_{\beta1}U_{\alpha2}U^*_{\beta2} + U^*_{\alpha1}U_{\beta1}U_{\alpha3}U^*_{\beta2} + U^*_{\alpha2}U_{\beta2}U_{\alpha3}U^*_{\beta3}\right\} = 0$$

to finally write

$$\begin{aligned}\mathcal{P}_{\nu_\alpha \longrightarrow \nu_\beta} = 2\mathfrak{Re}\left\{U^*_{\alpha1}U_{\beta1}U_{\alpha2}U^*_{\beta2}[e^{i(\phi_2-\phi_1)} - 1]\right\}\\ 2\mathfrak{Re}\left\{U^*_{\alpha1}U_{\beta1}U_{\alpha3}U^*_{\beta3}[e^{i(\phi_3-\phi_1)} - 1]\right\}\\ 2\mathfrak{Re}\left\{U^*_{\alpha2}U_{\beta2}U_{\alpha3}U^*_{\beta3}[e^{-i(\phi_3-\phi_2)} - 1]\right\}\end{aligned} \tag{1.9}$$

where we can recognize the more familiar form with the squared mass term $\Delta_{ij} = \frac{(\phi_j - \phi_i)}{2} = \frac{(m_j^1 - m_i^2)L}{4E_\nu}$ by using the following relation:

$$\mathfrak{Re}\left\{e^{i(\phi_j-\phi_i)} - 1\right\} = -2\sin^2\frac{\phi_j - \phi_i}{2} = -2\sin^2\Delta_{ij}$$

Then from the previous expression of the oscillation probability considering three neutrino families mixing, is easy to obtain the survival probability as follows

$$\begin{aligned}\mathcal{P}_{\nu_\alpha \longrightarrow \nu_\alpha} = 1 &- 4|U_{\alpha 1}|^2|U_{\alpha 2}|^2\sin^2\Delta_{21} \\ &- 4|U_{\alpha 1}|^2|U_{\alpha 3}|^2\sin^2\Delta_{31} - 4|U_{\alpha 2}|^2|U_{\alpha 3}|^2\sin^2\Delta_{23}\end{aligned} \tag{1.10}$$

where of the three differences of squared masses, only two are independent.

1.3.3 CP violation

Theories involving neutrino masses, typically assume parametrization of the PMNS matrix that encompasses various CP-violating complex phases, which could potentially affect neutrino oscillations. In this section, we introduce the theoretical aspects of CP violation in neutrino oscillations and the potential for experimental investigation in future searches. It has long been recognized that the Dirac CP-violating phase, inherent in the simplest three-neutrino model, could theoretically manifest in experiments that compare neutrino and antineutrino oscillations.

The relations between a non-zero δ_{CP} and a violation of the symmetry can be shown considering the neutrino oscillation probability computed in (1.9), from which the oscillation probability for antineutrino can be obtained considering that the elements of the PMNS matrix are either $\boldsymbol{U}$ or $\boldsymbol{U}^*$ depending on whether the neutrino appears as spinor or adjoint-spinor in the interaction vertex.

$$\mathcal{P}_{\overline{\nu}_\alpha \longrightarrow \overline{\nu}_\beta} = 2\mathfrak{Re}\left\{U_{\alpha 1}U^*_{\beta 1}U^*_{\alpha 2}U_{\beta 2}[e^{i(\phi_2-\phi_1)} - 1]\right\} + ... \tag{1.11}$$

Where the elements of the PMNS matrix are the complex conjugate of those for $\mathcal{P}_{\nu_\alpha \longrightarrow \nu_\beta}$, then unless $U_{\alpha i}$ and $U_{\beta j}$ are real, charge-parity symmetry does not hold in oscillations.

Effects of applying charge conjugation $\hat{C}$ and parity transformation $\hat{P}$ can be easily displayed considering the weak decay of a pion $\pi^- \longrightarrow \mu^-\overline{\nu_\mu}$ where the antineutrino is effectively always emitted in an RH helicity state. The parity operator reverses the particle momenta leaving the spins unchanged and resulting in a final state of an LH anti-neutrino. Based on the discussion provided in Sec.1.2 the matrix element of such a process is zero. Charge conjugation operator $\hat{C}$ instead acts by exchanging particles and anti-particles, resulting in this case with an RH neutrino which again violates the symmetry. But the combined operation $\hat{C}$ and $\hat{P}$ overall results in a valid state leaving, in principle the symmetry unviolated [3]. Finding a CP violation

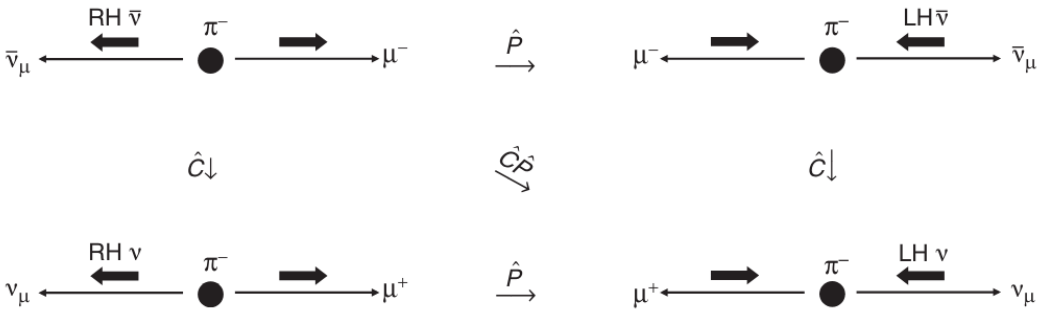

Figure 1.2: Charged pion decay and the outcomes derived from the application of $\hat{C}$, $\hat{P}$, and the combined $\hat{C}\hat{P}$.

becomes essential to explain the surplus of matter compared to antimatter observed in the Universe. Given that the interactions of QED and QCD individually preserve both $\hat{C}$ and $\hat{P}$, thereby conserving CP, weak interactions are the onliest method to observe the potential effects of a violation.

We have seen that the imaginary components of the PMNS matrix provide a possible source of a CP violation. The simplest method to evaluate the magnitude of the violation would be through the measure of an asymmetry between neutrinos and anti-neutrinos oscillations:

$$\Delta\mathcal{P}_{\alpha\beta} = \mathcal{P}_{\nu_\alpha \longrightarrow \nu_\beta} - \mathcal{P}_{\bar{\nu_\alpha} \longrightarrow \bar{\nu_\beta}}$$

Starting from the equation (1.11) consider a general case of muon appearance experiment for which $\alpha = e$ and $\beta = \mu$:

$$\begin{aligned}
\mathcal{P}_{\nu_e \longrightarrow \nu_\mu} &= 2\sum_{i<j} \mathfrak{Re}\left\{U^*_{e1}U_{\mu1}U_{e2}U^*_{\mu2}[e^{i(\phi_j-\phi_i)} - 1]\right\} \\
&= 2\sum_{i<j} \mathfrak{Re}\left\{U^*_{e1}U_{\mu1}U_{e2}U^*_{\mu2}[\cos(\phi_j-\phi_i) - 1 + i\sin(\phi_j-\phi_i)]\right\} \\
&= 2\sum_{i<j} \mathfrak{Re}\left\{\boldsymbol{U}[\cos(\phi_j-\phi_i) - 1\right\} - 2\sum_{i<j} \mathfrak{Im}\left\{\boldsymbol{U} + i\sin(\phi_j-\phi_i)]\right\} \\
&= -4\sum_{i<j} \mathfrak{Re}\left\{\boldsymbol{U}\sin^2\left(\frac{\phi_j-\phi_i}{2}\right)\right\} + 2\sum_{i<j} \mathfrak{Im}\left\{\boldsymbol{U}\sin(\phi_j-\phi_i)\right\} \\
&= -4\sum_{i<j} \mathfrak{Re}\left\{\boldsymbol{U}\right\}\sin^2\Delta_{ij} + 2\sum_{i<j} \mathfrak{Im}\left\{\boldsymbol{U}\right\}\sin 2\Delta_{ij}
\end{aligned}$$

where to improve readibility $\boldsymbol{U} = U^*_{e1}U_{\mu1}U_{e2}U^*_{\mu2}$ and $\Delta_{ij} = \frac{\phi_i-\phi_j}{2}$ have been used. Let us now introduce the so-called Jarlskog invariant $J = \mathfrak{Im}\left\{U^*_{e1}U_{\mu1}U_{e2}U^*_{\mu2}\right\}$ in order to write the previous equation as:

$$\begin{aligned}\mathcal{P}_{\nu_e \longrightarrow \nu_\mu} = & -4\mathfrak{Re}\{\boldsymbol{U}\}\sin^2\Delta_{ij} + 2J\left(2\sin 2\Delta_{12} - \sin 2\Delta_{13} + \sin 2\Delta_{23}\right) \\ = & -4\mathfrak{Re}\{\boldsymbol{U}\}\sin^2\Delta_{ij} + 2J\left(2\sin 2\Delta_{12} + \sin 2\Delta_{23} + \sin 2(\Delta_{13} - \Delta_{23})\right)\end{aligned}$$

using the identity $\sin A + \sin B + \sin(A+B) = 4\sin\left(\frac{A}{2}\right)\sin\left(\frac{B}{2}\right)\sin\left(\frac{A+B}{2}\right)$ it becomes

$$\mathcal{P}_{\nu_e \longrightarrow \nu_\mu} = -4\mathfrak{Re}\{\boldsymbol{U}\}\sin^2\Delta_{ij} + 8J\sin\Delta_{12}\sin\Delta_{13}\sin\Delta_{23}$$

Finally, generalizing for all the three neutrino flavours we can find the expression for the quantity $\Delta\mathcal{P}_{\alpha\beta}$ subtracting the expression for $\mathcal{P}_{\bar{\alpha}\longrightarrow\bar{\beta}}$ obtained as in (1.11)

$$\Delta\mathcal{P}_{\alpha\beta} = \pm 16J\sin\left(\frac{\Delta m^2_{21}L}{4E}\right)\sin^2\left(\frac{\Delta m^2_{31}L}{4E}\right)\sin^2\left(\frac{\Delta m^2_{32}L}{4E}\right) \tag{1.12}$$

where the sign depends on whether there is an even (+) or odd (-) permutation of e, μ, τ. The equation above can be reformulated using PMNS matrix elements to reveal the essential requirement for observing CP violation. Te following formulation indicates that all three mixing angles θ_{ij} must be non-zero, the phase δ_{CP} must differ from 0 and π, and the squared mass differences of the three elements must be non-vanishing.

$$\Delta\mathcal{P}_{\alpha\beta} = 2\cos\theta_{13}\sin 2\theta_{12}\sin 2\theta_{13}\sin 2\theta_{23}\sin\delta_{CP} \tag{1.13}$$

The largest contribution comes from θ_{13} constrained to < 0.094 at the 90% C.L. [4] and Δm^2_{12}, being the most important suppression factor due to the experimentally observed values. The contribution of Δm^2_{23} should also be considered, as it influences the weight of the term $\sin^2\Delta_{12}$ in the oscillation probabilities. Considering these constraints, long baseline experiments governed by Δm^2_{12} emerge as the most promising avenue for directly probing the Dirac CP phase within the neutrino matrix. In these experiments, the favoured channels where appreciable CP-violating effects are observed are $\nu_e \to \nu_\mu/\overline{\nu}_e \to \overline{\nu}_\mu$ and $\nu_\mu \to \nu_\tau/\overline{\nu}_\mu \to \overline{\nu}_\tau$.

Our understanding of the PMNS matrix elements enables accurate estimation of the difference δ_{CP}, typically within a few percent. Long-baseline experiments such as T2K [5] and NOνA[6] aim to significantly constrain δ_{CP}. T2K, for instance, was the first experiment to constrain the CP violation phase within a three sigma confidence level interval of $[-3.41, -0.03]$ for the normal mass ordering and $[-2.54, -0.32]$ for the inverse ordering [7]. Conversely, NOνA excludes the region around $\delta_{CP} = \frac{\pi}{2}$ for the inverted mass ordering, consistent with T2K, but excludes the region around $\delta_{CP} = -\frac{\pi}{2}$ for the normal ordering, in tension with T2K data. This discrepancy is

due to T2K's more pronounced separation between ν_e and $\overline{\nu}_e$ oscillations compared to NOνA

DUNE and HyperKamiokande prioritise the δ_{CP} measurement. However, matter effects reduce CP observation sensitivity, especially at higher energies and longer baselines. HyperKamiokande mitigates this by adopting a shorter baseline, thereby enhancing sensitivity to δ_{CP}. Nevertheless, DUNE experiments has the potential to estabilish CP violation in the leptonic sector with a 5σ (3σ) significance in 10 (13) years for 50%(75%) of the potential δ_{CP} values. [8]

1.4 MSW Effect

The presence of matter can modify neutrino propagation through coherent forward scattering processes with particles in the medium. This alteration known as the Mikheyev-Smirnov-Wolfstein effect (MSW) or simpler "matter effect", depends on the leptonic family to which the interacting neutrino initially belongs and results in a change in the oscillation probability.

Initially identified by L. Wolfenstein in 1979 [9], the MSW effect highlights differences in the PMNS parameters between neutrinos travelling in the vacuum and those interacting with matter. These differences arise from the fact that only electron neutrinos can engage in both weak charged-current (CC) and neutral-current (NC) elastic interactions with electrons in matter, while μ_ν and μ_τ exclusively undergo NC interactions. Following Wolfenstein's observation, Soviet physicists A. Smirnov and S. Mikheyev predicted that the mixing effect in neutrinos would intensify as matter density decreases. Experimental evidence confirming this correction to the probability of oscillation was first found at Fermilab Laboratory in 1986 [10]

Propagation of neutrinos in matter can be treated again with the time evolution of the flavour eigenstate whose Hamiltonian is now H_{eff} and differs from the vacuum one from an additive perturbative term coming from the elastic scattering between neutrinos and the matter particles:

$$H_{eff} = H_0 + V_{MSW}$$

If the perturbation induced by the presence of a medium had been the same for all three neutrino flavours the total effect would be null and would have any visible effect on the oscillation. The extra interaction potential energy term V_{MSW} account for the two weak interactions:

CC Exchange of a $W^{\pm}$ boson with the corresponding charged lepton, that in the ordinary matter, it can be only electrons, affects only electronic neutrino υ_e. The interaction potential V_{MSW} is proportional to the number density of electrons N_e in the medium and to the Fermi coupling constant G_F giving for neutrinos: $V_{CC} = +\sqrt{2}G_F N_e$

NC All three neutrino flavours can exchange neutral Z bosons. If the matter is electrically neutral, meaning the density of electrons is the same as that of protons, the contribution from electrons cancels out that of the protons. As a result, the additional term in the potential energy arises only from the neutron density N_n of the media, giving $V_{NC} = -\frac{\sqrt{2}}{2} G_F N_n$

where for antineutrinos in both cases opposite sings are required.

We can then write the effective Hamiltonian introducing the two contributions to the interaction:

$$H_eff = H_0 + V_{MSW} = H_0 + V_{CC} \begin{bmatrix} 1 & 0 \\ 0 & 0 \end{bmatrix} + V_{NC} \begin{bmatrix} 1 & 0 \\ 0 & 1 \end{bmatrix}$$

The third term related to the exchange of a Z boson as said, affects all the three flavours equally then its contribution is a multiple of the identity matrix. Therefore, it can be omitted without any change in the energy eigenvalues.

$$H_eff = H_0 + \frac{V_{CC}}{2} \begin{bmatrix} 1 & 0 \\ 0 & -1 \end{bmatrix} + \frac{V_{CC}}{2} \begin{bmatrix} 1 & 0 \\ 0 & 1 \end{bmatrix}$$

Again, subtracting any multiple of the identity matrix does not lead to a loss of generality and does not modify the physical system. So the equaiton above reduce to:

$$H_eff = H_0 + \frac{V_{CC}}{2} \begin{bmatrix} 1 & 0 \\ 0 & -1 \end{bmatrix}$$

1.4.1 Two-family neutrino mixing in matter

To compute the probability of oscillation for neutrinos propagating in matter, let us consider a simplified system of only two generations.
As for the vacuum case, the propagation in the matter is given by the resolution of Schr$\ddot{o}$edinger's laboratory-frame equation where we introduce the definition of V_{CC} and of H_0 as in in the previous section.

$$i\frac{d}{dt}\begin{pmatrix} \upsilon_\alpha \\ \upsilon_\beta \end{pmatrix} = \frac{\Delta m^2}{4E} \begin{pmatrix} -\cos 2\theta & \sin 2\theta \\ \sin 2\theta & \cos 2\theta \end{pmatrix} + V_{CC} \begin{pmatrix} 1 & 0 \\ 0 & -1 \end{pmatrix} \begin{pmatrix} \upsilon_\alpha \\ \upsilon_\beta \end{pmatrix}$$

Where Δm^2 and θ are still referred to as the vacuum parameters.
To solve the problem we should try to characterise the effective Hamiltonian of this system as a function of new matter parameters Δm^2_M and θ_M.The matter Hamiltonian

is [1]:

$$H_{eff} = \frac{\Delta m^2}{4E}\begin{pmatrix} -\cos 2\theta + \frac{V_{cc}/2}{(\Delta m^2/4E)} & \sin 2\theta \\ \sin 2\theta & \cos 2\theta - \frac{V_{cc}/2}{(\Delta m^2/4E)} \end{pmatrix}$$
$$= \frac{\Delta m^2}{4E}\begin{pmatrix} -\cos 2\theta + A & \sin 2\theta \\ \sin 2\theta & \cos 2\theta - A \end{pmatrix}$$

where we have defined $A = \frac{4E}{\Delta m^2}\frac{V_{CC}}{2} = \pm\frac{2\sqrt{2}G_F N_e E}{\Delta m^2}$ to simplify the notation
To find a more suitable form similar to the one of the Eq. 1.8 let us solve the following system:

$$\begin{cases} \frac{\Delta m_M^2}{4E}\sin 2\theta_M & = \frac{\Delta m^2}{4E}\sin 2\theta \\ \\ \frac{\Delta m_M^2}{4E}\cos 2\theta_M & = \frac{\Delta m^2}{4E}(\cos 2\theta - A) \end{cases}$$

From which one can explicate the solutions for θ_M and Δm_M^2:

$$\begin{cases} \Delta m_M^2 = \Delta m^2\sqrt{(\cos 2\theta - A)^2 + (\sin 2\theta)^2} \\ \\ \sin^2 2\theta_M = \frac{\sin^2 2\theta}{\sin^2 2\theta + (\cos 2\theta - A)^2} \end{cases} \tag{1.14}$$

And write the Hamiltonian in the matter in the simplest form:

$$H_{eff} = \frac{\Delta m_M^2}{4E}\begin{pmatrix} -\cos 2\theta_M & \sin 2\theta_M \\ \sin 2\theta_M & \cos 2\theta_M \end{pmatrix}$$

It has obtained an expression for the mixing angle that depends on A i.e. on the electron density of the media, and from the neutrino's energy. The quantity Δm_M^2 is sensible to sign of A since the propagation effect in a medium resulted in be different between neutrinos and antineutrinos.
Solving the Schr$\ddot{o}$edinger's equation in matter yield a similar result of 1.8 except for the fact of using mixing parameters computed for neutrinos interacting with the medium.

$$\mathcal{P}_{\alpha\to\beta}(L,E) = |\Psi_{\alpha,\beta}|^2 = \sin^2 2\theta_M \sin^2\left(\frac{\Delta m_M^2 L}{4E}\right) \tag{1.15}$$

Resonance

Second equation obtained in the system 1.14 can be rewritten as:

$$\tan 2\theta_M = \frac{\sin 2\theta}{\cos 2\theta - A} = \frac{\tan 2\theta}{1 - \frac{A}{\cos 2\theta}}$$

From this, it can be observed that there is a *resonant condition* corresponding to $A = \cos 2\theta$ for which the presence of matter causes a mixing angle's amplification. Under this condition the electron number density is

$$N_e^{Resonance} = \frac{\Delta m^2 \cos 2\theta}{2\sqrt{2} G_F E} = N_0 \cos 2\theta \tag{1.16}$$

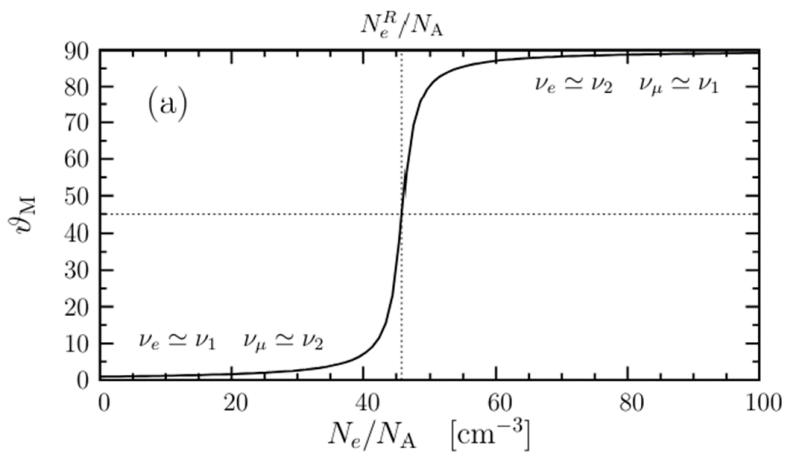

Figure 1.3: Effective mixing angle θ_M in matter as functions of the electron number density N_e divided by the Avogadro's number N_A.

And the value of $\tan 2\theta_M$ tends to $\pm\infty$ and then effective mixing angle assumes the maximum value $\theta_M = \frac{\pi}{4}$ (while the squared mass difference is at the minimum $\Delta m_M^2 = \Delta m^2 \sin 2\theta$), leading to the possibility of a total transition between two flavours if the resonant region is wide enough. The behaviour of θ_M as a function of the electron number density Ne is illustrated in Fig. 1.3 assuming $E = 1$ MeV, $\Delta m^2 = 7 \times 10^{-5} eV^2$ and $\sin 2\theta = 10^{-3}$. It can be recognized the following regions

$$N_e >> N_e^R \Rightarrow \theta_M \simeq \frac{\pi}{2} \tag{1.17}$$

$$N_e << N_e^R \Rightarrow \theta_M \simeq 0$$

$$N_e = N_e^R \Rightarrow \theta_M = \frac{\pi}{4}$$

Is interesting to display the resonant behaviour as a function of the ratio between the medium refraction length $L_e = \frac{2\pi}{\sqrt{2} G_F N_e}$ and the oscillation length in the vacuum $L_{oscill} = \frac{4\pi E}{\Delta m^2}$

$$r = \frac{L_{oscill}}{L_e} \equiv A$$

Moreover, let us define $R = \sin^2 2\theta_M$ and explicitate it as a function of r to highlight the energy and the material density dependence. Using 1.14 we have

$$R = \frac{\sin^2 2\theta}{1 + r^2 - 2r\cos 2\theta}$$

The plot of this function is shown in Fig. 1.4, where a resonance peak occurs at the point $r = \cos 2\theta$, with $R = 1$, as previously mentioned. Furthermore, the impact of material density on the resonance amplitude is evident. The width at mid-height of R is determined by $2\Delta(N_e)_R = 2(N_e)_R \tan 2\theta = 2N_0 \sin 2\theta$
Two significant limit cases can be observed:

$\theta \to 0$ $\mathrm{L}_e \simeq L_{oscill}$ the frequency that characterized a system of mixed neutrinos $\frac{c}{L_{osc}}$ corresponds to the proper frequency of the propagation medium $\frac{c}{L_e}$ and the resonance effect becomes more and more irrelevant $R \to 0$.

$\theta \to \frac{\pi}{4}$ when the mixing parameter in the vacuum tends to its maximum value the resonance shifts to the area where the material density tends to zero $N_e = 0$ (as for the vacuum) the curve becomes wider and $\Delta(N_e)_R$ grows until it converges to the value N_0 for which $R \to \frac{1}{1+r^2}$ (blue line in the plot).

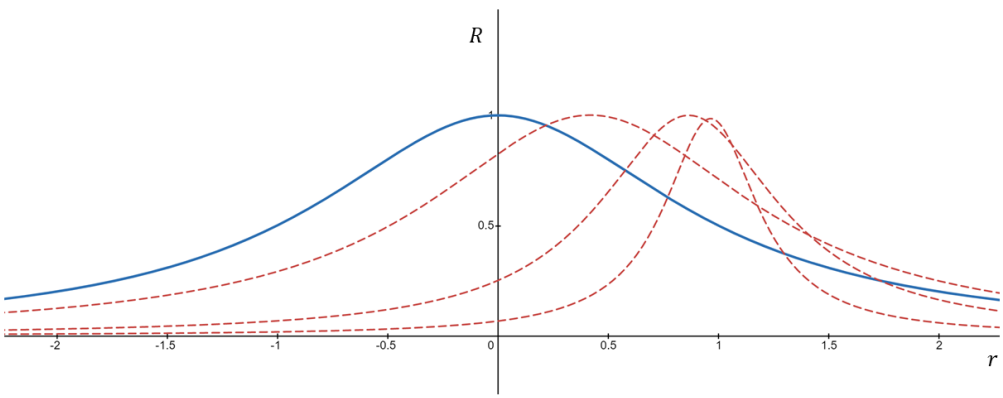

Figure 1.4: Resonance effect in matter. The picture shows the function $R(r)$ for different decreasing values of θ in red. Limit case $\theta = \frac{\pi}{4}$ is represented in blue

The MSW effect plays a crucial role in solar neutrino propagation, allowing solar neutrino experiments to measure the sign of the neutrino mass-squared difference, Δm^2_{21}. At the Sun's core, the high electron density can cause nearly complete electron

neutrino ν_e to muon neutrino ν_{mu} conversion if the conditions meet the resonance criteria. This happens when the electron density matches the critical resonance density N_e^R value, aligning the neutrinos almost entirely as ν_2 mass eigenstate. If the neutrino adiabatically crosses this resonance, it exits the Sun primarily as $\nu_2 = \sin\theta\nu_e + \cos\theta\nu_\mu$ which is, for small mixing angle, almost equal to ν_μ.

The dramatic transformation under the MSW effect, combined with a large mixing angle $\theta_{12} \simeq 34°$ and a small neutrino mass-squared difference $\Delta m^2_{21} \simeq 7.5 \times 10^{-5}\text{eV}^2$, provides a resolution to the historical "solar neutrino problem." This issue was first highlighted by the pioneering solar neutrino experiment led by Raymond Davis Jr. in the 1970s, which detected nly an half of the electron neutrino flux predicted by the standard solar models. Only in 2001 data from the Super-Kamiokande [11] and the Sudbury Neutrino Observatory [12] conclusively demonstrated that this deficit was a result of neutrino oscillations in matter

1.4.2 Matter-Antimatter asymmetry

As part of its definition, the parameter A exhibits opposite signs depending on whether neutrinos or antineutrinos are employed. Consequently, as suggested by expressions in 1.14 the values of the effective mass difference Δm^2_M and θ_M are influenced by this distinction between matter and antimatter. The result is that the mixing effects are enhanced or suppressed when utilizing neutrino or antineutrino beams (Fig. 1.5), respectively, providing a method to discern the sign of Δm^2_{ij}. Hence as the difference is defined as $m^2_j - m^2_i$, its sign depends on whether the mass eigenstate ν_j is heavier or lighter than ν_i leading to a positive or negative Δm^2_{ij} respectively.

The utilisation of the MSW effect induced by Earth matter in long-baseline experiments involves studying the appearance of electron neutrinos in a beam of muon neutrinos to discern the neutrino mass ordering. Oscillation probability for ν_e appearance is proportional to:

$$P_{\nu_\mu \to \nu_e} = \sin^2\theta_{23} \sin^2 2\theta_{13} \sin^2 \frac{\Delta m^2_{23} L}{4E}$$

Propagating in matter the vacuum mixing parameters are now replaced by effective mixing ones as defined in 1.14 where the vacuum angle is taken to be θ_{13} and the squared mass difference $\Delta m^2_{atm} \equiv \Delta m^2_{23}$. Since A embodies the difference for neutrino and antineutrino beam, from the known sign of V_{CC} the sign of Δm^2_{23} can be inferred by observing an enhancement or suppression of the oscillation.

At oscillation maximum, the $\nu_\mu \to \nu_e$ and $\overline{\nu_\mu} \to \overline{\nu_e}$ oscillation probabilities will be proportional to the $\sin^2 2\theta_M$. Thus, we expect to infer the sign by

$$\frac{\mathcal{P}_{\nu_\mu \to \nu_e}}{P_{\overline{\nu_\mu} \to \overline{\nu_e}}} = \begin{cases} > 1 & \text{NH} \\ < 1 & \text{IH} \end{cases}$$

This implies that experiments centred on the atmospheric mass gap Δm^2_{atm} and

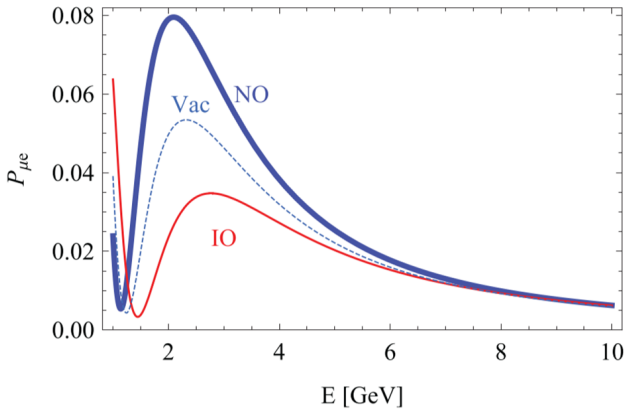

Figure 1.5: MSW effect on oscillation probability for ν_e appereance. In the normal ordering this resonant enhancement happens for neutrinos and in the inverted ordering it happens for antineutrinos, The ν_e and $\overline{\nu}_e$ enhanched samples, increase the capability to determine the mass ordering.

targeting either ν_e and $\overline{\nu}_e$ as final states, required a non-negligible ν_e fraction of the mass eigenstate ν_3. This fraction corresponds to the parameter of $\sin^2\theta_{13}$, underscoring that the capability to distinguish between normal or inverted ordering, using matter effect, relies on the measure of θ_{13}. Thus, alongside the determination of a CP violation, as seen in Sec. 1.3.3, also the determination of mass ordering hinges on the non-vanishing value of θ_{13}.

Remarkable constraints on the θ_{13} value have been reached in years from both reactor experiments, where the ν_e disappearance depends only on $\sin^2 2\theta_{13}$, and accelerator for ν_e appearance measurements that depend also on the δ_{CP} values. The resulting data consistently support a non-zero value for the PMNS matrix element U_{e3} with a global level of significance over the conventional 5σ threshold.

The Daya Bay in 2012 yielded a best-fit value of $\sin^2 2\theta_{13} = 0.086 \pm 0.041(stat.) \pm 0.030(sys.)$ effectively rejecting the hypothesis of $\sin^2 2\theta_{13} = 0$ at 94.6% C.L. [13]. Similar results were obtained by RENO [14] and DoubleCHOOZ **[double-chooz]** experiments shortly afterwards. Accelerators-based experiments results like T2K and MINOS instead, rely on the correlation between $\sin^2 2\theta_{13}$ and the CP violating phase δ_{CP} as shown in Fig. 1.6.

1.5 State of the art

Since Δm^2 is a natural constant, by adjusting the ratio L/E in experimental designs, sensitivity to neutrino mass-splitting can be maximized. The sensitivity is defined as

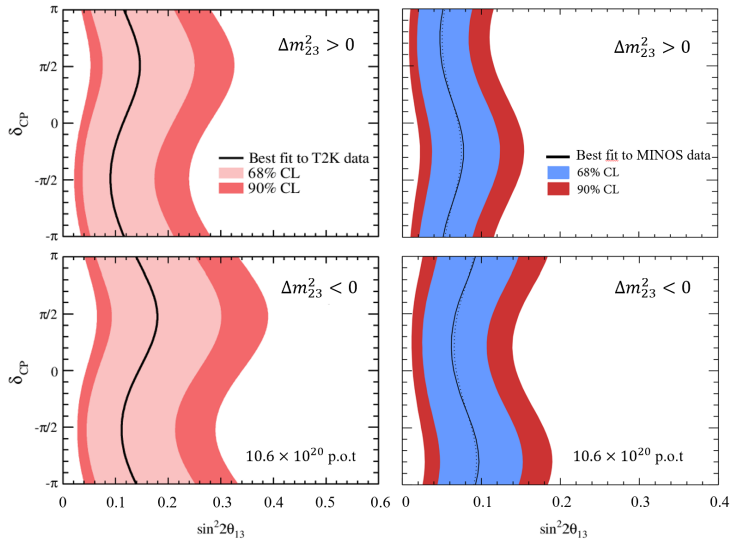

Figure 1.6: T2K (Left) and MINOS (Right) measured values of $\sin^2 2\theta_{13}$ for different values of δ_{CP}.

the value of Δm^2 for which:

$$\frac{\Delta m^2 L}{2E} \sim 1$$

The experiments are usually classified in two main types, based on the distance L between the neutrino beam-source and the detector

Short-Baseline (SBL) Depending on the neutrino source that can be either reactors, utilizing large $\overline{\nu}_e$ fluxes produced by heavy-nuclei β-decays and measuring the survival probability, or accelerator where the neutrino beam is produced by the decay of pions, kaons, and muons. Such detector placement is ideal to accurately measuring the initial neutrino flux and composition before significant oscillation occurs, ensuring that the observed neutrino behaviour is closely representative of the original beam and reducing un- certainties in initial flux measurements.

$$\frac{L}{E} \lesssim 10m/MeV \Rightarrow \Delta m^2 \gtrsim 0.1eV^2 \qquad \text{Reactor}$$
$$\frac{L}{E} \lesssim 1km/GeV \Rightarrow \Delta m^2 \gtrsim 1eV^2 \qquad \text{Accelerator}$$

Long- Baseline (LBL) These experiments exploit the same sources as SBL including also atmospheric neutrinos that providing a greater order of sensitivity on Δm^2. The far detector in these set-up is ideally located at the position of expected maximum oscillation, measuring the spectrum and flavour composition after the

neutrinos have oscillated.

$$\frac{L}{E} \lesssim 10^3 m/MeV \Rightarrow \Delta m^2 \gtrsim 10^{-3} eV^2 \qquad \text{Reactor}$$
$$\frac{L}{E} \lesssim 10^3 km/GeV \Rightarrow \Delta m^2 \gtrsim 10^{-3} eV^2 \qquad \text{Accelerator}$$
$$\frac{L}{E} \lesssim 10^4 km/GeV \Rightarrow \Delta m^2 \gtrsim 10^{-4} eV^2 \qquad \text{Atmospheric}$$

!

Further classification occur in considering the neutrino beam-source which instead in crucial to access to different oscillation parameters in the U_{PMNS} matrix

Solar neutrino sector

Thermonuclear reactions inside the sun's core are prolific sources of electron neutrino as products of both the pp chain and CNO cycle, whose result is:

$$4p + 2e^- \rightarrow^4 He + 2\nu_e + Q$$

Where Q is the amount of released energy per process.
This sector encompasses a variety of experiments, including solar neutrino observations and short-baseline reactor experiments like KamLAND, which are sensitive to the same oscillation parameters Δm^2_{12} and $\sin^2\theta_{12}$. Due to the specific L/E ratio the effects of Δm^2_{13} in oscillation probability is subdominant.

The Homestake experiment [15], along with subsequent radiochemical experiments like SAGE [16] and Gallex/GNO [17] between 1968 and 2007, measured the solar neutrino flux using electron neutrino capture on Chlorine or Gallium. The results were all in agreement, suggesting a deficit in the detected electron neutrino flux produced by the Sun. Later on, water Cherenkov detectors like Kamiokande [11]detected neutrinos by observing Cherenkov light produced by neutrino interactions in water, confirming the suppression of the expected neutrino flux.

The definitive answer regarding the nature of the neutrino flux deficit came from the Sudbury Neutrino Observatory (SNO) [12] in Canada. Utilizing heavy water, SNO was sensitive to three different neutrino interaction channels to compare the total electron neutrino flux:

- b$^{(\mathrm{CC})}{}_e + d \rightarrow p + p + e^-$ Cherenkov light on D2O $\Rightarrow \Phi(\nu_e)$

  $\nu_x + d \rightarrow p + n + \nu_x$ Neutron capture on deuteron $\Rightarrow \Phi\nu_e + \Phi(\nu_\mu) + \Phi(\nu_\tau)$

  $\nu_x + e^- \rightarrow e^- + \nu_x$ Cherenkov light on D2O $\Rightarrow \Phi\nu_e + 0.15\Phi(\nu_\mu) + \Phi(\nu_\tau)$

  and confirmed that the total neutrino flux matched predictions, proving that neutrinos oscillate en route from the Sun to Earth, with a significant fraction converting from ν_e to other flavours due to the matter effect.

Running since 2007, the Borexino experiment at Italy's Gran Sasso Laboratory has measured specific fluxes such as ^7Be and *pep* neutrinos, with results consistent with oscillation predictions. Along with this contribution KamLAND was designed to investigate the same energy range through the ν_e disappearance adding fundamental constraints over the solar parameters. In Figure 1.7 the allowed parameter regions from both solar data analysis and KamLAND are shown in the $\sin\theta_{12}^2 - \Delta m_{12}^2$.

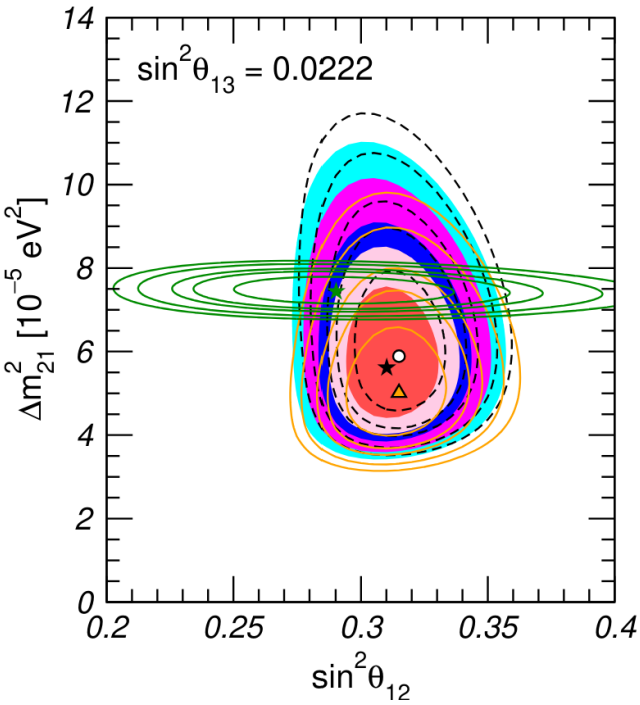

Figure 1.7: Allowed parameter regions (at $1\sigma, 90\%, 2\sigma, 99\%, 3\sigma$ C.L) for fixed $\theta_{13} = 8.6°$ from the analysis of KamLAND data (solid green contours with best fit marked by a green star) and from the combined analysis of solar data.

Reactor neutrino

Using large fluxes of electron anti-neutrino produced in heavy nuclei β^- decay, disappereance probability for $\overline{\nu}_e$ can be measured trough the inverse β decay reaction occuring in the detector:

$$\overline{\nu}_e + p \rightarrow e^+ + n$$

The positron undergoes to annichilation, resulting in the emission of two immediate photons. Meanwhile, the low-energy neutron travels through the doped scintillator materia until it is eventually absorbed by a nucleus emitting a delayed photon. The events are recontructed byt correlating the fast signal coming from positron to the delayed one coming from neutron absorption.

Energy of neutrinos from reactor sources, reach order of ∼MeV and are usually coupled to SBL detectors. Such values of L/E are enough to provide θ_{13} probes. Using inverse beta-decay (IBD) in Gadolinium-doped liquid scintillators to detect

reactor antineutrinos, a first upper limit on the mixing angle was achieved by Double Chooz, RENO [14] and Daya Bay [13]. A global data analysis. the best-fit value of θ_{13} for these experiments are summarized in Table 1.5

Experiment	$\sin^2\theta_{13}$
Double Chooz	0.088±0.033
RENO	0.082±0.009 ± 0.006
Daya Bay	0.0841±0.0027 ± 0.0019

Atmospheric neutrino sector

Interaction of cosmic rays with the atmosphere's nucleons leads to the creation of several products among which pions and kaons whose decay into muons bring a flux of muonic neutrinos.

At lower energies (around 1 GeV), the expected ratio of muon neutrinos and antineutrinos to electron neutrinos and antineutrinos $(\nu_\mu + \overline{\nu}_\mu)/(\nu_e + \overline{\nu}_e)$ should be 2.

Atmospheric neutrinos are well suited for studying neutrino oscillations due to their energy spectrum, which spans from a fraction of a GeV to over 100 GeV. They cover distances L ranging from a mere tens of kilometers to as much as $13 \cdot 10^3$ kilometers. Consequently, the ratio L/E varies from 1 km/GeV to 10^5 km/GeV. It is possible to view a single detector as having two distinct sources: a closer source consisting of downgoing neutrinos, and a more distant source of upgoing neutrinos. Under the hypothesis of no oscillation, the zenith angle distribution should exhibit symmetry between upward and downward directions, provided there are no other factors influencing the distribution of neutrino angles in relation to the vertical. On the other hand, any asymmetry observed between the upward and downward directions could suggest the presence of neutrino oscillations.

The key experiments in the detection of atmospheric neutrinos include the pioneering Kamiokande, its more advanced successor Super-Kamiokande, and the Irvine-Michigan-Brookhaven (IMB) experiment, all of which utilize water Cherenkov detectors. Initially, both Kamiokande and IMB observed a shortfall in the $(\nu_\mu + \overline{\nu}_\mu)$ flux, a phenomenon not observed by Frejus and NUSEX. Subsequent observations by Kamiokande indicated that this deficit varied with the zenith angle, thereby suggesting a distance-dependent oscillation of ν_μ into a third flavour, ν_τ This discovery was further substantiated by Super-Kamiokande, which accurately measured the oscillation parameters.

In more recent years, neutrino telescope experiments such as ANTARES [18] and IceCube [19] have refined the study of atmospheric neutrino oscillations by lowering their energy thresholds, thereby contributing additional precision to the measurements of these oscillation parameters. Both experiments utilize Cherenkov light detection emitted from neutrino interactions near the detectors to study atmospheric neutrinos.

In addition Long-Baseline (LBL) experiments can be used to improve results

on the atmospheric sector being sensitive to the same range of Δm^2. Among these experiments we mention the contribution od CHOOZ and Palo Verde, probing the $\overline{\nu_e}$ disappearance oscillation channel in the same region explored by atmospheric neutrinos, and of K2K and the Main Injector Neutrino Oscillation Search (MINOS) both searching for the ν_μ disappereance events.

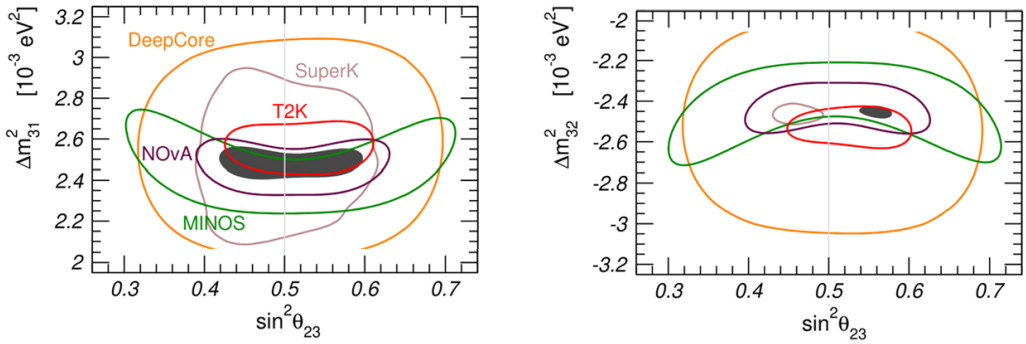

Figure 1.8: 2σ C.L allowed regions in the $\sin\theta_{23} - \Delta m^2_{3l}$ plane with $l = 1$ for Normal ordeing (Left) and $l = 2$ for Inverted ordering (Right) using appereance and disappereance data from both atmospheric and LBL experiments. To include costraints from reactor experiments a prior on the θ_{13} is included.

The early experiments, K2K [20] and MINOS [21] were crucial in confirming the ν_μ disappearance in regions consistent with atmospheric neutrino oscillations. K2K, which operated a neutrino beam produced by a 12 GeV proton beam and detected by a near detector as well as the Super-Kamiokande detector 250 km away, provided the first evidence of neutrino oscillations using an accelerator-produced beam.

MINOS further explored oscillations probability as a function of the E_ν using the NuMI beamline at Fermilab, detecting neutrinos in a detector located 735 km away. By $\nu_\mu \to \nu_\mu$ transitions costraints over Δm^2_{23} and $\sin^2\theta_{23}$ were improved.

NOνA [6] has added to this landscape by confirming electron neutrino appearance and exploring the neutrino and antineutrino oscillation parameters further, indicating deviations from maximal mixing and providing insights into CP violation in the neutrino sector. In addition to these, experiments like OPERA have successfully confirmed the appearance of ν_τ from a ν_μ beam, over a 732 km.

Looking forward, new projects such as DUNE, which will be inspect deeper in the next chapter, and Hyper-Kamiokande are expected to start operations, promising even more detailed studies of neutrino oscillations.

1.6 Mass Ordering

+In Section 1.3, we introduced a standard parametrization of the PMNS mixing matrix, which includes three mixing angles and one potential complex phase. The meaning of each matrix element is such that when a mass eigenstate ν_i interacts producing a charged lepton, the probability that this lepton is α corresponds to the ν_α fraction in ν_i denoted as $|U_{\alpha,i}|^2$ [1].

Various experimental approach described in the previous section, have enabled the determination of the different flavour fractions from the mixing parameters measurements together with squared-mass differences between them. To further elucidate the phases and signs of the U_{PMNS} matrix elements, and to highlight which types of experiments access to the measurement of different matrix elements, it is insightful to rewrite this matrix in the following decomposed form

$$U_{PMNS} = \underbrace{\begin{pmatrix} 1 & 0 & 0 \\ 0 & c23 & s23 \\ 0 & -s23 & c23 \end{pmatrix}}_{\text{Atmospheric}} \underbrace{\begin{pmatrix} c13 & 0 & s13e^{-i\delta_{CP}} \\ 0 & 1 & 0 \\ -s13e^{-i\delta_{CP}} & 0 & c13 \end{pmatrix}}_{\text{Cross}} \underbrace{\begin{pmatrix} c12 & s12 & 0 \\ -s12 & c12 & 0 \\ 0 & 0 & 1 \end{pmatrix}}_{\text{Solar}} \cdot \mathcal{P}$$

where $\mathcal{P}$ is a diagonal matrix accounting for two extra complex phases if neutrino are Majorana fermions.
Currently, the well-measured parameters include θ_{12}, θ_{13}, Δm^2_{12}, $|\Delta m^2_{3l}|$ and less precise measurements and an unresolved octant ambiguity are associated with the angle θ_{23}. Below is a brief description of their characterization, following what presented in the previous section.

$\boldsymbol{\theta_{12}}$ and $\boldsymbol{\Delta m^2_{12}}$ are measured with a precision of 2-3% in solar neutrino experiments focused on $\overline{\nu}_e$ disappearance events. The most reliable results are confirmed by the SNO [22] and KamLAND [4] experiments. From the above expression of the mixing matrix it can be seen that the solar neutrino dominating terms allowed to approximate $\theta_{12} \approx \theta_{SOL}$. This remains a valid approximation in two-family mixing since the ν_3 component in the electron neutrino is relatively small, allowing ν_e to be effectively treated as a mixture of the ν_1 and ν_2 mass eigenstates. As evident from the final results table, while not maximal, θ_{12} is significantly larger compared to the quark mixing angles observed in the CKM matrix.

$\boldsymbol{\theta_{23}}$ and $|\boldsymbol{\Delta m^2_{23}}|$ can be inferred from the disappearance of ν_μ and $\overline{\nu}_\mu$ in accelera-

tor experiments such as T2K, NOνA, and MINOS, as well as in studies of atmospheric neutrinos from Super-Kamiokande. Atmospheric neutrinos predominantly influence the mixing terms driven by θ_{23}-, such that we can refer to them as θ_{ATM}. The results indicate a broad mixing range, with θ_{23} between 37° and 53°, and the most fitting value being 45°, which corresponds to maximal mixing.

$\boldsymbol{\theta_{13}}$ is defined such that $|U_{ei}|^2 = \sin^2\theta_{13}$. This angle's measurements are primarily conducted through short-baseline reactor experiments probing a $\overline{\nu_e}$ disappereance like Double Chooz, RENO, and Daya Bay, and are expected to be further refined in accelerator experiments such as T2K , Noνa and DUNE. This parameter is pivotal not only for the real term in U_{PMNS} but also involves the CP-violating phase that enters the matrix solely in conjunction with $\sin^2\theta_{13}$. Finding a non-zero θ_{13} and establishing its magnitude is one of the objectives for future long-baseline neutrino experiments.

Best fit based on the latest result on mixing parameters and neutrino masses performed in three family frameworks are listed in Table 1.9 taken from [23].

	Normal Ordering (best fit)		Inverted Ordering ($\Delta\chi^2 = 9.1$)	
	bfp $\pm 1\sigma$	3σ range	bfp $\pm 1\sigma$	3σ range
$\sin^2\theta_{12}$	$0.307^{+0.012}_{-0.011}$	$0.275 \to 0.344$	$0.307^{+0.012}_{-0.011}$	$0.275 \to 0.344$
$\theta_{12}/^\circ$	$33.67^{+0.73}_{-0.71}$	$31.61 \to 35.94$	$33.67^{+0.73}_{-0.71}$	$31.61 \to 35.94$
$\sin^2\theta_{23}$	$0.454^{+0.019}_{-0.016}$	$0.411 \to 0.606$	$0.568^{+0.016}_{-0.021}$	$0.412 \to 0.611$
$\theta_{23}/^\circ$	$42.3^{+1.1}_{-0.9}$	$39.9 \to 51.1$	$48.9^{+0.9}_{-1.2}$	$39.9 \to 51.4$
$\sin^2\theta_{13}$	$0.02224^{+0.00056}_{-0.00057}$	$0.02047 \to 0.02397$	$0.02222^{+0.00069}_{-0.00057}$	$0.02049 \to 0.02420$
$\theta_{13}/^\circ$	$8.58^{+0.11}_{-0.11}$	$8.23 \to 8.91$	$8.57^{+0.13}_{-0.11}$	$8.23 \to 8.95$
$\delta_{\rm CP}/^\circ$	232^{+39}_{-25}	$139 \to 350$	273^{+24}_{-26}	$195 \to 342$
$\frac{\Delta m^2_{21}}{10^{-5}\ \mathrm{eV}^2}$	$7.41^{+0.21}_{-0.20}$	$6.81 \to 8.03$	$7.41^{+0.21}_{-0.20}$	$6.81 \to 8.03$
$\frac{\Delta m^2_{3\ell}}{10^{-3}\ \mathrm{eV}^2}$	$+2.505^{+0.024}_{-0.026}$	$+2.426 \to +2.586$	$-2.487^{+0.027}_{-0.024}$	$-2.566 \to -2.407$

Figure 1.9: Three-flavor oscillation parameters from global data as of March 2024 for both the Normal and Inverted orderings. The results are obtained with the inclusion of the atmospheric neutrinos results provided by the Super-Kamiokande collaboration.

In the oscillation model presented there are two independent squared mass differences conventionally addressed to Δm^2_{21} and Δm^2_{32}. Global fit to the data from neutrino oscillation experiments revealed a significant gap in the magnitudes of two of them: $\left|\Delta m^2_{12}\right| << \left|\Delta m^2_{32}\right|$. Observations of atmospheric neutrinos have provided an initial measurement indicating that Δm^2_{13} is of the same order of magnitude as Δm^2_{32}. As detailed in Sec. 1.4, matter effects offer an experimental method that is sensitive to the sign of Δm^2_{ij}, as demonstrated by solar neutrino experiments. The sign of Δm^2_{23} instead, remains elusive as it is typically measured in vacuum oscillations. This

ambiguity leads to two potential configurations for neutrino mass ordering, arising from the sign of Δm^2_{31}

$$m_1 < m_2 < m_3 \Rightarrow \Delta m^2_{31} > 0 \qquad \text{Normal}$$
$$m_3 < m_1 < m_2 \Rightarrow \Delta m^2_{31} < 0 \qquad \text{Inverted}$$

The comprehensive scenario emerging from these results is illustrated in Fig. 1.10.

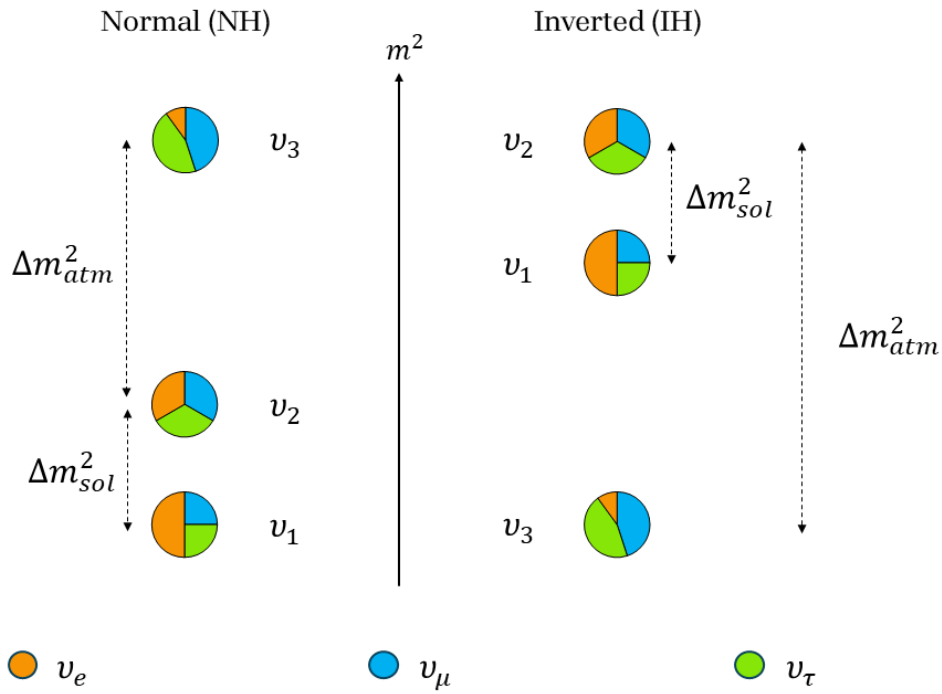

Figure 1.10: Schematic representation of the three-neutrino squared-mass spectrum including the flavour content in each mass eigenstates, obtained from experimental results on atmospheric and solar neutrinos.

Long-baseline neutrino oscillation experiments play a crucial role in determining the neutrino mass ordering by utilizing matter effects as the beams travel underground through the Earth. Notably, experiments like HyperKamiokande and DUNE are designed specifically to address this problem. The determination of the neutrino mass ordering can also be approached by studying the appearance of ν_e within a muon neutrino beam: changing from neutrinos to antineutrinos inverts the effects of both δ_{CP} phase and the matter enhancement. By properly tuning the ratio L/E_ν and taking into account the known mixing angles, is possible to separate the effects of CP violation and matter from the sign of the mass difference, thereby establishing the correct neutrino mass ordering.

Current global fit results from a combination of long-baseline experiments (NOνA, MINOS, T2K), reactor experiments (Daya Bay, RENO, Double Chooz), and solar neutrino experiments (SNO, Super-Kamiokande, Borexino) increasingly support the

normal mass ordering by a $\Delta\chi^2$ values of approximately 2 as shown in Fig. 1.11.

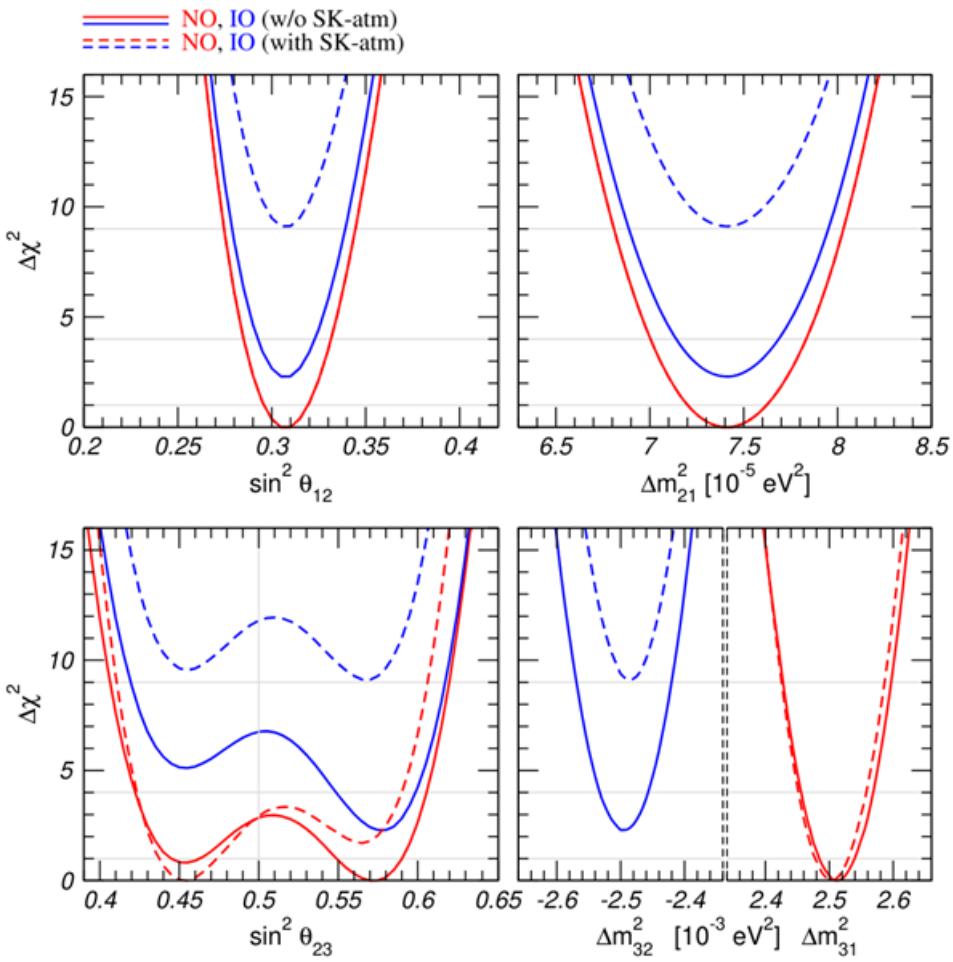

Figure 1.11: Global three-neutrino oscillation analysis. As atmospheric mass-squared splitting it used Δm^2_{31} for NO and Δm^2_{32} for IO.

Chapter 2

DUNE

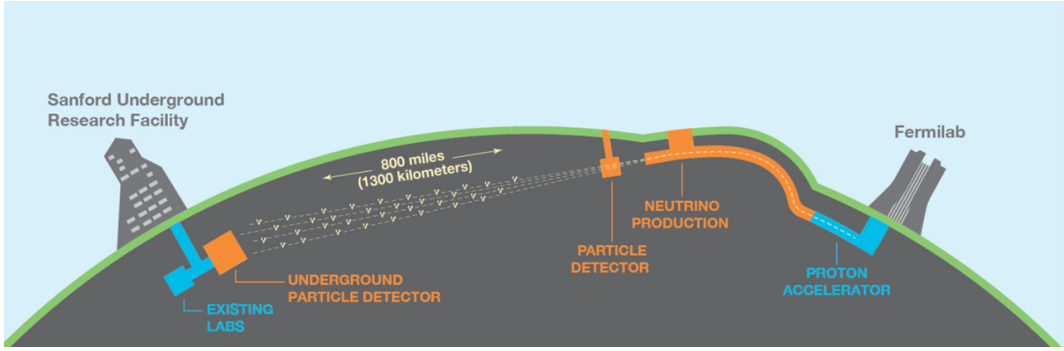

Figure 2.1: DUNE experimental set-up. The LBNF beamline is situated at Fermilab, in Illinois, and the DUNE detectors in Illinois and South Dakota, separated by 1300 km.

The Deep Underground Neutrino Experiment (DUNE) is a next-generation, long-baseline (LBL) neutrino oscillation experiment, engineered to exhibit high sensitivity to neutrino oscillations. The design features the most intense neutrino beam to date, achieving up to 2.4 MW, and includes two experimental sites: the Near Detector (ND) complex at Fermilab in Batavia, Illinois, and a multi-kiloton Far Detector based on liquid argon time projection chambers (LArTPC) comprising a total mass of 70 kton, at the Sanford Underground Research Facility (SURF) in South Dakota, approximately 1300 km away and $\sim$ 1500 m underground.

DUNE will pursue a broad scientific program: its primary objectives include an exhaustive investigation of neutrino oscillation and the precise measurement of mixing parameters, along with determining the neutrino mass ordering and CP-violating phase. The secondary programme includes the study of neutrinos from core-collapse supernovae and the search for signatures Beyond the Standard Model (BSM), such as nucleon decays.

In this chapter we outlines the goals of the DUNE scientific agenda, the general design and setup of the two sites, and the assumptions and methods used to perform the measurements.

2.1 DUNE Design

To achieve its physics goals, DUNE will utilize the most intense wide-beam (anti)neutrino beam, a multi-kiloton Far Detector based on LArTPCs technology for high-precision reconstruction of neutrino interactions, and a Near Detector, essential for constraining systematic uncertainties to unprecedented levels. To fully execute its compehensive scientific agenda DUNE will require two consecutive phases of operation resumed as folllow:

PHASE-I In its initial phase, DUNE will begin to address some early physics goals using an upgradable 1.2 MW proton beam, only two FD modules with a total of 20 kilotons of fiducial mass, and a provisional setup for the near detector complex (ND-LAr, TMS, SAND).

PHASE-II Transition involves upgrade to 2.4 MW neutrino beam and the complete deployment of its experimental infrastructure: four FD modules to reach 40 kilotons fiducial mass, and a fully-configured near detector, improved with ND-GAr.

2.1.1 Neutrino beam

DUNE will receive its neutrino beam provided by the Long Baseline Neutrino Facility (LBNF) at Fermilab. Initially operating at a proton beam power of 1.2 MW from Fermilab's Main Injector via the Proton Improvement Plan II (PIP-II), LBNF is designed for a future upgrade to 2.4 MW in Phase-II, handling proton energies between 60 and 120 GeV. The accelerated protons strike on graphite fixed-target, generating secondary particles primarily consisting of $\pi^{\pm}$ and $K^{\pm}$ which are then focused by magnetic horns into a 194 m long decay pipe. Here, pions decay predominantly into $\mu^{+} + \nu_{\mu}$ or $\mu^{-} + \overline{\nu}_{\mu}$ depepending on the pions' charge.

An absorber at the pipe's end significantly filters out most muons, leaving a beam primarily made of ν_{μ} or $\overline{\nu}_{\mu}$ with minor contamination from electron neutrinos stemming from residual kaons and muon decays. By adjusting the horn's magnetic field polarity, the facility can selectively focus on either positive or negative particles, enabling the beam to switch between neutrino and antineutrino modes, referred to as Forward Horn Current (FHC) and Reverse Horn Current (RHC), respectively.

This setup allows the horns to select a range of neutrino energies peaking at about 2-3 GeV and extending up to 10 GeV, crucial for covering the first two oscillation maxima and distinctive aspect of the DUNE experiment. Expected neutrino and anti-neutrino fluxes together with the flavour composition are shown in Fig. 2.2.

2.1.2 Near Detector

The Near Detector of DUNE is situated 574 meters from the neutrino beam source at Fermilab and is instrumented to measure the neutrino beam rate and spectrum imme-

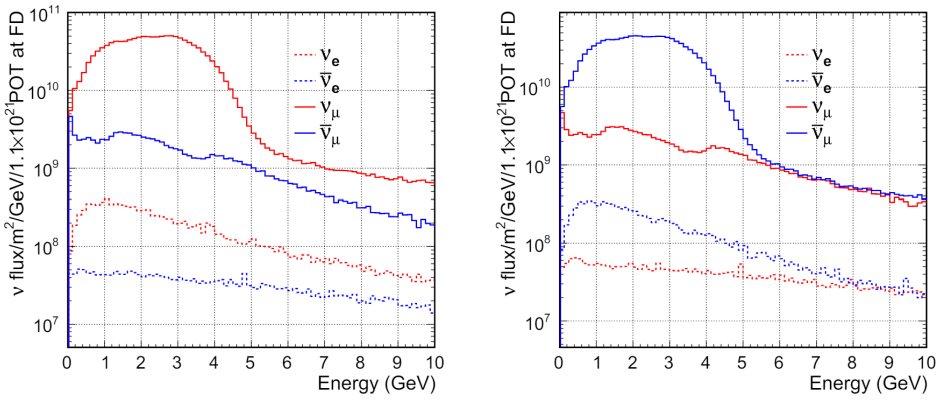

Figure 2.2: Expected fluxes as a function of beam energy at the FD for neutrino mode (left) and antineutrino mode (right).Taken from [24].

diately after production, before the neutrinos undergo oscillation. This measurement is crucial as it establishes the initial conditions of the neutrinos, serving as a baseline for comparison with the oscillated neutrinos detected at the (FD). Moreover, the ND embarks on an independent physics program, extending beyond neutrino oscillation studies to probe foundational aspects of the Standard Model, such as electroweak interactions and quantum chromodynamics, BSM framework measuremetns, including searching for non-standard interactions, sterile neutrinos, dark photons, and other exotic particles.

The ND complex is composed of three detectors, each with specific roles and configurations tailored to DUNE's experimental phases. The ND features the ND-LAr (ArgonCube), the Temporary Muon Spectrometer (TMS), which will be replaced by the high-pressure gaseous Argon TPC (ND-GAr) in PHASE-II surrounded by an electromagnetic calorimeter (ECAL) in a 0.5 T magnetic field. Both the ND-LAr and the TMS/ND-GAr are mounted on rails, being a movable off-axis allowing to participate in the Precision Reaction-Independent Spectrum Measurement (PRISM) of off-axis neutrinos. The third detector, System of on-Axis Neutrino Detection (SAND) consists of a 3D-scintillator low-density target inside a superconducting magnet at 0.6 T and electromagnetic calorimeter (ECAL) from KLOE experiment. SAND continuosly monitors the flux of neutrinos, providing an essential means for cross-validation and systematic verification of the neutrino flux results from ND-LAr. The DUNE Near Detector is depicted in Fig. 2.3 for both on and off-axis configuration

ND-LAr

Is a Liquid Argon Time Projection Chamber (LArTPC) organized into a 5×7 matrix of small, optically isolated TPC modules, each equipped with individual pixelated readouts that provide precise timing information to minimize event overlap. This arrangement optimizes event reconstruction in the dense neutrino flux environment,

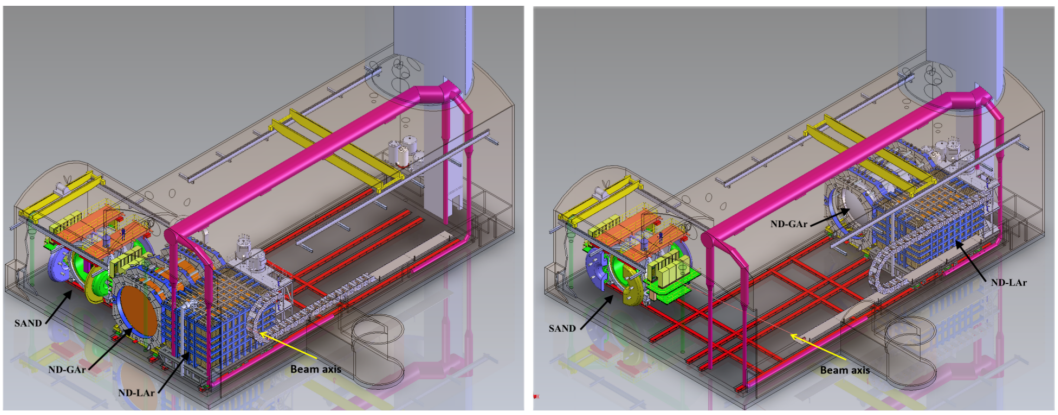

Figure 2.3: 3D view of the DUNE Near Detector hall: (left) all detectors are in onaxis position; (right) ND-LAr and ND-GAr are in an off-axis position, and SAND remaining on axis(right) [24]

like the one at the ND. With a fiducial mass of 67 tons and an active volume of $5 \times 7 \times 3m^3$, the ND-LAr aims to provide high statistics by detecting $10^8 \nu_\mu$ CC events per year.

The large volume contains most of hadron interactions, but its acceptance decreases for muons with measured momenta higher than 0.7 GeV/c. To address this, the LArTPC is complemented by the TMS/Nd-GAr, to measure muon momentum and charge—key for accurate neutrino energy assessments. Having the same target nucleus as the Far Detector, the ND-LAr reduces sensitivity to nuclear effects and systematic errors in FD's signal.

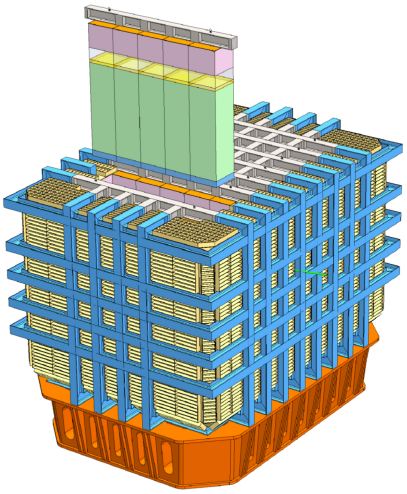

Figure 2.4: Drawing of the ND-LAr detector, with details one of the seven lines of five modules.[25]

ND-Gar

ND-GAr is a high-pressure gaseous argon time projection chamber (HPgTPC) encased within an electromagnetic calorimeter (ECAL) in a 0.5 T magnetic field. With a fiducial volume of ~ 1 ton, it is expect to detect 1.6×10^6 ν_μ CC events annually in an on-axis configuration. The interaction of neutrinos with gaseous argon provides a distinct sample of $\nu - Ar$ events studied at a lower energy threshold compared to the liquid detector. ND-GAr introduces different systematic uncertainties, enhances the identification of charged pions and protons, and allows for better analysis of primary interaction products.

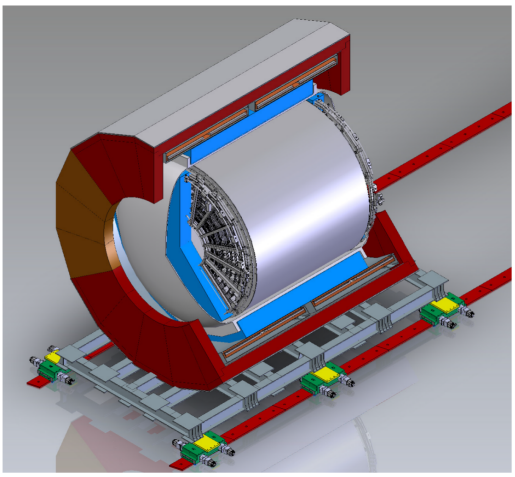

Figure 2.5: Schematic of ND-GAr with the HPgTPC, its pressure vessel, the ECAL, the magnet, and the return iron.[25]

SAND

The System for on-Axis Neutrino Detection (SAND) is a multi-purpose detector dedicated to precision tracking and calorimetry functions. It consists of an inner volume featuring a small LAr active target (~ 1 ton) GRAIN, and a low-density tracker (STT) based on Straw Tubes with distributed target mass, both housed in an ECAL encased in a 0.6 T superconducting magnet repurposed from the KLOE experiment (Fig.2.6). The tracker's design is particularly effective at isolating small energy depositions from neutrons, enhancing the ability to include neutrons in event reconstruction, crucial to determine low-neutrino flux. The on-axis fixed position of SAND provides systematic cross-checks of the flux against measurements from ND-LAr and ND-GAr when they are moved off-axis. Additionally, SAND's unique technology and target materials, distinct from those in the Far Detector, contribute valuable data for developing interaction models and understanding nuclear effects. Detailed design and physics goals of SAND will be discussed in Chapter 3.

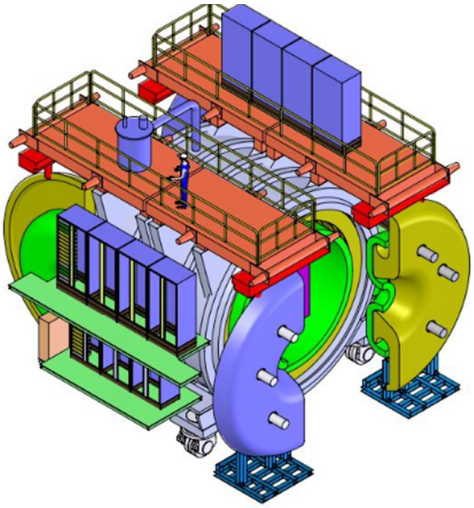

Figure 2.6: SAND engineering model

2.1.3 Far Detector

The DUNE Far Detector (FD) complex will be installed at approximately 1.5 km underground at SURF, South Dakota (USA). It involves four liquid argon time projection chamber (LArTPC) modules, housed within a cryostat of internal dimension of 18.9×17.8×65.8 meters,with a mass of about 17.5 kton each (10 kton fiducial mass).

For DUNE Phase-I, only two modules, FD1 and FD2, are planned. The other modules, FD3 and FD4, will be operational in Phase-II. Modules FD1 and FD2 are both single-phase LAr TPCs, with different technological implementations. The first module FD1 is a traditional Horizontal-Drift LArTPC whose design was previously tested and validated at the CERN Neutrino Platform using the ProtoDUNEs detector, which employs a prototype, approximately 20 times smaller than the actual FD modules. The second module FD will employ an innovative single-phase Vertical-Drift design where the cathode is placed at the bottom and the anode read-out is at the top of the cryostat.

The designs for the third and fourth modules, FD3 and FD4, are still under development and will be deployed in PHASE-II.

Horizontal-Drift

The inner volume of the detector is segmented into four drift regions by alternating three anode plane assemblies (APAs) and two cathode plane assemblies (CPAs), each drift region measuring 58.2 m long, 3.5 m wide, and 12.0 m high(Fig. 2.7). A uniform electric field of 511 V/cm is maintained across these regions by biasing the cathodes at -180 kV, drifting the ionization electrons horizontally towards the anode planes. Each APA is dual-sided, featuring three stratified layers of active wires arrayed in a

grid pattern on each side. The initial two layers, labelled U and V, generate bipolar induction signals as electrons traverse them, while the final layer X produces an unipolar singal.

Timing data is provided by a photon detection system called X-ARAPUCA [26], located behind each anode wire plane. This system utilizes a dichroic short-pass filter to modify the wavelength of the scintillation photons and confine them within an enclosed chamber, where SiPMs collect the light signal.

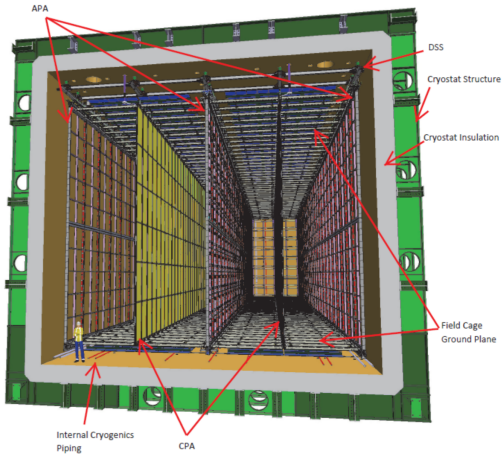

Figure 2.7: Drawing of the Horizotal-Drift FD1 showing the alternating anode (APA) and cathode (CPA) plane assemblies howing the alternating anode (A) and cathode.

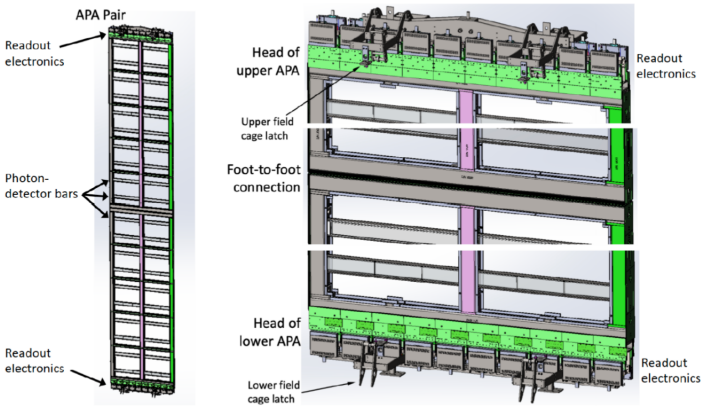

Figure 2.8: Left: one unit of the APA wall, composed by two APAs linked together. Right: zoomed view of the top and bottom ends of the left figure showing the readout electronics of the APAs [27]

Vertical-Drift

The FD2 module is a vertical drift LArTPC whose schematic drawing is shown in Fig. 2.9. In this design, a horizontal cathode plane is centrally suspended within the cryostat, creating two vertically stacked volumes, each 6.5 meters in height. Ionization

electrons drift vertically from the cathode towards anodes positioned at the top and bottom of the detector.

The anodes consist of perforated printed circuit boards (PCBs) to prevent deformation when mounted horizontally. Each anode features a two-PCB configuration: the first PCB includes a shielding and an initial induction plane, while the second PCB contains the second induction and collection planes. The top anode is adjustable, supported by a stainless steel frame suspended from Kevlar wires, maintaining a deformation of less than 10 mm over 3 meters. The bottom anode is fixed on the cryostat floor.

Readout electronics differ between anodes, with the top electronics located in the cryostat chimney and the bottom ones beneath the support frame. The photon detection system collects argon scintillation light for triggering and timing information, with x-ARAPUCA modules specifically redesigned for this vertical drift configuration. This design offers a slightly larger instrumented volume (13.513.060m^3) and facilitates simpler construction and installation compared to the horizontal drift module.

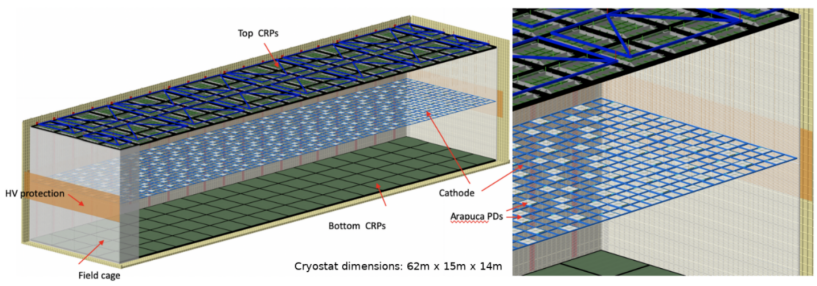

Figure 2.9: Left:Sketch of the full vertical drift module FD2. Right: close-up to the mounting of the photo-sensor on the cathode plane.

2.2 Physics Program

The DUNE experiment is one of the largest LBL neutrino experiments, featuring the world's most intense neutrino beam and a massive liquid argon detector. This setup supports a broad scientific program aimed at significantly advancing current knowledge and achieving multiple scientific objectives:

Primary goals The determination of neutrino mass ordering given the sign of $\left|\Delta m^2_{23}\right|$, measurements on δ_{CP} phase accounting for charge-parity violation, determination of the octant in which θ_{23} relies and sensitive test on the three-neutrino paradigm. Along with searches for physics Beyond the Standard Model suuch as searches for proton decay and detection of ν_e flux from core-collapse supernovae and other low-energy neutrinos.

Ancillary goals LBL oscillation studies with sensitivity to BSM channels, including non-standard interactions (NSIs), violations of charge, parity, and time reversal symmetry (CPT), sterile neutrinos, heavy neutral leptons, and searches for tau neutrino appearance. In addition Dark Matter researches using signatures from both the ND and FD can be perfomed as well as studies on neutrino cross-sections and nuclear effects.

2.2.1 Standard neutrino oscillation

DUNE experiment is designed to perform long baseline neutrino physics through $\nu_\mu \to \nu_e$ oscillations events. The oscillation probability in the three-flavour paradigm for the sub-channel muon to electron through matter is given in Eq. 1.10, and resulted to be sensitive to multiple parameters of the PMNS matrix. In the case of sub-channel studiend by DUNE:

$$\begin{aligned}\mathcal{P}_{\nu_\mu \longrightarrow \nu_e} = & \sin^2\theta_{23}\sin^2 2\theta_{13}\frac{sin^2(\Delta_{31}-aL)}{(\Delta_{31}-aL)^2}\Delta^2_{31} \\ & + \sin 2\theta_{23}\sin 2\theta_{13}\sin 2\theta_{12}\frac{\sin(\Delta_{31}-aL)}{(\Delta_{31}-aL)}\Delta_{31}\frac{\sin(aL)}{aL}\Delta_{21}\cos(\Delta_{31}+\delta_{CP}) \\ & + \cos^2\theta_{23}\sin^2 2\theta_{12}\frac{\sin^2(aL)}{(aL)^2}\Delta^2_{21}\end{aligned} \tag{2.1}$$

where we adopted the notation $\Delta_{ij} = \Delta m^2_{ij} \cdot L/4E_\nu$ and $a = G_F N_e/\sqrt{2}$.

The δ_{CP} and the parameter a for the MSW effect switch signs when transitioning from muon to antimuon beams, introducing a neutrino-antineutrino asymmetry due to both the CPV and MSW effects. From the equation, the sensitivity to the sign of Δm^2_{13}, and consequently to the mass ordering, is influenced by matter effects. In the GeV energy range, the asymmetry from the MSW effect increases with the baseline length L as the neutrinos travel through more matter. The magnitude of δ_{CP} is

measured through the Jarlskog invariant, as seen in Sec. 1.3.3, by constraining the value of $\sin^2 2\theta_{13}$.

This measurement affects both the amplitude and phase of the oscillation. The ratio L/E was chosen such that the degeneracy between these two asymmetries is resolved, thus CPV and mass ordering can be determined simultaneously. In Figure 2.10, the oscillation probability channel for the DUNE baseline length is displayed. A significant asymmetry between the neutrino and antineutrino beams is evident. At approximately 1300 km, this asymmetry reaches about ±40% in the region of peak flux, which is substantially greater than the maximal asymmetry induced by the δ_{CP} phase. To assess the sensitivities of each oscillation parameter resolution, δ_{CP},

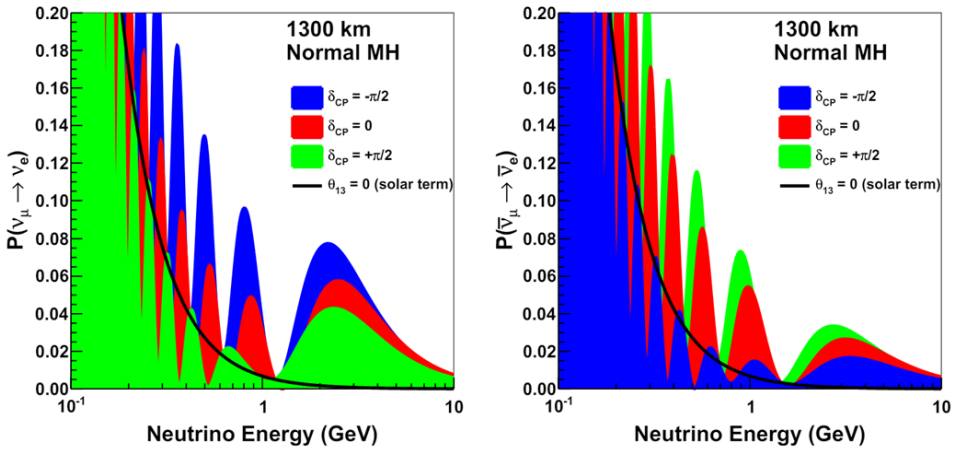

Figure 2.10: Appereance probability from ν_e and $\overline{\nu}_e$ at the DUNE baseline of 1285 km as a function of neutrino energy for different values of δ_{CP} asusming a normal ordering.

the θ_{23} octant, and the mass ordering, common exposure and staging assumptions have been adopted. The analyses are based on simultaneous fitting of the energy spectrum for the FD, utilizing selected samples from the Near Detector ND for both disappearance and appearance events with an equal running in ν_μ and $\overline{\nu}_\mu$ beam mode. Each measurement assumes only normal ordering throughout and a nominal exposure corresponding to 7, 10, and 15 years of data collection. For each measurement, the nominal result is represented as the median of the fit results, and the uncertainties, depicted as transparent bands, are calculated to be interval containing 68% of the fit results, providing a standard measure of precision.

For a non-maximal CP violation sensitivities are expected to increase starting from 3σ for half of the values of the δ_{CP} values after first 5 years of running, 5σ for same values after 10 years, up to 3σ CL for 75% in 13 years of total exposure, as visible in th right panel of Fig. 2.12.

The CP violation significance as a function of δ_{CP} phase, for the same exposure years, is instead shown in Fig. 2.11. Maximum sensitivity is reached for $\delta_{CP} = \pm\pi/2$ and decrease approaching CP-conserving values. To exploit mass ordering sensitivity

same, approach used for CP violation analysis is employed. Left panel of Fig. 2.11 shows the mass-ordering significance for different values of exposure as a function of the true δ_{CP} value. With about three years of exposure ($\sim$ 100 kt-MW-years) DUNE will be able to reach a 5σ CL independently from the value of the CP-violating phase value. In Figure 2.12 is instead shown the significance for $\delta_{CP} = -\pi/2$, and for 100% of its possible values, as a function of exposure in kt-MW-years.

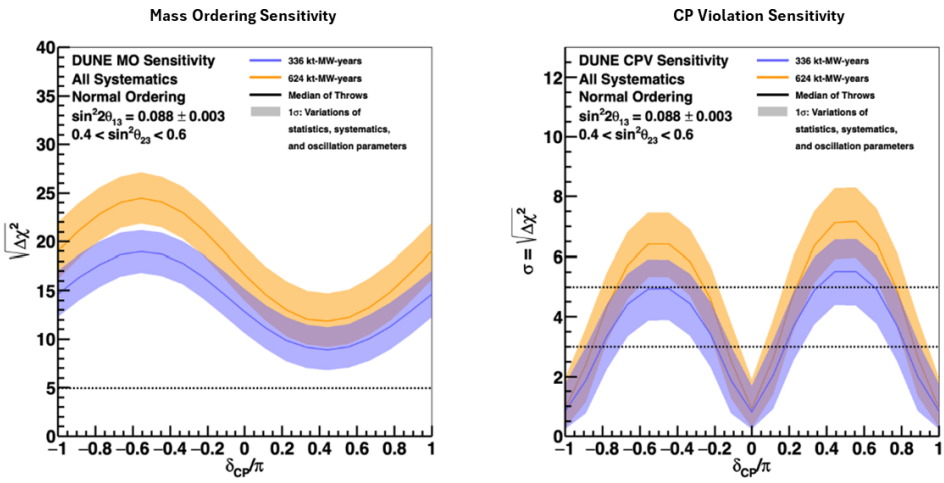

Figure 2.11: Left: Significance of the DUNE determination of the neutrino mass ordering , as a function of the true value of δ_{CP}. Right: Significance of the DUNE determination of CP-violation ($\delta_{CP} \neq 0, \pi$) as a function of the true value of δ_{CP}. Both for seven (blue) and ten (orange) years of exposure.

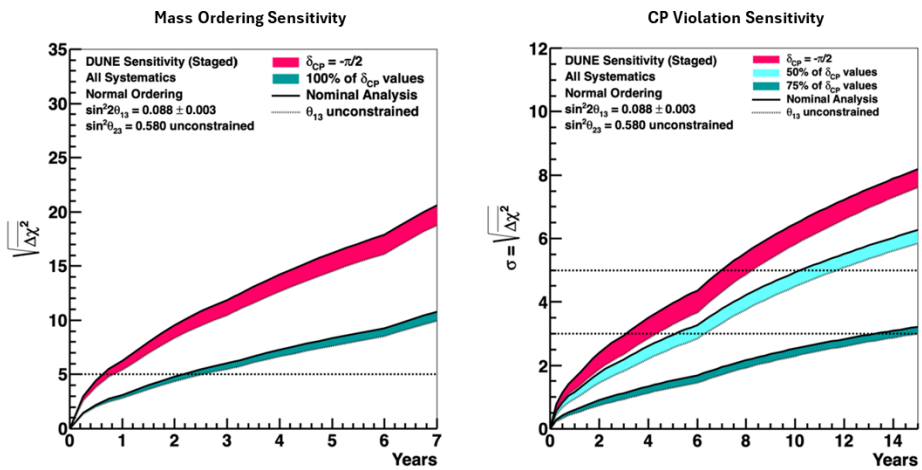

Figure 2.12: Left: significance of the DUNE determination of the neutrino mass ordering for $\delta_{CP} = \pi/2$, and for 100% of its possible true values, as a function of time in years. Right: significance of the DUNE determination of CP-violation for $\delta_{CP} = -\pi/2$, and for 50% and 75% of its possible values, as a function of exposure in time.

Chapter 3

SAND

The System for On-Axis Neutrino Detection (SAND) is one of the three detectors in the ND complex of the DUNE experiment. SAND features a 0.6 T superconducting magnet and an electromagnetic calorimeter made of lead and scintillating fibres, both repurposed from the KLOE experiment. The inner magnetized volume will host a small 1-ton LAr active target (GRAIN) in the upstream region and a target/tracker system made of Straw Tubes (STT) alternating with thin passive target planes made of different materials.

SAND's primary function is to monitor the neutrino beam close to the production point, perform measurements of the beam spectrum to compare with FD flux, and to control systematic uncertainties that could affect the oscillation analysis. The internal tracking system and the small liquid argon (LAr) target will provide neutrino interactions across various nuclear targets, such as argon (Ar), polyethylene (CH2), and carbon (C). This extended data can be used to study interaction models and constrain nuclear effects. Additionallly, inner tracker is designed to incorporate neutrons in event reconstruction, accessing regions of phase space in neutrino interactions not previously seen in experiments. This capability enhances the resolution of energy transferred to the nucleus, aiding in flux determination and potential improvements in nuclear modeling [28].

3.1 Design

3.1.1 Magnet

SAND's magnet produces a uniform 0.6 T magnetic field over a cylindrical volume of 4.8 m of diameter and 4.3 m of length [29] . This is achieved with a single conductor layer coil that operates at a nominal current of 2902 A, placed inside a cryostat 4.40 meters long, positioned within an iron yoke. Cooling is managed through thermo-siphoning cycles using helium gas at 5.2 K injected at 3 bar from a cryogenic service turret positioned at the top of the yoke, and liquified into a reservoir in thermal

contact with the coil. Liquid He is used to directly cool down the current leads while gaseous helium is used for radiation shields. The vertical cross-section of the KLOE experiment, to display the coils and cooling system design, is shown in Fig. 3.1.

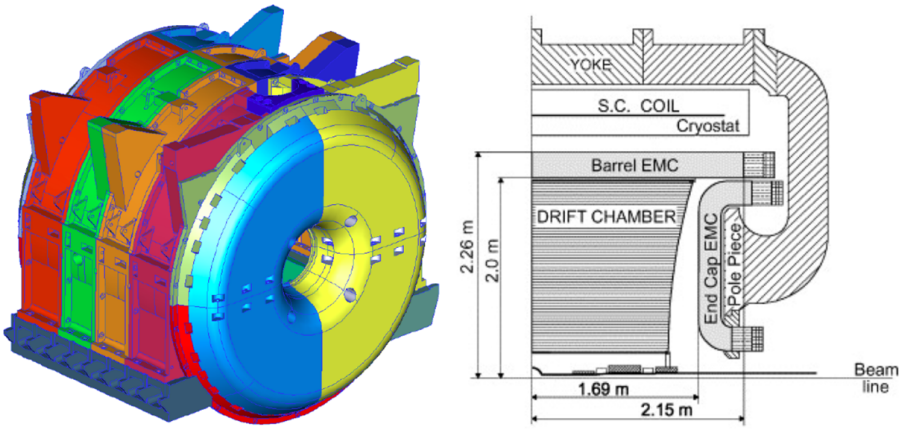

Figure 3.1: The KLOE detector: (left) 3D engineering CAD model of the magnet and (right) vertical cross section

3.1.2 ECAL

The electromagnetic calorimeter (ECAL) of SAND, repurposed from the KLOE experiment, is a lead scintillating fiber sampling calorimeter which ensures high light transmission, and sub-nanoseconds timing accuracy. The design consists of a

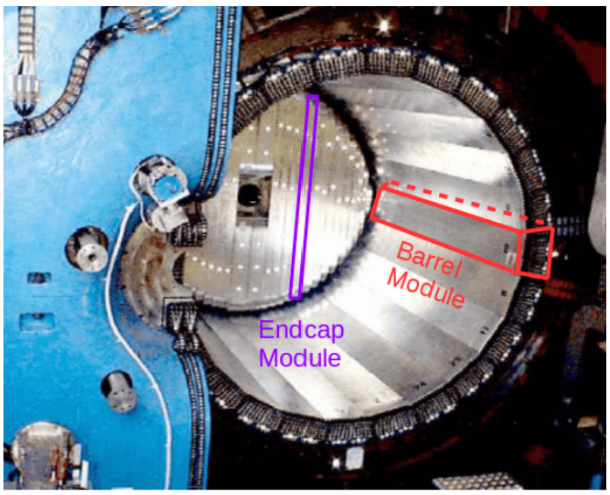

Figure 3.2: A view of the KLOE calorimeter shows the far endcap closed with vertically oriented ECAL modules.

cylindrical barrel calorimeter with 24 modules, each measuring 4.3 m long and 23 cm thick having a trapezoidal cross-section characterized by two bases of 52 cm and

59 cm. It is completed with two C-shaped endcaps, made of 32 vertically oriented modules each, of varying lengths (0.7 to 3.9 meters) and 23 cm of thickness. The endcaps modules are bent horizontally to insert the barrel calorimeters and host photo-tube axes parallel to the magnetic field. This configuration leaves no inactive gaps and ensures a total 4π hermicity. At both ends of the modules, light guides are placed in a 5x4 grid such that each cell of fibers is read using photomultipliers (PMTs).

All modules alternate approximately 200 layers of 0.5 mm thick lead foils and 200 layers of 1 mm diameter scintillating fibers, glued together with a compatible epoxy. The overall thickness is around 15 radiation lengths and the average density is 5 g/cm^{-3}. Performances of the ECAL were estimated during KLOE running phase resulting in the following energy and time resolution[25]:

$$\frac{\sigma}{E} = \frac{5.7\%}{\sqrt{E(\text{GeV})}} \qquad \sigma_t = \frac{54}{\sqrt{E(\text{GeV})}}\ \text{ps}$$

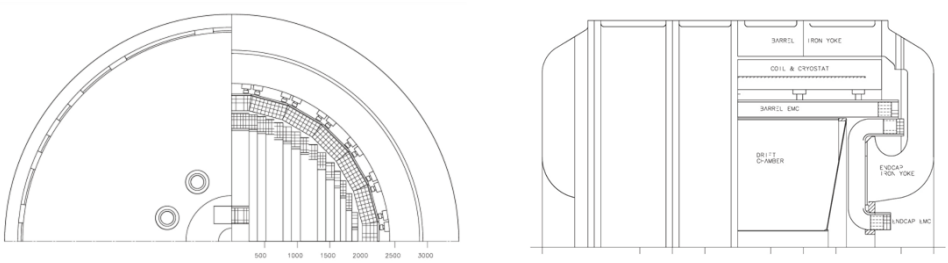

Figure 3.3: Front (left) and side (right) schematic representation of the KLOE calorimeters. Light guides location inside the magnet is shown. Units are in mm [30]

3.1.3 Straw Tube Tracker

The inner volume of SAND utilizes Straw Tube Tracker (STT) technology, filling the internal magnetic volume except for the upstream region, which houses a small liquid argon target described later in SECTION. The STT volume acts as a target for (anti)neutrino interactions and provides a tracking system to accurately reconstruct the momenta of charged particles. The STT system is designed as a modular detector, with neutrino targets physically separated from the tracking system (straw tubes), whose mass contribution is negligible. The target mass is uniformly distributed throughout the tracking volume, maintaining an average density low enough (0.18 g/cm^3) to be transparent to the final state particles produced in neutrino interactions. Figure 3.4 shows the standard configuration of a single module made of:

- A 5 mm thick solid polypropylene (CH_2) target slab, customizable in thickness to adjust the target mass and density as required;

- A polypropylene radiator consisting of 105 foils, each 18 μm thick, alternated with air gaps of 117 μm. These enhance particle identification capabilities through transition radiation, ensuring effective e^-/π differentiation;

- Four layers of straws, each 5 mm in diameter with 12 μm mylar walls coated with aluminium and a 20 μm tungsten wire coated with gold. The straws are arranged in an XXYY pattern and function as the tracking component of the STT. They are filled with a Xe/CO_2 gas mixture at an internal pressure of ~ 1.9 atm.

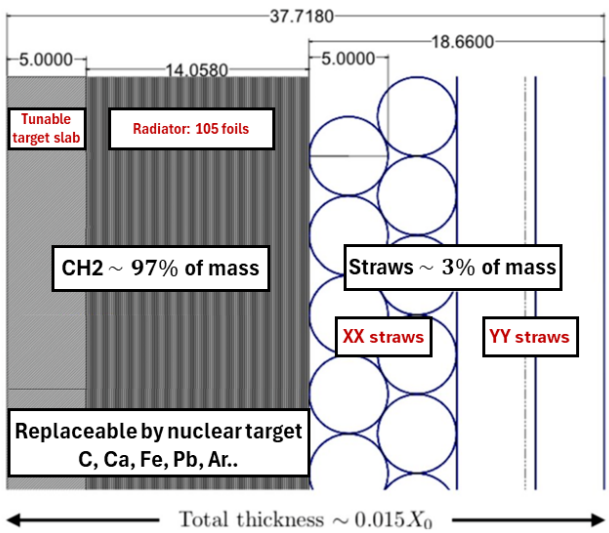

Figure 3.4: Section of one STT module showing three components from left to right: the tunable propylene target, the TR radiator with 150 foils of CH_2 (some of which can be dismounted to implement other nuclear targets) and the four straw tube layers in the XXYY arrangement.

The default configuration includes 8 carbon target modules, 70 CH_2 target modules, and 6 tracking modules positioned in both the upstream and downstream regions of the STT. This setup achieves an average density of 0.18 g/cm^3 ($\sim 1.3X_0$), with a total mass of 7.4 tons. Note that the density is kept low enough to ensure that the total detection length is comparable to the radiation length, allowing accurate measurements of the final state particle momenta. In this configuration, the STT foresees a spatial resolution of $\sigma_{x,y} < 200$

The Granular Argon for Interaction of Neutrinos (GRAIN) will be a small ~ 1 t LAr target situated in the upstream region of the SAND inner volume. It enhances ND-LAr TPCs data by providing on-axis measurements of nuclear effects from neutrino-argon interaction. In particular, it will allow to evaluate nuclear effects by measuring, together with the STT, neutrino interactions with argon, hydrogen, and carbon, all within the same detector apparatus. Its design is conceived to exploit the detection of the fast-emitted scintillation light from liquid Argon constraining the

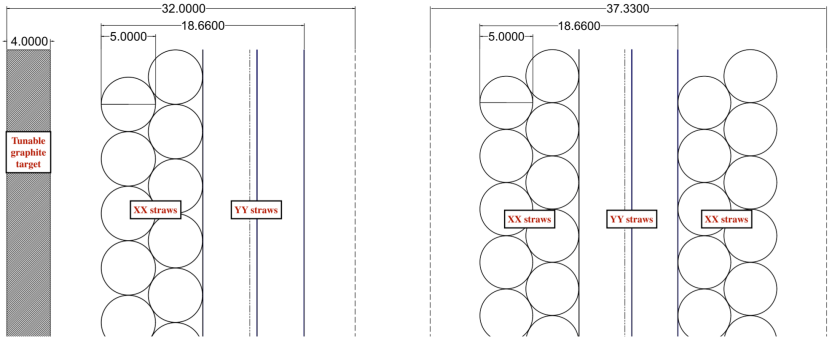

Figure 3.5: Left: Drawing of an STT module with a graphite (pure C) target. The thickness of the graphite plate is adjusted to provide the same fraction of X_0 as the CH_2 modules shown in Fig.3.4. The space created by the C-composite frame is also shown. Right: one STT tracking module without target and radiator, with only six layers of straw in a XXYYXX arrangement [28].

photon collection to a few nanoseconds and achieving high spatial resolution. The minimal volume of this detector ($\sim 1X_0$) aims to minimize the energy loss, particle showering and multiple scattering effects on the STT downstream components.

The detector features a dual-cryostat system consisting of an inner vessel and an outer vessel. The former is made of aluminum, measuring 147 cm in height, 150 cm in width, and a maximum depth of 47 cm. The latter is composed of layers of aluminum alloy, honeycomb, and carbon fiber, measuring 190 cm in height, 200 cm in width, and with a maximum thickness of 83 cm along the beam direction. This dimension are shown in Fig. 3.6. The light collection is done in the inner vessel, equipped with Vacuum UltraViolet (VUV) cameras operating at liquid argon temperatures (78 K).

The design considers two optical system options, one based on lenses and another on Coded Aperture Masks [31]. Lens-based cameras are well-known for their direct image reconstruction but pose construction challenges in cryogenic environments: conventional lenses exihibit low transmissvity to VUV light. Moreover due to LAr high refractive index, the focusing capability of standard lenses is reduced, resulting in a limited field of view and larger volumes. In contrast, mask-based cameras are simpler to build, offer a greater depth of field, and feature a more compact design.

Both optical systems are coupled to pixel-segmented photon detectors, each one consisting of a Silicon Photomultiplier (SiPM) matrix. The models currently available are the S14160 and S13615 Hamamatsu arrays, which come in 8×8 and 16×16 matrix configurations, respectively. These SiPMs face a significant limitation in their poor sensitivity to the 127 nm wavelength of argon scintillation light. To overcome this issue, a wavelength-shifter (WLS) is essential to convert UV light to visible light, where the SiPMs achieve their optimal photon detection efficiency.

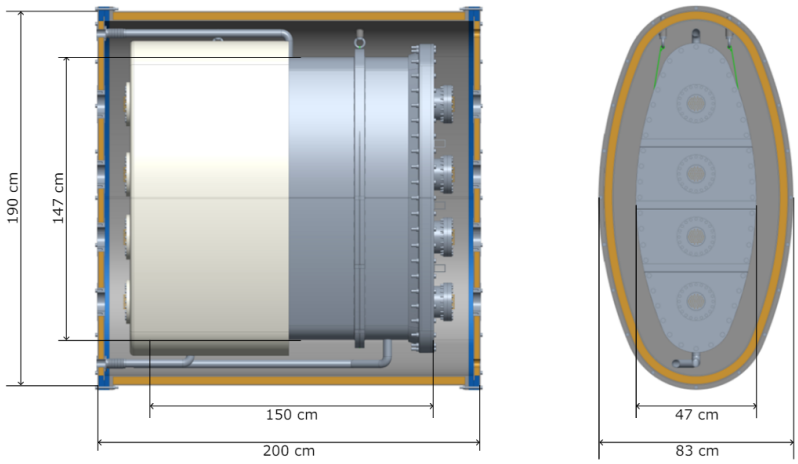

Figure 3.6: 3D model of GRAIN in lateral (left) and frontal (right) view with the inner and outer vessel dimensions. The target will be positioned almost in direct contact with the ECAL and occupies approximately the first upperstream ∼90 cm of the inner volume.[31]

3.2 Physics program

The SAND detector has to be able to monitor the beam on-axis, producing neutrino spectrum measurement in a relatively short time [27] to check the stability of the beam. Those measurements will be decisive to tune the beam model and control changes in the beam flux and spectra due to different reasons (e.g. target degradation).

SAND will constraints systematic uncertainties and neutrino/antineutrino flux analysis to improve the oscillation parameters measurements at FD. The design aims to support a wide-ranging physics program, which includes also fundamental studies on the nuclear effects in neutrino interactions with different targets.

DUNE will exploit the number of neutrino interactions for different flavours as a function of the reconstructed neutrino energy at both the Far and Near Detectors. The number of events in both sites can be expressed as the convolution of flux, cross-section and detector response function:

$$N^{ND}_{\nu_\alpha}(E_{rec}) = \int_{E_\nu} dE_\nu \Phi^{ND}(E_\nu)(E_\nu)\sigma^X(E_\nu)R_{phys}(E_\nu, E_{vis})R^{ND}_{det}(E_{vis}, E_{rec}) \quad (3.1)$$

$$N^{FD}_{\nu_\beta}(E_{rec}) = \int_{E_\nu} dE_\nu \Phi^{FD}(E_\nu)(E_\nu)P_{\nu_\alpha\to\nu_\beta}\sigma^{Ar}(E_\nu)R_{phys}(E_\nu, E_{vis})R^{FD}_{det}(E_{vis}, E_{rec}) \quad (3.2)$$

where:

$\Phi(E_\nu)$ is the incoming neutrino flux

σ_X is the neutrino cross section for X-process depending on the target nucleus which is Argon for the FD but is different in the ND environment.

$P_{\nu_\alpha \to \nu_\beta}$ is the probability of oscillation at FD that should be computed

E_ν is true neutrino energy

E_{rec} is the reconstructed neutrino energy

E_{vis} is the total energy in the visible final state

R_{phys} is the physics response function introduced by smearing of nuclear effects

R_{det} is the detector response function different for ND and FD

From the above equation, the oscillation probability cannot be determined just using the ratio of the number of events, even when considering the near-to-far neutrino flux ratio

$$\frac{N^{FD(E_{rec})}}{N^{ND}(E_{rec})} \neq R(E_\nu) P_{\nu_\alpha \to \nu_\beta}(E_\nu)$$

The main terms in Eq. 3.1 do not trivially cancel out between the Far and Near Detectors, making necessary to unfold them in order to perform neutrino oscillation analysis. This is not possible exploiting a single detector and single target material. While ArgonCube provides large statistical samples using technology similar to the FD, and TMS/ND-GAr can detect low-threshold particles despite its limited fiducial mass. However, using Argon as the sole nuclear target poses limitations for ND measurements. The Argon nucleus is not ideal for flux measurements due to significant nuclear effects that introduce modifications in the reconstructed spectra.

Additionally, since the relevant energy range for oscillation analyses is $0.5 < E_\nu < 10$ GeV, the interaction cross section include many contributions from all main processes such as $\sim 25\%$ quasi-elastic (QE), 42% resonances (RES), and 33% deep inelastic scattering (DIS). Current uncertainties on these processes are too large to cancel off in the ratio even using a ND complex as similar as possible to the FD.

To meet the DUNE analysis requirements is necessary to design a Near Detector capable of reducing the systematic uncertainties to a few percent over all the factors entering in Eq. 3.1.

3.2.1 Systematics uncertainties constrains

SAND will continuously monitor the on-axis $\nu/\overline{\nu}$ beam by reconstructing different complementary neutrino interactions. It will provide independent measurements of the interaction rate and energy spectra for the $\nu_\mu, \overline{\nu}_\mu, \nu_e, \overline{\nu}_e$ beam components exploiting several strategies for both relative and absolute fluxes:

$$\nu_\mu p \to \mu^- p \pi^+ \Rightarrow \text{relative } \nu_\mu \text{ flux vs. } E_\nu$$
$$\overline{\nu}_\mu p \to \mu^+ n(\text{QE}) \Rightarrow \text{relative } \overline{\nu}_\mu \text{ flux vs. } E_\nu$$
$$\nu e \to \nu e \text{elastic scattering} \Rightarrow \text{absolute } \nu_\mu \text{ flux}$$
$$\overline{\nu}_\mu p \to \mu^+ n \text{ (QE)} \Rightarrow \text{absolute } \overline{\nu}_\mu \text{ flux}$$

Referring to Eq. 3.1, even by measuring the flux, the three quantities σ_X, R_{phys}, R_{det} are still convoluted. SAND will be able to unfold and contrain such quatities thanks to the hydrocarbon in the target/tracker that provides neutrino interaction on different targets, C and H, in the same detector with a fixed R_{det}.

The hydrogen-enriched samples can be isolated using transverse kinematic imbalance (TKI) techniques. Given the expected high statistics for the ND (METTI REF), precise measurements of σ_X on H can be attained. Then, having hydrogen $R_{phys} = 1$, the determination of E_ν relies only on the detector response R_{det}, which is essentially determined by the momentum resolution $\delta p/p$.

On top of this, SAND will also provide constraints on the nuclear smearing (R_{phys}) on Argon thanks to the GRAIN detector. By performing measurements on Argon and on Hydrogen, one can constrain the product $\sigma_X \mathrm{R}_{phys}$ in argon, allowing thedetermination of nuclear smearing effects with the neutrino spectrum at the ND.

SAND results can then be compared with ND-LAr data, thus allowing to validate the unfolding of R_{det} in liquid Argon, and validating the predictions from the Near Detector before the extrapolation to the Far Detector.

3.2.2 Searches for New Physics

Physics Beyond the Standard Model (BSM) may emerge from unexpected deviations from the Standard Model (SM) predictions in the measurements conducted by the SAND detector. Such deviations would signify the presence of new BSM physics. SAND is designed to investigate potential BSM physics effects, such as examining the low-energy anomaly reported by the MiniBooNE [32] experiment. Oscillations involving sterile neutrinos might be identified by measuring neutrinos and antineutrinos CC ratios as a function of L/E, such as:

$$R_{e\mu}(L/E) = \frac{(\nu_e N \to e^- X)}{(\nu_\mu N \to \mu^- X)} \quad \text{and} \quad \bar{R}_{e\mu}(L/E) = \frac{(\bar{\nu}_e N \to e^+ X)}{(\bar{\nu}_\mu N \to \mu^+ X)}$$

as well as NC/CC ratios ($R_{\nu p}$) and ($R_{\bar{\nu} p}$) as functions of L/E, offering additional insights into the distinction between appearance and disappearance phenomena[28]. Moreover, SAND can further enhance the sensitivity of ND complex to probe Dark Sector physics,including searches for heavy sterile neutrinos, axion-like particles, and dark photons.

Chapter 4

An Extended Kalman Filter for SAND

The reconstruction of trajectories and interaction points is an essential step in the data analysis of particle physics experiments. Track fitting applies established statistical estimation procedures to determine the parameters of charged particle trajectories and their kinematic properties from a set of discrete measurements (hits). The primary methods for estimating track parameters are usually based on least-squares principles. The Kalman Filter (KF), introduced in 1960, is a recursive version of least-squares regression for track fitting, originally developed in high-energy physics by the DELPHI experiment, for estimating the state of a linear system under random disturbances [33].

The KF processes a set of discrete measurements to determine the state of a linear dynamical system. Operating through a prediction and an update phase, it combines predictions based on previous state estimates with subsequent measurements to minimize the impact of random perturbations or noise on the following state estimates. This method is particularly effective when the equation of motion is (quasi-)linear, there are numerous discrete measurement points, and the distance between these points is short enough to allow accurate state extrapolation, even in the presence of noise.

Although the KF has been largely used in many fields and showed optimal performances for most track reconstructions, its reliance on linear models for the system poses a significant limitation for many applications. This limitation has led to the development of various extensions, one of which is the Extended Kalman Filter (EKF). The EKF is designed to handle non-linear systems, such as the analysis of charged particles moving through magnetic fields.

In this chapter, the principles of the Extended Kalman Filter algorithm will be introduced. Its implementation for particles crossing the SAND detector will then be described, including the energy loss due to the passive target in the STT and the main sources of noise. Such implementation is later validated thorugh a series of

consistency tests both on ideal trajectories and simulated ones.

4.1 The Kalman Filter algorithm

The Kalman Filter consists of iterative steps in which the track state, and its associated covariance matrix, are updated as it progresses through a discrete dynamical system. At each step, it computes the best estimate of the state describing the system from the information collected at each previous measurements sites. Given a prior state vector a_{k-1}, or an initial estimate of the state (seed) if $k = 0$, the system equation describing the evolution of the state to the next site k is given by:

$$a_k^{k-1} = f_{k-1}(a_{k-1}) + w_{k-1}$$

where:

$\mathbf{a}_k$ is the track state vector at current step k

$\mathbf{w}_{k-1}$ is the *Process noise vector* is accounting for all sources of noise when propagating from site $k-1$ to k. It is assumed to be unbias.

$\mathbf{f}_{k-1}$ is the *State propagator*, non-linear function that represents the state vector propagation model from site k-1 to site k, which corresponds to a deterministic motion in the absence of noise ($w_{k-1} = 0$)

At each measurement site k, a set of observables values about the system are collected. These are represented by a m-dimensional colum vector named *measurement vector* (m_k). From the known state vector at a measurement site k, the measurement vector can be obtained as:

$$m_k = h_k(a_k) + \epsilon_k \tag{4.1}$$

where:

$\boldsymbol{h_k}$ *projector* is the measurement projection function from track state to measurement

$\boldsymbol{\epsilon_k}$ *measurement noise vector* is accounting for all sources of noise of the measurement vector. It is assumed to be unbias.

Note that for both w_k and ϵ_k a Gaussian distribution with zero means have been assumed, whose variances are respectively

$$Q_{k-1} = \langle w_{k-1} w_{k-1}^T \rangle \qquad V_k = \langle \epsilon_k \epsilon_k^T \rangle$$

As already said, the KF is a recursive algorithm that considers the single measurement locally, updating the best estimation of the state vector of the system through

a chi-squared minimization. The algorithm follows three main steps: prediction, filtering, and smoothing. Figure 4.1 shows a scheme of the KF algorithm, while the three step are described below.

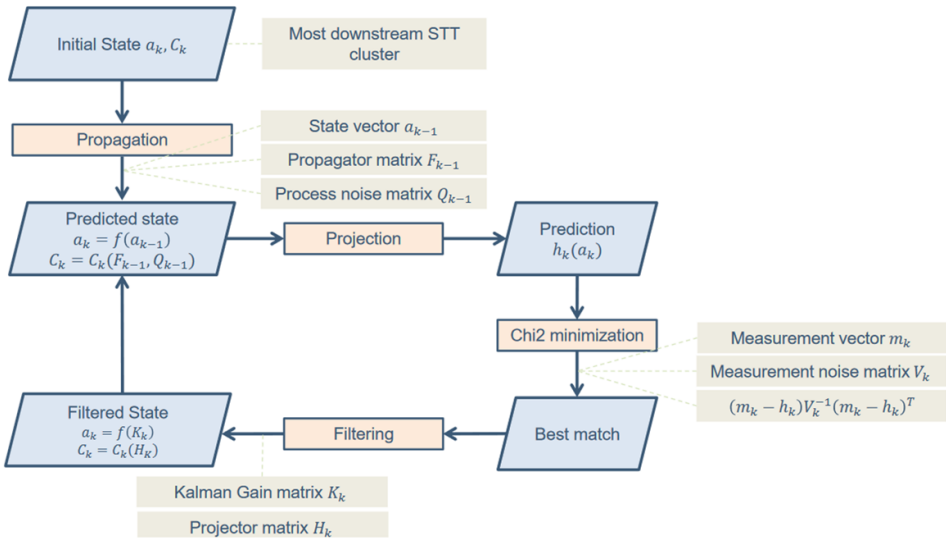

Figure 4.1: Flow chart of the KF algorithm.

Prediction

Given the observations made at sites up to $k-1$, the prediction of the state at the k-step, a_k^{k-1}, is obtained from the state vector a_{k-1} and its covariance matrix C_{k-1} as:

$$a_k^{k-1} = f_{k-1}(a_{k-1}) + w_{k-1} \tag{4.2}$$

$$C_k^{k-1} = F_{k-1} C_{k-1} F_{k-1}^T + Q_{k-1} \tag{4.3}$$

where the propagator matrix F_{k-1} is defined as first order derivatives of the state vector at site k with the respect to the state vector at previous step $k-1$:

$$F_{k-1} = \frac{\partial f_{k-1}}{\partial a_{k-1}} \qquad \text{Propagator matrix} \tag{4.4}$$

Filtering

At this stage, the algorithms updates the present k-th predicted state vector, a_k^{k-1}, based upon all present and past measurements. This is done estimating the track parameters using measurements up to and including m_k.

At the current stage, the only information about the state vector at k, from what was observed up to $k-1$, can be summarized with the following χ^2:

$$(\chi^2)_k^{k-1} = (\chi^2)_{k-1} + (a_k^* - a_k^{k-1})^T (C_k^{k-1})^{-1} (a_k^* - a_k^{k-1})$$

where a_k^* is the new estimation of the state vector at site k that should be optimized during the filtering, and χ^2_{k-1} is independent from it. It is now possible to add the information from the new measurement as:

$$(\chi^2)_k^k = (m_k - h_k(a_k^*))^T V_k^{-1} (m_k - h_k(a_k^*))$$

The increment to $(\chi^2)_{k-1}$ is then obtained as:

$$\begin{aligned}(\chi^2)_+ =& (a_k - a_k^{k-1})^T (C_k^{k-1})^{-1} (a_k - a_k^{k-1}) \\ &+ (m_k - h_k(a_k))^T V_k^{-1} (m_k - h_k(a_k))\end{aligned} \tag{4.5}$$

The best possible estimate of the state vector that can be obtained from all the measurements at the k-th site, is the one that minimizes the increment in Eq. 4.5. This can be found resolving the condition:

$$\frac{\partial \chi_+^2}{\partial a_k^*} = 0$$

from which one obtains:

$$a_k = a_k^{k-1} + K_k (m_k - h_k(a_k^{k-1})) \tag{4.6}$$

$$C_k = \left[(C_k^{k-1})^{-1} + H_k^T V_k^{-1} H_k \right]^{-1} \tag{4.7}$$

where a_k is called filtered state vector, C_k is its associated covariance matrix, and K_k is the *Kalman Gain* matrix defined as:

$$K_k = C_k^{k-1} H_k^T (V_k + H_k C_k^{k-1} H_k^T)^{-1}$$

that has been introduced to represent how much the new measurements at k improved the state vector at the same step.

Smoothing

Despite the filtered state vector obtained in the previous stage is already the optimal state at each site k, it can be reevaluated and improved after all the information over subsequent sites, from *k+1* up to n, has been collected. This process is called smoothing.

To perform the smoothing, a recurrence formula that operates in the reverse order

compared to the prediction and filtering stages nooed to be implemented. The smoothing process begins at the final site (k=n) and proceeds backwards to the first site (k=0). The best estimator for the state vector at site $k+1$, using the informations from all n-sites, is defined as the weighted mean of the predicted state vector, a^k_{k+1}, at site (k + 1) using measurements made at sites 1 to k and the filtered state vector, a^n_{k+1}, based on the measurements of the sites n to k + 1. It can be obtained minimizing the quantity:

$$\chi^2 = (a^n_{k+1} - a^k_{k+1})^T (C^k_{k+1})^{-1} (a^n_{k+1} - a^k_{k+1}) \tag{4.8}$$

$$+ (a^n_{k+1} - a^{n,k+1}_{k+1})^T (C^{n,k+1}_{k+1})^{-1} (a^n_{k+1} - a^{n,k+1}_{k+1}) \tag{4.9}$$

where C^k_{k+1} and C^n_{k+1} are the covariance matrices associated to the predicted and filtered state respectively. Being beyond the scope of this thesis to perform all the calculations[1], we will only write the final result of the smoothed state vector as follows:

$$a^n_k = a_k + A_k(a^n_{k+1} - a^k_{k+1})$$

$$C^n_k = C_k + A_k(C^n_{k+1} - C^k_{k+1})A^T_k$$

where A_k is defined as the the *Smoother Gain* matrix

$$A_k = C_k F^T_k (C^k_{k+1})^{-1}$$

4.2 KF implementation for SAND

It is now possible to describe the implementation of the KF algorithm to be used in the SAND detector. To do so, it is necessary to define a track model for a charged particle propagating through a magnetized volume, such as the SAND inner volume (Sec. 3). The model should take into account possible energy loss due to the presence of passive targets as well as the major sources of noise. One can then express the different components of the KF described in the previous section exploiting such model. The fitting process consists of determining the particle's path, described in a 6D phase space, by selecting specific surfaces in the detector as fixed locations to collect track hits. In the case of SAND, the Straw Tubes have been adopted as tracking modules arranged in layers. The fitting is performed by determining the particle's parameters at the positions where the track intersects these reference layers. At each location, the fit computes 5 parameters including position coordinates and momentum components assuming that one dimension can be derived, or costrained,

[1]The complete computation of both fitered and smoothing recurrence formula are available at [34]

from the others.

4.2.1 Trajectory model in a magnetic field

A particle with charge $q = \kappa \cdot |q|$ and mass m, moving into an homogeneous magnetic field $\mathbf{B}$, is subjected to a Lorentz force and follows an helicodal motion

$$\overrightarrow{F} = q \cdot \left(\overrightarrow{v} \times \overrightarrow{B}\right)$$

In SAND, the magnetic field is directed along the x-axis $\overrightarrow{b} = (1, 0, 0)$ and the above equation can be simplified as:

$$\overrightarrow{F} = q \cdot B \begin{pmatrix} 0 \\ v_z \\ -v_y \end{pmatrix} \tag{4.10}$$

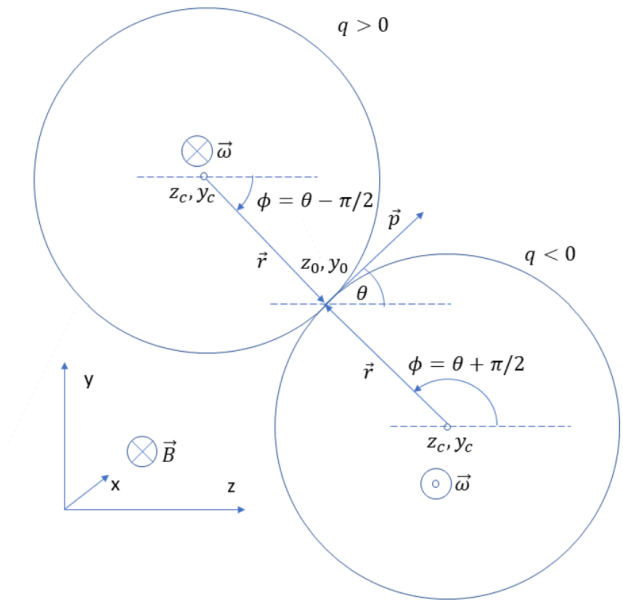

Figure 4.2: Sketch of the circulat motion on the bending y-z plane

The particle's motion can be thus decoupled in a constant velocity component along the x-axis, and a uniform circular motion in the y-z plane, which can be described using the polar angle

$$\theta = \arctan\left(p_x / |\overrightarrow{p_\perp}|\right) \tag{4.11}$$

where $\overrightarrow{p}$ is the particle momentum, p_x, p_y, p_z its components along the three axis,

and $\overrightarrow{p_\perp} = (0, p_y, p_z)$ is the transverse momentum. One can then obtains:

$$\overrightarrow{F} = q \cdot |\overrightarrow{v_\perp}| \cdot B \begin{pmatrix} 0 \\ \cos\theta \\ -\sin\theta \end{pmatrix} = -m \cdot \hat{r} \cdot \frac{|\overrightarrow{v_\perp}|^2}{R} \tag{4.12}$$

where $\overrightarrow{r} = R \cdot \hat{r}$ is the position of the particle with the respect of the center of the circle. If the particle's position is $\overrightarrow{x} = (x, y, z)$, the center coordinates of the circle can be written in terms of the azimuthal angle of the pivot with respect to the center itself, $\phi = \theta - \kappa \cdot \pi/2$ (Fig. 4.2), as:

$$\begin{aligned} y_c &= y - R\sin\phi \\ z_c &= z - R\cos\phi \end{aligned}$$

and thus the equations of motions became:

$$\begin{aligned} x &= x_o + v_x \cdot (t - t_o) \\ y &= y_c + R \cdot \sin(\omega(t - t_0) + \phi_0) = y_0 + R \cdot (\sin\phi - \sin\phi_0) \\ z &= z_c + R \cdot \cos(\omega(t - t_0) + \phi_0) = z_0 + R \cdot (\cos\phi - \cos\phi_0) \end{aligned} \tag{4.13}$$

where:

$\overrightarrow{x_0} = (x_0, y_0, z_0)$ is the initial position taken arbitrarly to coincide with the measurement point at site $k = 0$.

$\mathbf{t}_0$ is the initial time.

$\omega = -(\vec{\omega})_x = \kappa \cdot \frac{|\overrightarrow{v_\perp}|}{R}$ is the angular velocity.

$\phi_0 = \arctan(y_0 - y_c)/(z_0 - z_c)$ is the initial rotation angle respect to the pivotal point, $\vec{x_0}$

From the ϕ_0 deifinition, we derive also the relation between the rotation angle and the radius of the helix as:

$$\phi = \pm \arccos\left(\cos\phi_0 + \frac{(z - z_0)}{R}\right) \tag{4.14}$$

with the condition $(\phi - \phi_0) \cdot \omega > 0$ for propagation forward in time and $(\phi - \phi_0) \cdot \omega < 0$ for propagation backward in time. This ensures that the model will return only the solution that corresponds to the next hit in the correct time direction.
Finally, using the definition of dip angle (rotation of the helix w.r.t y-z plane),

$\lambda = \arctan(p_x/|\vec{p_\perp}|)$, it is possible to derive:

$$
\begin{aligned}
t &= t_0 + \frac{(\phi - \phi_0)}{\omega} = t_0 + \tilde{R} \cdot \frac{(\phi - \phi_0)}{|\vec{v}| \cdot \cos\lambda} \\
x &= x_0 + \tilde{R} \cdot \tan\lambda \cdot (\phi - \phi_0) \\
y &= y_0 + R \cdot (\sin\phi - \sin\phi_0) \\
z &= z_0 + R \cdot (\cos\phi - \cos\phi_0)
\end{aligned}
$$

where $\tilde{R} = \kappa \cdot R$ is the signed radius of the helix.

It is now possible to define a convenient parametrization of the state vector, which result convenient in fixed target experiments, for a track propagating through a magnetized detector:

$$
a_k = \begin{pmatrix} x \\ y \\ 1/\tilde{R} \\ \tan\lambda \\ \phi \end{pmatrix} \tag{4.15}
$$

where ϕ is used as running parameter instead of z to solve the problem of tracks looping back due to the magnetic field.

4.2.2 Energy loss

Interaction of incident particle with the target and radiator materials of the STT induces energy losses that cause a reduction of the helix curvature. This effect must be included in the implementation of the KF algorithm to be able to correctly predict the vector state from one step to the following one. The energy loss between two steps can be defined as:

$$
\Delta E = \frac{dE}{dx}\Delta l \tag{4.16}
$$

where the amount of crossed material:

$$
\Delta l = \Delta s \cdot \frac{v}{|v_z|} = \frac{\Delta s}{|\cos\lambda| \cdot \sin\phi}
$$

and Δs defined as the thickness of the passive material (target plus the radiator). The dE/dx is computed from the standard Bethe-Bloch formula, in which the properties of the detector materials are included as extracted from SAND geometry file (Sec. 5.1.2)

In the KF, the fraction of energy lost ΔE is accounted for by updating the quantity $1/R$ at every step by the quantity:

$$
\Delta(1/R) = \frac{d(1/R)}{dE}\Delta E
$$

$$-\langle\frac{dE}{dx}\rangle = \underbrace{4\pi N_a m_e r_e^2 c^2}_{\text{Constant terms}} \cdot \underbrace{\rho\frac{Z}{A}}_{\text{Medium properties}} \cdot \underbrace{\frac{z^2}{\beta^2}\left(\frac{1}{2}\ln\frac{2m_e c^2\beta^2\gamma^2 T_{max}}{I^2} - \beta^2\right.}_{\text{Beam properties}} \underbrace{\left. - \frac{\delta}{2} - \frac{c}{z}\right)}_{\text{Density and C-shell corrections}}$$

It us useful to rewrite this in terms of the state vector parameters that entrers in the system propagation. Using the energy-momentum relation $p = \sqrt{E^2 - m^2}$,and the relation between the transverse momentum and inverse radius attainable from Eq. 4.12

$$R = \frac{|\overrightarrow{p_\perp}|}{|q| \cdot B} \tag{4.17}$$

from which the standard conversion to compute the particle momentum obstained as

$$p_\perp(\text{GeV/c}) = 0.3B(\text{T}) \cdot R(\text{m}) \tag{4.18}$$

Considering also that $p_\perp = p/\cos\lambda$, one obtains:

$$\begin{aligned}
\Delta(1/R) =& \frac{\partial(1/R)}{\partial E}\frac{\partial p}{\partial E}\Delta E \\
=& -0.3 \cdot B \cdot \cos\lambda \cdot \frac{E}{(E^2 - m^2)^{3/2}} \\
=& -0.3 \cdot B \cdot \cos\lambda \cdot \frac{\sqrt{p^2 + m^2}}{p^3} \\
=& -0.3 \cdot B \cdot \cos\lambda \cdot \left(\frac{(1/R)}{0.3 \cdot B \cdot \cos\lambda}\right)^3 \cdot \sqrt{\left(\frac{0.3 \cdot B \cdot \cos\lambda}{(1/R)}\right)^2 + m^2} \\
=& -\frac{(1/R)^2}{0.3 \cdot B \cdot \cos\lambda} \cdot \sqrt{1 + \frac{m^2(1/R)^2}{(0.3 \cdot B\cos\lambda)^2}} \\
=& -\frac{(1/R)^2}{0.3 \cdot B} \cdot \sqrt{1 + \tan^2\lambda} \cdot \sqrt{1 + \frac{m^2(1/R)^2}{(0.3 \cdot B)^2}(1 + \tan^2\lambda)}
\end{aligned}$$

4.2.3 System Equation

Given the track model for a charged particle in an homogeneous magnetic field in a fixed target experiment, and the contribution of the energy loss between different steps, it is now possible to implement the Extended Kalman Filter algorithm in SAND and derive the system equation $a_k = f_{k-1}(a_{k-1}) + w_{k-1}$

Propagator f_{k-1}

To predict the state vector a_k along the helical trajectory we determine the propagator function $f_{k-1}(a_{k-1})$ according to the helix transformation from site $k-1$ to k in the system equation:

$$\begin{aligned} x_k &= x_{k-1} + \tilde{R}_{k-1} \cdot \tan\lambda_{k-1} \cdot (\phi_k - \phi_{k-1}) \\ y_k &= y_{k-1} + R_{k-1} \cdot (\sin\phi_k - \sin\phi_{k-1}) \\ 1/\tilde{R}_k &= \tilde{R}_{k-1} + \kappa \cdot \Delta(1/R_{k-1}) \\ \tan\lambda_k &= \tan\lambda_{k-1} \end{aligned} \tag{4.19}$$

Considering that the measurements will be perfomed in planes of fixed z, the corresponding ϕ angle can be obtained from:

$$\cos\phi_k = \cos\phi_{k-1} + \frac{(z_k - z_{k-1})}{R_{k-1}}$$

Propagator matrix F_{k-1}

The propagator matrix defined in Eq. 4.4 is calculated by differentiating Eq. 4.19 with respect to a_{k-1}. This involves calculating various partial derivatives for each state vector parameter, which we will not detail in this text, but can be found in [35].

Process noise matrix Q_{k-1}

If the state vector parameters evolution is unaffected by stochastic noise, the process noise covariance matrix Q_{k-1} is exactly diagonal, as the term w_{k-1} is absent in Eq. 4.2. However, when introducing stochastic processes such as MCS, ionization losses, and bremsstrahlung (which is not treated in our case), the system equation becomes non-deterministic and process noise must be included. This vector represents the fluctuation of each parameter along the particle's path, resulting in off-diagonal elements in its covariance matrix Q_{k-1}. While the energy loss due to ionization has already been accounted for, MCS must also be considered for completeness as it affects the prediction of the state vector between two subsequent steps. At each step the scattering angle, θ_{MS}, is computed as [36]:

$$\sigma_{MS} = \frac{13.6MeV}{\beta pc} z \sqrt{\frac{\Delta l}{X_0}} \left[1 + 0.038 \ln\left(\frac{\Delta l}{X_0}\right)\right]$$

where β is the particle velocity and X_0 is the radiation lenght of the material expressed in cm

The variance of the process noise depends on the materials the particle travels through between two measurement sites (k-1 and k). To simplify the model, we assume

that the distance between these two sites is small enough. Instead of considering the continuous distribution of materials along the path, we approximate all scattering effects as occurring in a single, infinitely thin layer. The elements of the process noise covariance matrix Q_{k-1}, relative to ϕ and $\tan\lambda$, are evaluated through error propagation and can be expressed as:

$$\begin{aligned}\langle w_i w_j \rangle =& \sigma_{MS}^2 \left(\frac{\partial w_i}{\partial \theta_{k-1}} \frac{_j}{\partial \theta_{k-1}} + \frac{\partial w_i}{\partial \lambda_{k-1}} \frac{_j}{\partial \lambda_{k-1}} \right) \\ =& \sigma_{MS}^2 \left(\frac{\partial w_i}{\partial \theta_{k-1}} \frac{\partial w_j}{\partial \theta_{k-1}} + (1+\tan^2\lambda_{k-1})^2 \frac{\partial w_i}{\partial \tan\lambda_{k-1}} \frac{\partial w_j}{\partial \tan\lambda_{k-1}} \right)\end{aligned}$$

4.2.4 Measurement prediction

Lastly, it is possible to derive the formulae related to the measurement equation $m_k = h_k(a_k) + \epsilon_k$. As mentioned, the locations of the charged particle are sampled at discrete points along its trajectory, referred to as measurement layers. For each layer, the spatial coordinate and the angle of the trajectory are collected, forming the measurement vector m_k. Since in the STT the planes can be oriented either horizontally or vertically, the angles at which the track hits the layer at site k are defined as:

$$\theta_{xz} = -\kappa \cdot \arctan \frac{\tan\lambda}{\sin\phi} \qquad \theta_{yz} = \phi + \kappa \cdot \frac{\pi}{2}$$

and the correspoding measurement vectors are respectively:

$$m_k = \begin{pmatrix} x \\ \theta_{xz} \end{pmatrix} \qquad m_k = \begin{pmatrix} y \\ \theta_{yz} \end{pmatrix}$$

Projector h_k

As defined in Eq. 4.1, the projector provides the measurement vector at site k as a function of the state vector parameters. With the track model implemented as describe in Eq. 4.19], the projectors are defined, depending on the orientation of the STT layers, as:

$$h_k^x = \begin{pmatrix} x_k \\ -\kappa \cdot \arctan \frac{tan\lambda}{\sin\phi} \end{pmatrix} \qquad h_k^y = \begin{pmatrix} y_k \\ \phi_k + \kappa \cdot \frac{\pi}{2} \end{pmatrix} \tag{4.20}$$

Projector Matrix $\mathbf{H}_k$

The derivatives of the projector h_k are included through the following matrix which is in general dependent again on the orientation of the measurement layers:

$$H_k^x = \begin{pmatrix} 1 & 0 & 0 & 0 & 0 \\ 0 & 0 & 0 & \frac{\kappa}{\sin\phi_k \cdot \left[1+(\frac{\tan\lambda_k}{\sin\phi_k})^2\right]} & -\frac{\tan\lambda_k}{\tan\phi_k} \cdot \frac{\kappa}{\sin\phi_k \cdot \left[1+(\frac{\tan\lambda_k}{\sin\phi_k})^2\right]} \end{pmatrix}$$

$$H_k^y = \begin{pmatrix} 0 & 1 & 0 & 0 & 0 \\ 0 & 0 & 0 & 0 & 1 \end{pmatrix}$$

Measurement noise matrix V_k

It accounts for the resolution of detector at the measurement site. If two coordinates are measured on the intersection layer at step k and these coordinates are statistically independent, the covariance matrix can be expressed as:

$$V_k = \begin{pmatrix} \sigma_x^2 & 0 \\ 0 & \sigma_\theta^2 \end{pmatrix}$$

where $\sigma_x = 200$ μm and $\sigma_\theta = 0.2$ mrad are the position and angular resolutions expected for the STT. More in general, we can take V_k as a constant matrix in the track fitting.

4.3 Test and Validation

To test the implemented KF algorithm, a series of consistency checks focusing exclusively on the algorithm's performance, without delving into detailed physical studies, were performed. The initial phase involved a preliminary test simulating circular trajectories of varying momentum in a homogeneous magnetic field. This stage was essential to isolate and validate the algorithm performances on propagation. Subsequently, the energy loss was introduced, to verify its correct implementation within the algorithm. This step was crucial for assessing how well the EKF handles the complexities of experimental scenarios where the passive target materials are introduced. Finally, the same analysis were performed on simulated muon trajectoriesincluding includin both the energy los and MCS effects.

4.3.1 Standard consistency checks

To verify whether or not the KF is performing correctly, it is usefull to introduce a metric, called *innovation* vector, defined as the residual between the predicted measurement and the true one for each KF step:

$$\mathbf{r}_k = \text{predicted}_k - \text{true}_k$$

The innovation is instrumental in updating the state estimate, as shown in Eq. 4.6, and can thus be used to verify the reliability of the filtering process. If the prediction and propagation stage of the algorithm are correctly implemented, the innvoation should have zero mean and covariance matrix given by Eq. 4.7. The consistency of the filter is then verified following two procedures:

1. verify that the innovation is consistent with its covariance by checking if the

magnitude falls within $\pm\sqrt{C_{ii}}$ range. If the filter is working properly a standard normal distribution is expected for:

$$g_k^i = \frac{r_k^i}{\sqrt{C_k^i}} \tag{4.21}$$

where

r_k^i is the discrepancy between prediction and true measurement for the i-th matrix element, at the k-th step

$\mathbf{C}_k^i$ is the covariance matrix diagonal element for the same element and step

2. verify the unbiasedness of the innovation using a χ^2 hypothesis testing. The normalized innovations squared, defined as:

$$q_k = \mathbf{r}_k^T C_k^{-1} \mathbf{r}_k \tag{4.22}$$

was computed for a sequence of N trials of the Kalman filter. If the filter assumptions are met, then q follows a chi-squared distribution with 2 degrees of freedom corresponding to the rank of the innovation.

4.3.2 Lossless trajectory model

For the first test, energy losses and multiple Coulomb scattering effects were intentionally excluded. Both procedures described in the previous section were applied to a samples of charged particles propagating in a magnetic field. The trajectory of each particle was computed analytically step-by-step along the z-axis, with a step size of 50 mm. For each step, the position and direction of the trajectory were used to define the measurement vector. A smearing of 200 micrometers on the position and of 200 milliradians on the direction was applied to simulate the STT expected resolution. The Kalman Filter was then applied to each trajectory and both checks described above were performed. The result of the KF application on one trajectory is reported in Fig. 4.3, where the positions of the trajectory on both the xz and yz planes are shown for all the stages of the algorithm. The corresponding results of the consistency checks are reported in Fig.4.4 where g-distribution is computed for both elements of the measurements vector while Fig.4.4 shows the distribution of q.

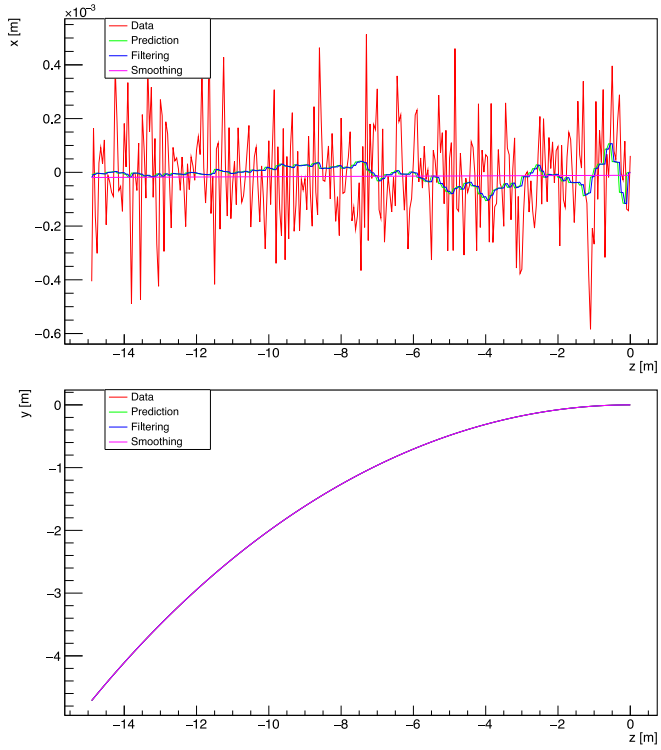

Figure 4.3: Reconstruction of circular trajectories using the EKF algorithm for ideal case excluding any energy losses contribution. Top: xz plane where the smearing applied on measurements is visible. Bottom: the same trajectory in the y-z bending plane assess the correct implementation of the system equations.

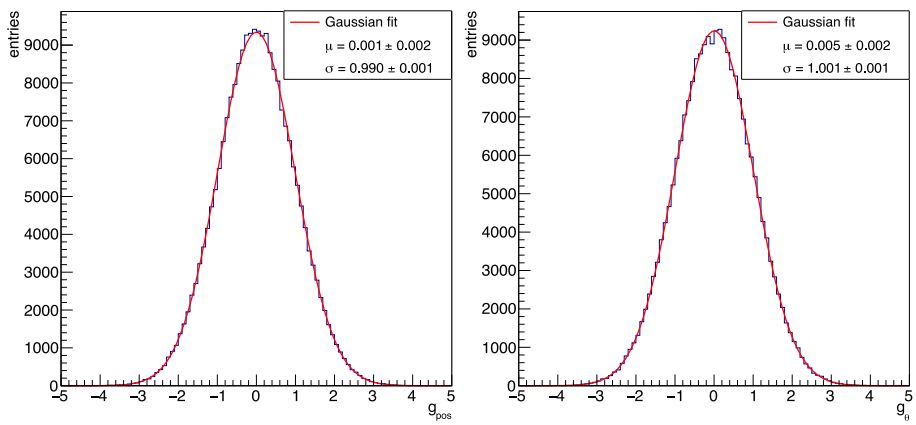

Figure 4.4: Distributions of the g quantity for both position and angular measurements

4.3.3 Energy loss and Multiple Coulomb Scattering

To validate the algorithm in a more realistic detector environment, is necessary to verify the correct implementation of the energy loss in the passive target of the STT modules, introduced in Sec. 4.2.2. At each step k, the energy loss between

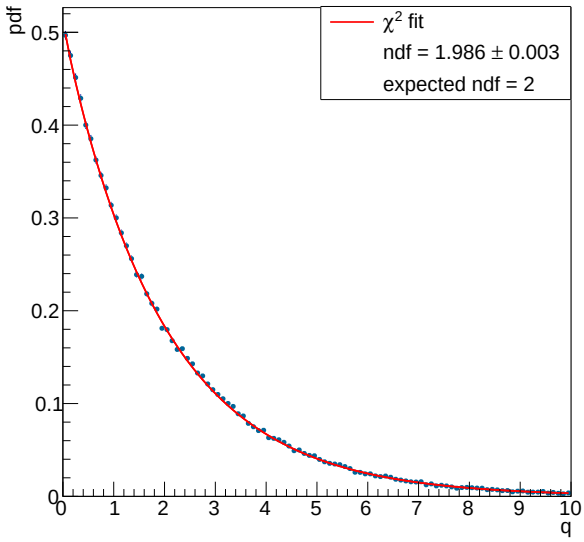

Figure 4.5: χ^2 hypothesis test for ideal charged particle trajectories with no energy losses to verify the validity of the filtering stage implementation. The obtained number of degrees of freedom is equal to the rank of the innovation confirming the correct implementation of the covariance noise matrix assumptions.

points k and $k{+}1$, is computed using dE/dx estimates from the Bethe-Bloch formula multiplied by the crossed material, ΔZ:

$$E_k^{reco} = \frac{dE}{dx} \times \Delta Z \left[\mathrm{g} \cdot \mathrm{cm}^{-2}\right] \tag{4.23}$$

where the particle trajectory between two subsequent sites was approximated as a straight line as depicted in Fig. 4.6.The ΔE_k^{true} is instead obtained as the difference between the MC energy of the particle at the step k and the one at the step $k{+}1$. A complete physics simulation (as described in the following Chapter 5) was performed in order to compare the computed energy deposition ΔE_k^{reco} with the expected

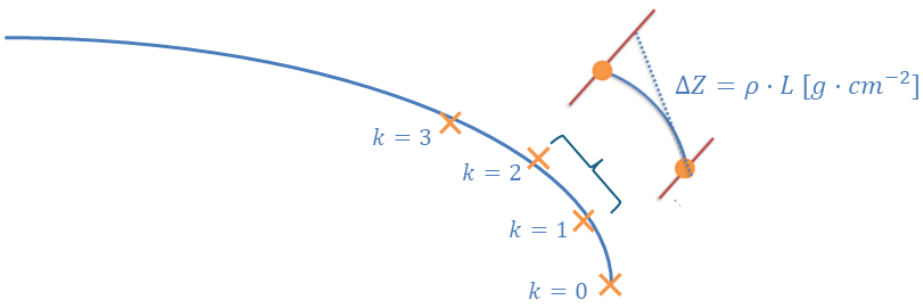

Figure 4.6: Sketch of the linear approximation used in the computation of the energy loss between two measurements layer.

$Delta_k^{true}$ from Monte Carlo (MC), at the same step. Left panel of Fig. 4.7 shows the compared distribution of ΔE^{reco} and ΔE^{true}. Despite some discrepancies the two distributions present similar features to describe the energy loss in different materials present in the STT. In the right panel instead the the distribution of $(\Delta E^{reco} - \Delta E^{true})/\Delta E^{true}$. It is visible how the highest bins are the two closest to zero, with a half-width-half-maximum of 0.15, suggesting a correct implementation of the $(\Delta E^{reco}$ computation. The observed discrepancies can be addressed to more than one factor: the emission of secondary particles, which are included by the MC generator but not in Eq. 4.23 and the linear approximation for ΔZ described above, that could not be optimal for lager value of energy loss.

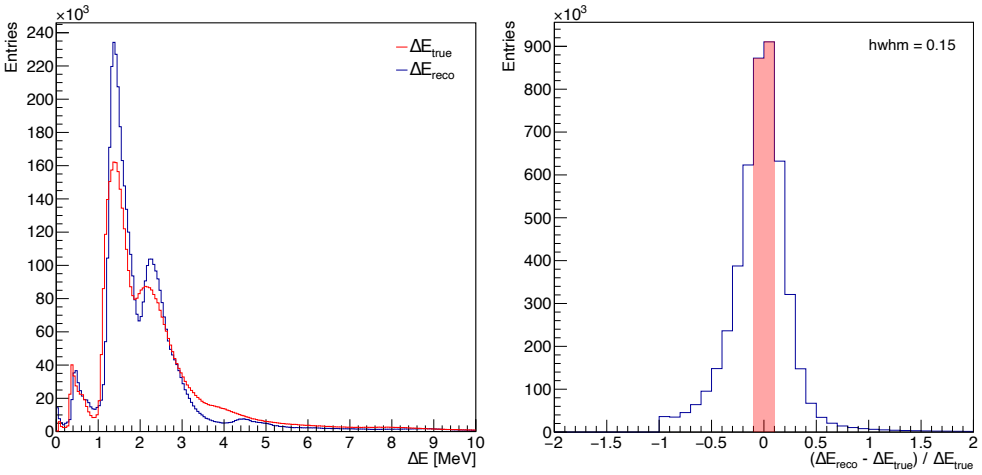

Figure 4.7: Left: distribution of the energy loss for each step of the simulated trajectories obtained from the MC-truth (red) and computed as described in Eq. 4.23 (blue); peaks correspond to different materials. Right: residuals distribution of the computed energy loss.

4.3.4 Complete trajectory model

After validating the energy loss, it is now possible to verify the consistency of the EKF implementation on realistic charged particles crossing the SAND STT volume including both energy los and Multiple Coulomb Scattering effects. A sample of muons was generated with a full physics simulation detailed later in Sec. 5.1. Validation procedure as described in Sec. 4.3 is perfomed to the simulated trajectories. An example of a reconstructed muon trajectory is shown in Fig. 4.8, while the same distributions shows in the ideal case are displayed in Fig. 4.9 and Fig. 4.10 for g distribution and the chi-squared test respectively.

Despite the introduction of stochastic noise due to energy losses during trajectory propagation, the algorithm is performing well. The smoothed state obtained with the KF is converging to the true trajectory state and the predicted measurement vector aligns with the observed one and its covariance matrix.

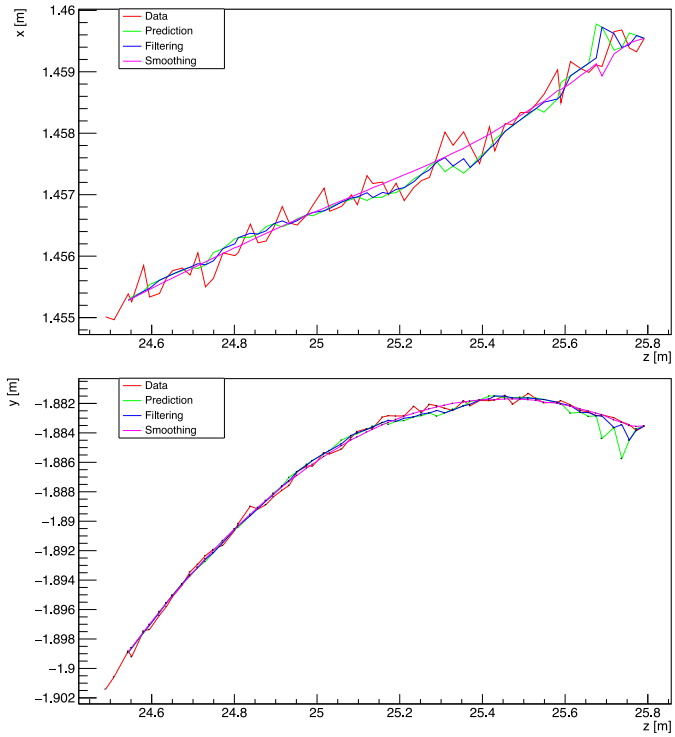

Figure 4.8: Reconstruction of a simulated muon trajectory using the EKF algorithm, including the energy losses contribution. Top: xz plane, where the smearing applied to the measurements is visible. Bottom: the same trajectory in the yz bending plane assess the correct implementation of the system equations.

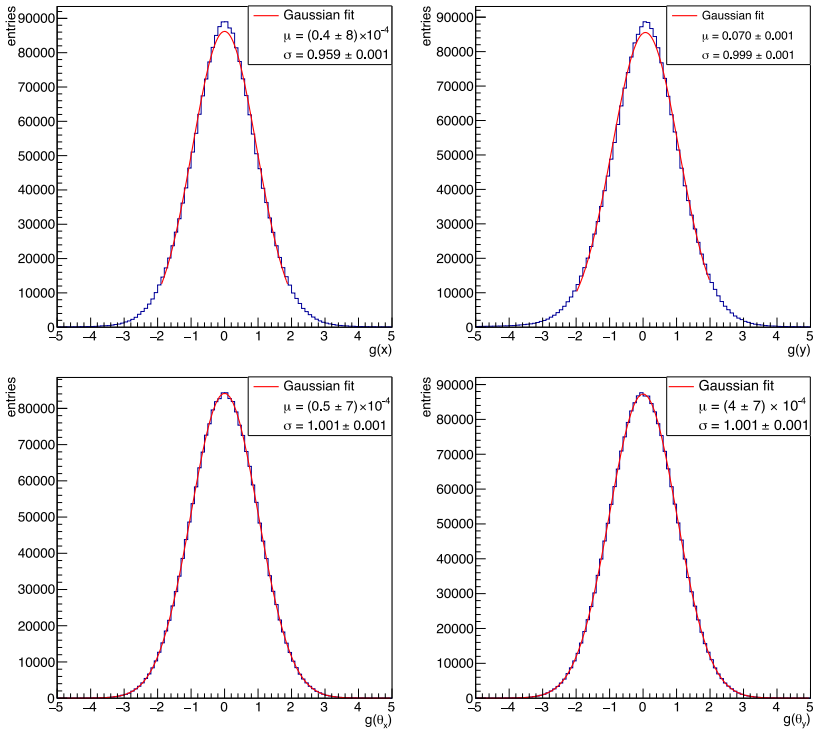

Figure 4.9: Distributions of the g quantity for both position (top row) and angular (bottom) measurements.

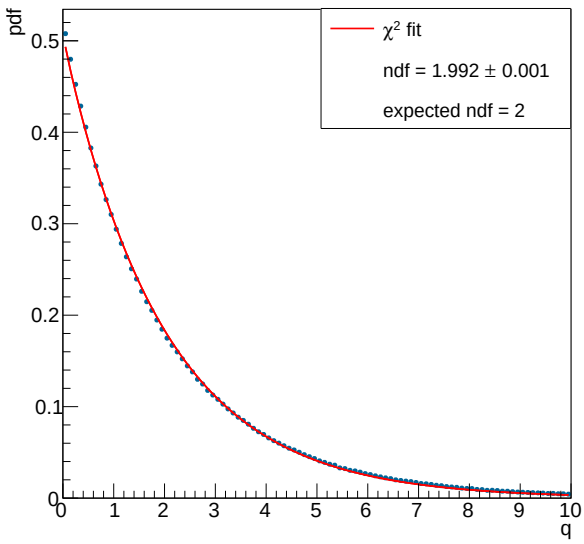

Figure 4.10: χ^2 hypothesis test for simulated muons trajectories including energy losses to verify the validity of the filtering stage implementation.

Chapter 5

Reconstruction of ν_μ CC events in the target/tracker

Following the promising results reported in the previous chapter, a full simulation of the SAND detector has been used to study the performances of the algorithm in reconstructing ν_μ CC events.

5.1 Simulation Framework

A full simulation has been performed, consisting of various steps, from the neutrino interaction to the signal digitization, as outlined in Fig 5.1. The neutrino flux, geometry generator, and interaction generation packages are common to the whole Near Detector. The signal digitization and the reconstruction of the signals produced in the STT was instead developed separately in the C++ SAND framework. This allowed to leverage object-oriented features and accommodate different measurement layer designs and coordinate systems with minimal user-coding. The software includes generic abstract base classes that implement Kalman filter-based track fitting without being tied to a particular track model or geometry. This approach ensured a robust and flexible framework for algorithm validation under controlled conditions.

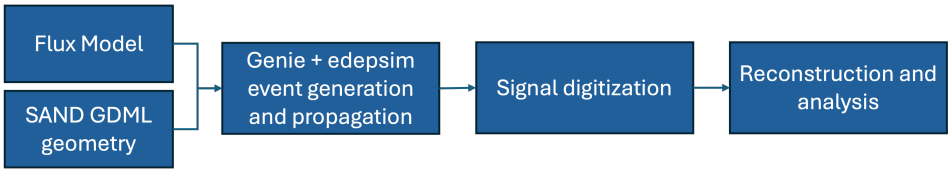

Figure 5.1: Complete simulation flow chart including: flux simulation operated by GEANT4, SAND geometry included in XML files generated by *gegede* application.These two are given as input for generating neutrino events with GENIE. Primary particles are propagated into detector geometry, using edep-sim software to simulate energy deposition.

5.1.1 Flux spectrum

The neutrino flux at the Near Detector is predicted using a Geant4-based simulation of the incident proton beam, the target, the focusing horns, the decay pipe, and the hadron absorber. All the simulated neutrino interactions used in the following analysis were generated with neutrino fluxes as expected at the LBNF (3). These are calculated at 574 m from the start of the horns and include fluxes for muon and electron neutrinos and antineutrinos[REF]. The unoscillated calculated flux for muon neutrinos used in the generation of neutrino interactions in SAND is shown in Fig. 5.2.

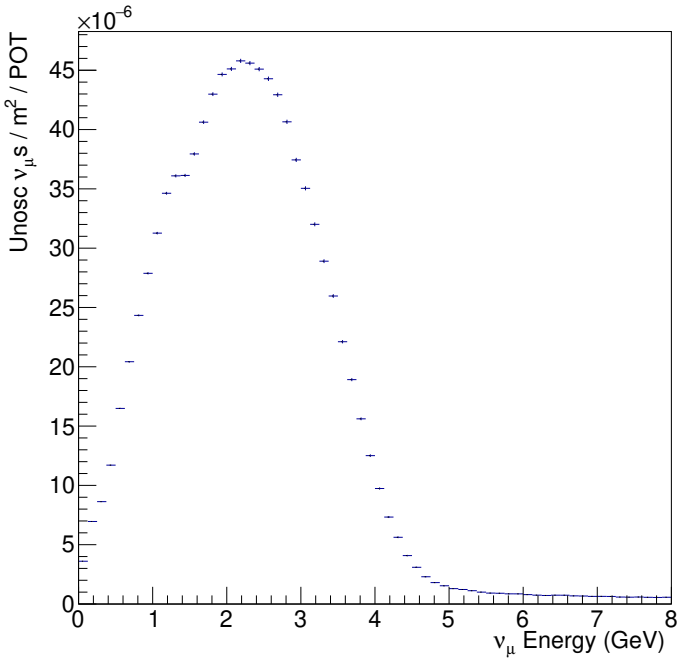

Figure 5.2: Generated ν_μ flux used as input for the neutrino event generation in GENIE

5.1.2 Geometry

The SAND geometry is described by XML files generated by a python based application called General Geometry Description (GeGeDe) REF, recommended by the DUNE collaboration. GeGeDe transforms user geometrical inputs into the GDML format, an XML-based format that expresses all necessary properties for simulating particle interactions.

The used geometry includes all the detector components as described iN 3, with the z axis going along the beam direction, while the y and x axis go upward and sideways respectively. Despite the geometry includes all the SAND components, the following results will be presented by looking only at the STT component. A detailed

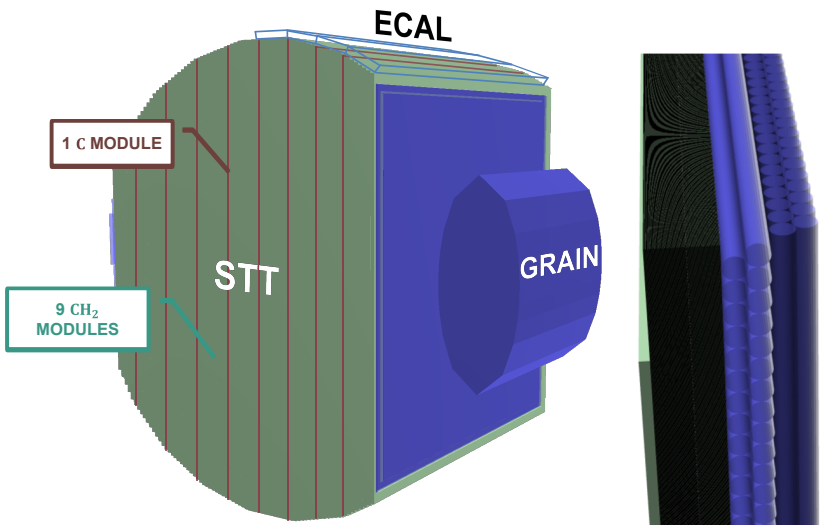

Figure 5.3: Views of the geometry of the STT as implemented in the simulation. Left: Straw Tube Tracker geometry showing the alternating sequence of C and CH_2 modules, in red ad green respectively. The first and last five modules are tracking modules (blue). Right: A detail of one standard CH_2 STT module is shown on the right.

description of its implementation is thus here provided:

STT geometry

In accordance with the specifications outlined in Sec. 3.1.3, the Straw Tube Tracker has been simulated. It consists of 84 modules, arranged in a sequence where one carbon (C) module alternates with every nine polyethylene (CH_2) modules. Each unit is composed of a slab of target material (either C or CH2), a radiator constructed from 105 C3H6 foils, each 18 thick, interleaved with layers of air, and four planes of straw tubes. The first and last five STT units act as tracking modules, equipped solely with straw tube planes without target and radiator slabs. The width of each module is consistently set at 4 meters, while the height varies according to the z-axis position. Fig. 5.1.2 displays the complete geometry of the STT, along with a detailed view of an individual module. 5.1.2

5.1.3 Neutrino event generation and particle propagation

Flux and detector geometry serve as inputs for neutrino event generation. The simulation of neutrino interactions with the multiple nuclei targets present in SAND's inner tracking volume was performed with the GENIE event generator. GENIE is a ROOT-based [37] neutrino interaction generator widely used in the neutrino community, especially for low-energy (<1 TeV) interactions.

One important aspect of the GENIE generator is the possibility to specify both a detector geometry and a neutrino flux. For this simulation, the geometry and flux

just described were used. The software than uses these information, together with pre-compiled cross-section libraries, to determine the neutrino energy and interaction type. The prduced output contains detailed information regarding the simulated neutrino processes and the particles in the final state. Particles exiting the struck nucleus are then propagated through the detector using a Geant4 wrapper called edep-sim[38].

Edep-sim produces ROOT trees containing simulated energy deposition information and associated truth labels. The tree includes TG4Event object, which contains data on primary particles, including event and run identifiers. It also holds details on particles trajecotries, such track identifier, PDG codes,initial momentum and sequence of points formed along the path. For SAND, the edep-sim output is utilized to simulate the response of the STT and ECAL and to perform digitization according to their readout specifications. Specifically, GENIE files are read in the "rootracker" format, which is a standard for GENIE event ROOT trees. Edep-sim can also generate and propagate beams of particles using Geant4 command macros, a feature that has been employed in this thesis. A display of a simulated ν_μ events in SAND is shown in Fig. REF for both the XY- and YZ-view.

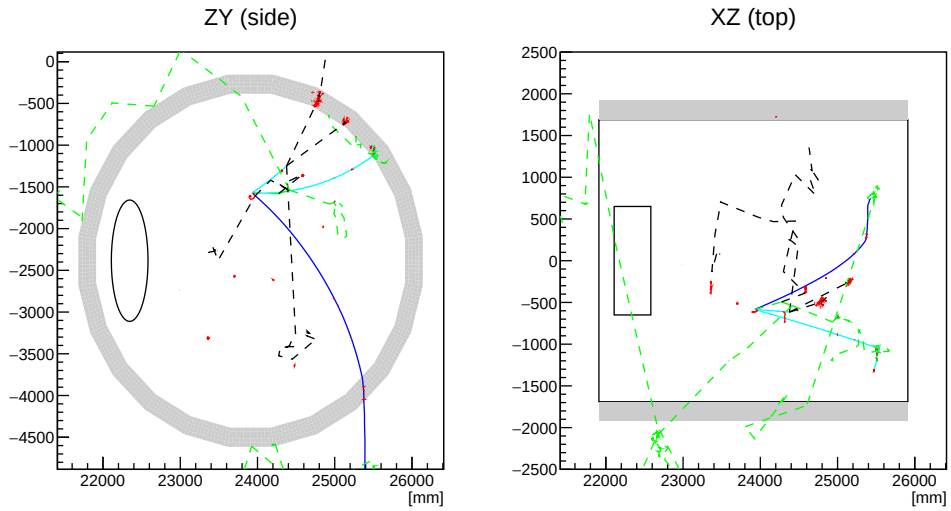

Figure 5.4: Display of a simulated ν_μ event in SAND. Muons are represented in blue, pions in cyan, gammas in black, electrons in red and neutrons in green.

5.1.4 Digitization

From the simulated MC trajectory data, one needs to produce a set of measurements resembling the ones the detector would produce by simulating the detector response and digitization of the signals. For the STT case, the measurement is a 2D vector composed by a spatial coordinate and a direction, as defined in Eq.4.1. In the following, instead of the complete digitization expected for the STT, a simplified version will be used.

Each particle trajectory is sampled at discrete spatial intervals of 5 cm along the z-axis, starting from the interaction point, by selecting the appropriate trajectory points among the ones produced by edep-sim. At this step, no pattern recognition is performed. Each particle is associated with its trajectory points exploiting the MC-truth.

From the selected trajectory points, the measurement is obtained as the x and y coordinates of the point, while the angles on the horizontal and vertical planes, θ_{xz} and θ_{yz}, are computed as the mean of the slopes between the selected point and the previous and following ones. To introduce realistic detector effects and resolution limitations of SAND, a smearing of $\sigma_{x,y} = 200\mu$m and $\sigma_\theta = 0.2$mrad is applied to the positions and angles respectively. Figure 5.5 illustrates the initial steps and logical flow from reading the detector geometry to reconstructing the initial state. For this implementation, it was assumed that measurements alternate between

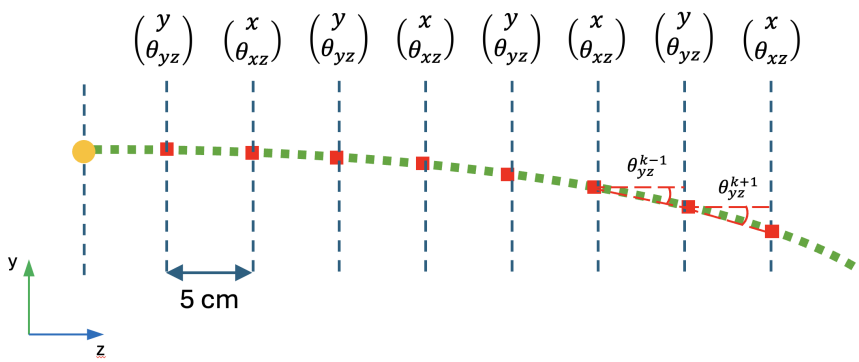

Figure 5.5: Sketch of the digitization procedure. In yellow is represented the the interaction vertex, in green the simulated Trajectory Points, while in red the selected ones at each measurement layer (dotted lines).

vertical and horizontal-like STT planes. Note that this is a simplification used for algorithm validation and does not reflect the actual STT pattern in SAND. Future improvements will involve digitization that includes the real STT arrangement and the implementation of a clustering algorithm.

After digitization, we arbitrarily choose the initial state vector at $k = 0$ as the most downstream point of the MC-generated track points. This point serves as the initial seed for the reconstruction algorithms, which will then proceed with propagation according to the model elaborated in Section 4.2.

5.2 Trajectory reconstruction

One of the goals of the SAND detector is to use multiple nuclei targets to provide high-statistic sample of neutrino-hydrogen interactions that can be used for nuclear model extraction (Sec. 3.2). The simulations and reconstruction of charged current neutrino interactions can be used as preliminary studies to assess the feasibility of

Particle	Events
μ^-	619924
π^+	284747
p	308280

Table 5.1: Number of reconstructed particles for each type in a sample of $\nu \sim 10^6$ events using the aforementioned criteria.

SAND and optimize its design.

After validating the EKF implementation in Chapter 4, its performances were esitimated by appliying it to single particles produced in ν-CC interactions, using the available information from the STT. A sample of $10^6 \nu_m u$ CC interactions in the STT volume was simulated, following the pipeline depicted in Section 5.1. For each simulated interaction, all the primary particles exiting the vertex were selected, exploiting the MC-truth, if three selection criterions were satisfied:

a) the particle should be either a muon, pion or proton

b) the trajectory should have a minimum of 10 measurements

c) and the starting point (corresponding to the vertex position) should be inside a fiducial volume defined as a cilinder of radius 1.85 m from the center of the STT on the vertical plane, and of 3.1 m of lenght along the x-axis i.e. $\sqrt{y^2 + z^2} < 1.85$ m.

The simulation produced about 10^6 ν_μ events among which the selection efficiency for each particles tupe is listed in Table 5.1

The KF algorithm was then applied to the selected trajectories and its performances were evaluated looking at the reconstructed state vector parameters.

5.2.1 Position and angle reconstruction

Measurement vector parameters were taken as the ones of the reconstructed state associated to the most upstream measurement of each trajectory, for which the MC values where also available from the simulation. The x and y coordinate, as well as $\tan\lambda$ and ϕ obtained from the reconstruction, where thus compared with the corresponding MC values. The resolution of each quantities was then computed separately for each of the selected particle types (muon, pions. protons). Fig. 5.6 shows the distribution of each reconstructed quantity of the state vector as a function of the corresponding true one for the reconstructed muons, while the right side show the distribution of the residuals of each paramenter. Similar plots for pions and protons are reported in A. A summary of all the obtained results is lsited in Table 5.2.

Reconstructed quantities result well predicted with unbiased mean ($< 10^-4$). The RMS for all parameters is $< 5 \times 10^{-3}$ excluding $\tan\lambda$, for which the RMS is

instead about 3%. Considering the projectors expression in eq. 4.20 is reasonable to expect larger RMS values for parameters related to the horizontal planes (x and tanλ), hence the uncertainty on angular resolution enters as the propagated error on lambda, affecting differently the errors on different planes.

	x	y	$\tan\lambda$	ϕ
$\mu-$	$-4e-06 \pm 0.0019$	$-4.6e-06 \pm 0.00012$	0.0009 ± 0.029	-0.0008 ± 0.0021
π^+	$7e-07 \pm 0.0026$	$5.1e-06 \pm 0.00024$	0.0037 ± 0.039	-0.0005 ± 0.0035
p	-$3e-06 \pm 0.0023$	$1.30e-05 \pm 0.0002$	0.0022 ± 0.043	-0.0010 ± 0.0036

Table 5.2: Reconstructed positions and directions for all the selected particles. The results are expressed as $\mu\pm$ RMS.

5.2.2 Momentum reconstruction

Once the 3D trajectory is reconstructed, the particle momentum can be estimated from the track curvature. Recalling eq. 4.18 the relation obtained is:

$$P_{reco} = P_\perp \cdot \sqrt{1+\tan^2(\lambda)} = 0.3 \cdot B \cdot R_{reco} \cdot \sqrt{1+\tan^2(\lambda)} \tag{5.1}$$

For each event and primary particle selected the comparison between the true MC momentum P_{true} and the reconstructed P_{reco}, as well as the relative residuals, are shown in Fig. 5.7. It is visible how the results present similar features for all the selected particles, the most notable being a large number of low momentum particles with overestimated reconstructed energies. Further investigation of these results was done by looking at the resolution of the momentum reconstruction as a function of the dip angle distribution (Fig. 5.8). As seen in Fig. 5.6 the reconstruction of the dip angle worsens for larger angles, usually corresponding to lower momentum, and affects the value of the reconstructed momentum (Eq.5.1). Figure. 5.9 shows the momentum reconstruction efficiency after selecting all the trajectories with $\tan\lambda < \pm 1$ where the overestimated is greatly reduced by this cut.

A large number of events with overestimated momentum is still clearly visible for all the particles. Despite this tail, the final distribution of the residual for both muons and pions has a mean value <0.004, with an RMS of 4.8% for the muons and 6.3% for the pions. The reconstructed momentum distribution of the protons is instead largely affected by the tail and presents a bias of about 3% with an RMS of 8%. The results for all the particles are summarized in Table 5.3.

Selecting all the trajectories with $\tan\lambda < \pm 1$, the overestimated tail is greatly reduced, as shown in Figure REF.

	All trajectories	$abs(\tan\lambda) < 1$
μ^-	0.005 ± 0.053	-0.002 ± 0.048
π^+	$5e-4 \pm 1e-4$	-0.004 ± 0.063
p	0.038 ± 0.085	0.034 ± 0.079

Table 5.3: Proton reconstruction resolution for all the selected particles before and after the cut over large values of the dip angle λ

5.3 Vertex reconstruction

Vertex finding is a critical process in particle physics, involving the identification of clusters of particle tracks that originate from the same spatial point. A straightforward tool that searches for tracks that can be geometrically combined to form a vertex was thus developed. The underlying principle is based only on geometric considerations, rather than more complex methods.

For each simulated event, the procedure begins by considering all reconstructed tracks by the kalman filter algorithm. These tracks are linked into 2-prong vertices if they meet two criteria:

1. The impact parameter—the perpendicular distance from the track to the vertex point—is less than 5 cm.

2. The longitudinal distance—the distance along the beam axis—between the upstream position of the track and the point of closest approach is less than 10 cm.

Following this, any 2-prong vertices that can be clustered within a 5 cm radius are merged into a single vertex. This merged vertex is roughly estimated as the mean value of the coordinates of the individual vertices involved.

The final step involves optimizing the position of the vertex. This is achieved by minimizing the sum of the impact parameters of the tracks associated with the vertex. The vertex position is adjusted within a 5 cm range, in steps of 1 mm (Fig. 5.10). This iterative process refines the vertex location to provide a more accurate reconstruction of the interaction point. It's important to note that this method does not account for the momenta of the tracks, nor does it consider the errors in track parameters estimated by the Kalman filter. Therefore, this approach is an initial attempt to estimate the accuracy of interaction point reconstructed by using the SAND Target Tracker and the kalman filter track reconstruction. Due to the track selection efficiency reported in Table 5.1, combined with the efficiency of the vertexing procedure itself, about 367000 vertices were reconstructed. The results for the those vertices are visible in Fig. 5.11 and 5.12, where the difference between the true and reconstructed x, y, and z coordinates of the vertex are shown. From Figure 5.11 it is visible how the results for the x and y coordinates have similar results: a mean value

$< 10^{-6}$ mm and a RMS of about 3 mm for the x coordinate, whle the y coordinate has a mean value $< 10^{-4}$ mm and a RMS of about 2 mm, The FWHM of both distributions was also computed and was found to be 600 μm for both distributions. Figure 5.12 shows instead the residual of the z coordinate, for which a bias of about 2 mm was found, with a RMS of 5 mm and a FWHM of 3 mm. As written in Chap3, one of the main goal of SAND is to detect neutrino interactions of both Argon, Carbon and Hydrogen targets to disentangle and constrain the main parameters involved in the neutrino oscillation analysis (Sec. 3.2). To do so, the vertex position should be reconstructed with high precision, to correctly identify the target, and thus the material, where the interaction occurs. This makes the reconstruction of the z coordinate crucial. As the width of a target is 5 mm (Sec.3.1.3), the resolution of the reconstructed z coordinate should have a resolution smaller than such value. The results described above, and summarized in Table 5.4, show how the current KF and vertexing algorithms satisfy this requirement, as the FWHM of the residual distribution is 3 mm.

	x	y	z
Mean	$(4 \pm 5) \times 10^{-6}$	$(1.3 \pm 0.1) \times 10^{-4}$	-0.0017 ± 0.00001
RMS	0.0027 ± 0.0001	0.0019 ± 0.0001	0.0049 ± 0.0001
FWHM	0.0006 ± 0.0004	0.0006 ± 0.0004	0.0030 ± 0.0004

Table 5.4: Resolutions of the vertex reconstruction for all the spatial coordinates.

5.4 Future Prospects

The algorithm that has been developed is suitable for the baseline STT requirements but in its current state, it relies on MC-truth for seeding and PID. Introducing a reliable seeding algorithm to improve the initial state vector selection procedure is necessary to allow its use with real data. Furthermore, refining the handling of multiple scattering contributions for different particles is necessary to achieve higher energy resolution. Enhancing the modeling of scattering effects in momentum reconstruction will reduce uncertainties and improve accuracy, especially for protons. Another potential improvement is the development of a realistic STT digitization and clustering. Currently, GRAIN reconstruction is conducted separately from the STT and from ECAL. Each subdetector has its reconstruction algorithm running independently, and a global fit has not yet been developed. Tracks in the STT are fitted without consideration for matching clusters in the ECAL and GRAIN. All these additions are required to develop a comprehensive reconstruction software for neutrino events within the SAND framework.

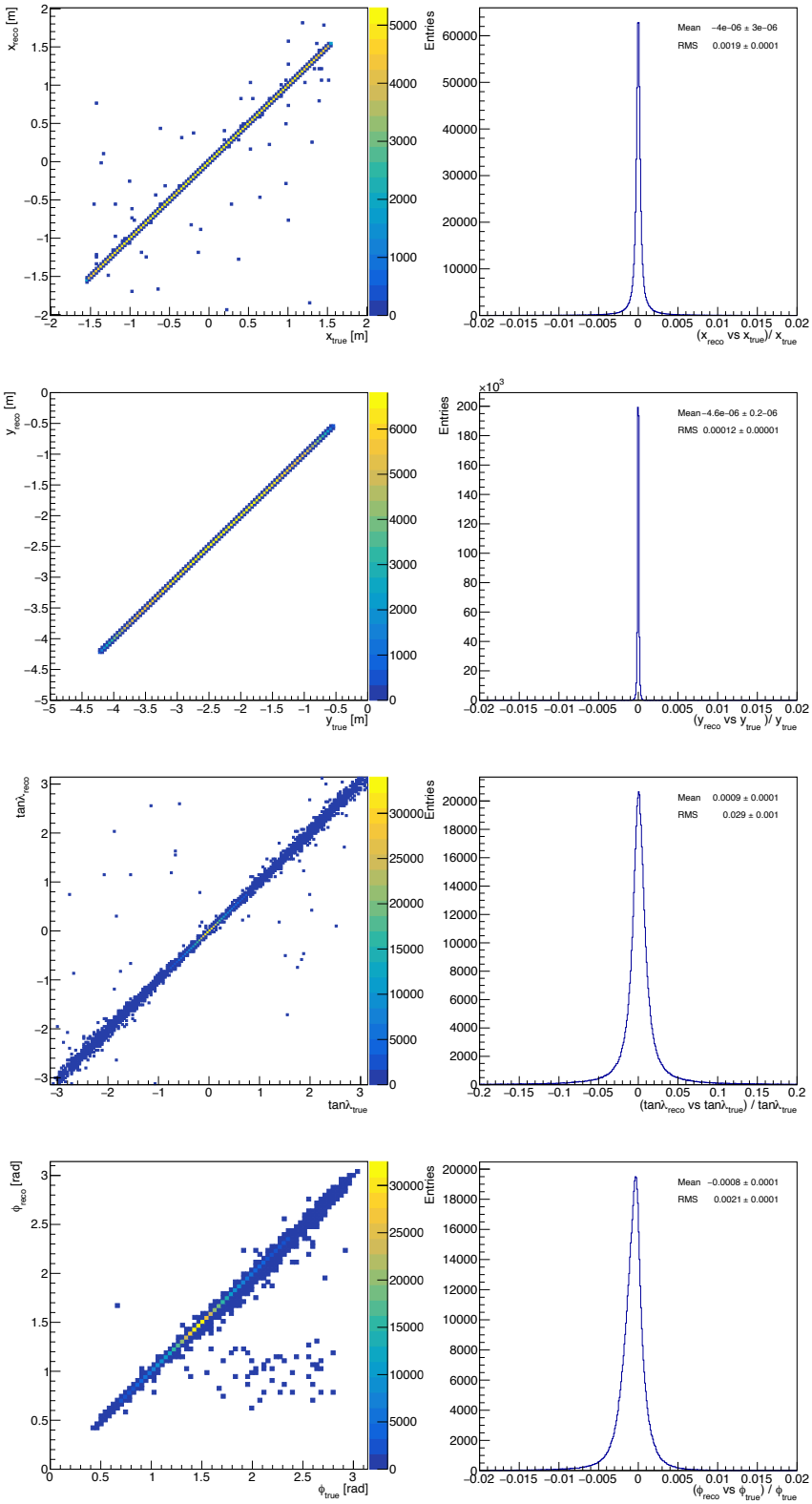

Figure 5.6: From top to bottom: x, y, $\tan\lambda$, and ϕ reconstructed quantities for the selected muons. Left: reconstructed quantities as a function of the true ones. Right: relative residuals of each reconstructed quantity.

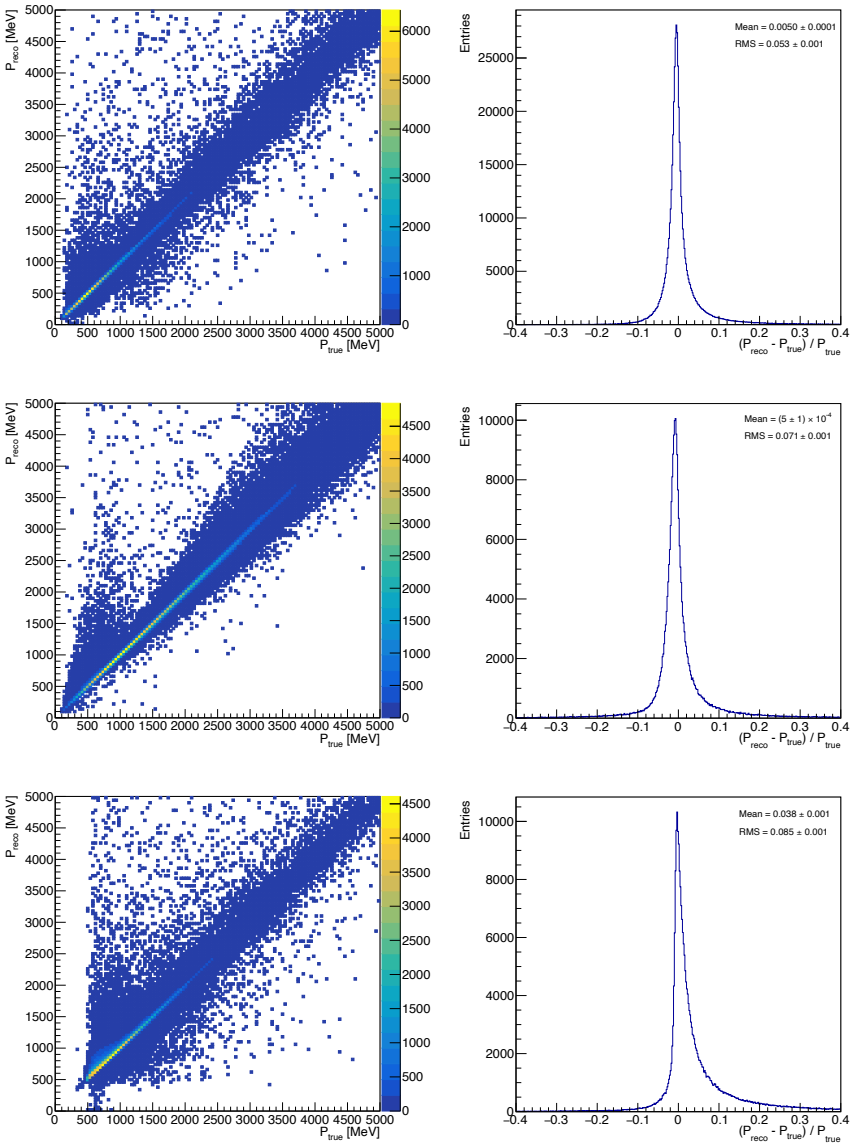

Figure 5.7: Primaries particle momentum reconstruction in the fiducial STT volume for all the selected muons (top), pions (middle), protons (bottom). Left: reconstructed momentum as a function of the true one. Right: relative residuals distribution.

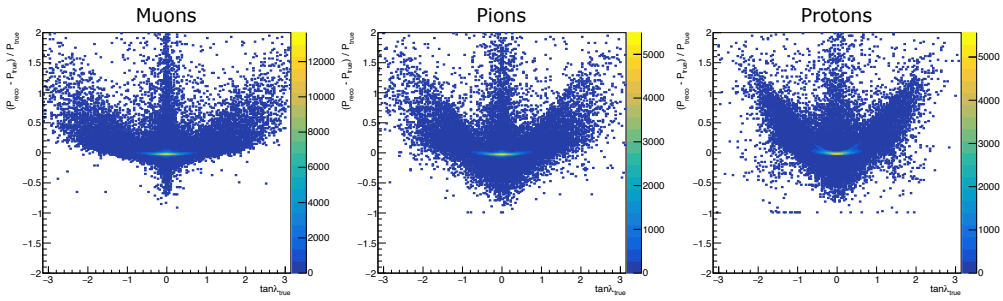

Figure 5.8: Momentum residuals as a function of the true value of the dip angle $\tan\lambda$ for muons (8)left), pions (middle) and protons (right).

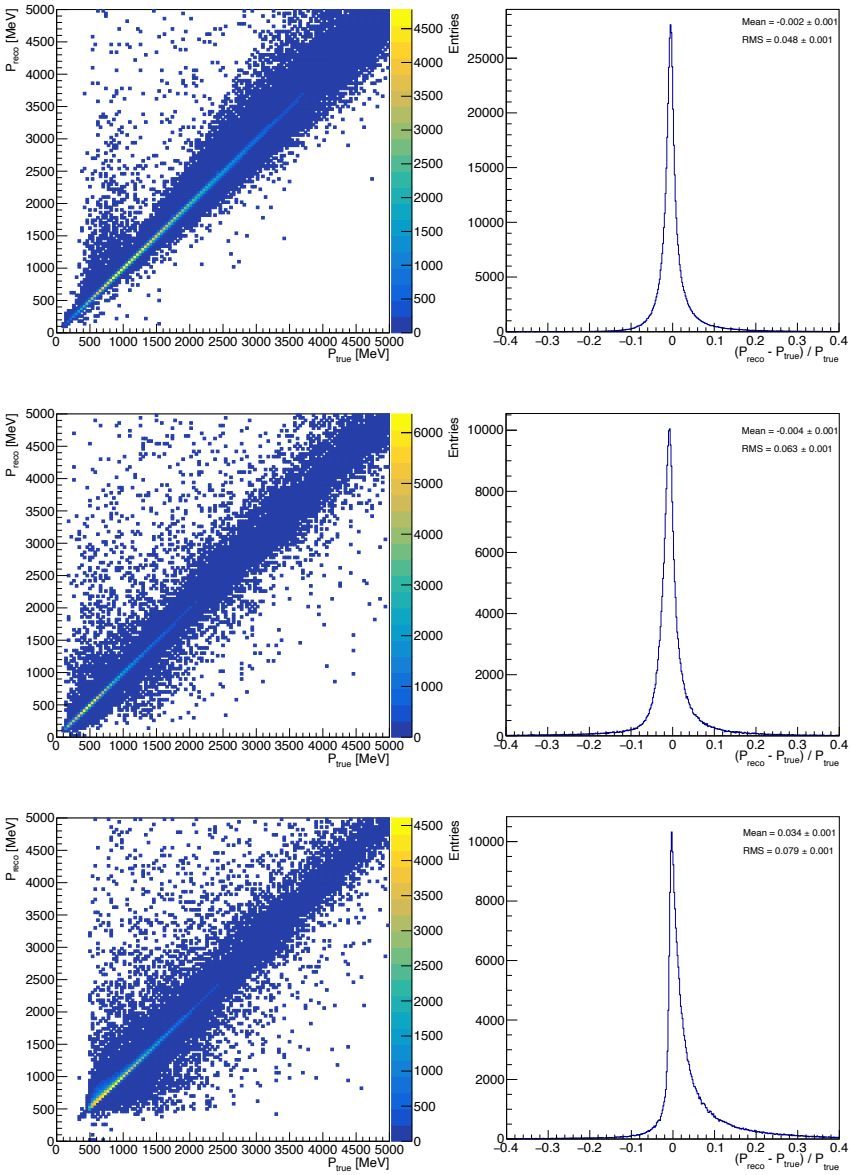

Figure 5.9: Primaries particle momentum reconstruction in the fiducial STT volume for muons (top), pions (middle), and protons (bottom) with $|\tan\lambda| < 1$. Left: reconstructed momentum as a function of the true one. Right: relative residuals distribution.

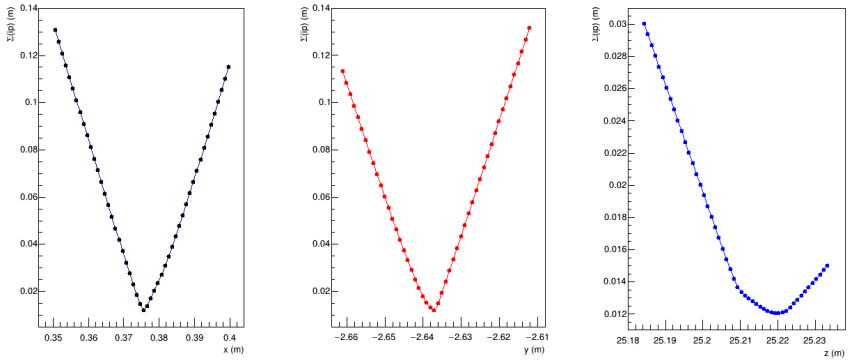

Figure 5.10: Example of vertex optimization for 5-prong vertex. 1D projections x (left), y (middle), z (right) of the iterative minimization.

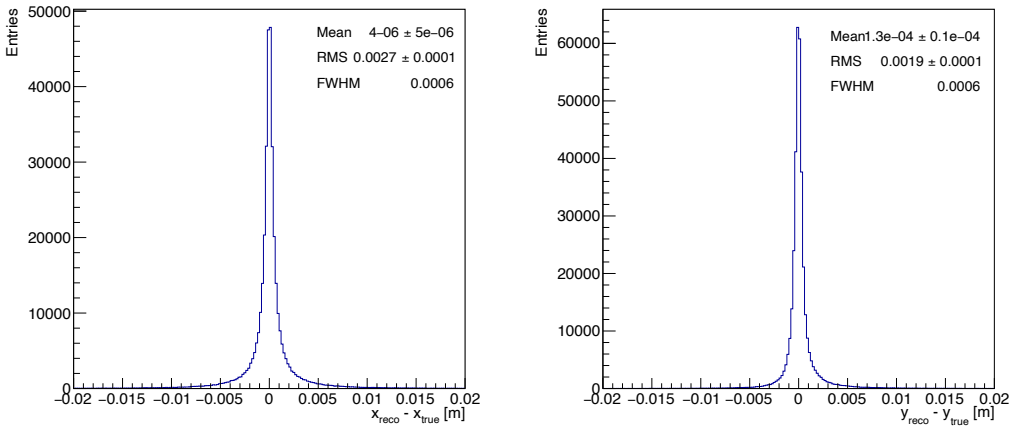

Figure 5.11: Vertex reconstruction of x and y coordinates for the event selected as in Sec. 5.2

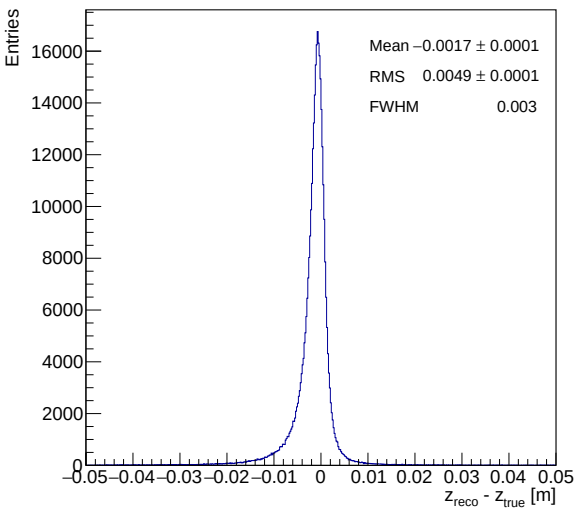

Figure 5.12: residual of the vertex z coordinate

Conclusions

Since their discovery in 1998, neutrino oscillations have been extensively studied through various experiments involving solar, atmospheric, accelerator, and reactor neutrinos. These studies have measured several key parameters, but open questions remain, such as the determination of neutrino mass ordering and CP violation in the leptonic sector. The Deep Underground Neutrino Experiment (DUNE) is a next-generation long-baseline neutrino experiment designed to address these questions.

DUNE will feature a Far Detector with four LAr TPCs and a Near Detector complex comprising three different detectors: ND-LAr and TMS, which are movable off-axis, and SAND, fixed along the beam axis, designed to perform measurements that constrain systematic uncertainties in neutrino oscillation analysis at the FD. The DUNE oscillation analysis cannot heavily depend on Monte Carlo (MC) simulations or model corrections to control systematics, given its ambitious goals and expected sensitivity. A robust analysis with minimal model dependence is particularly critical for searches for New Physics.

SAND is a multipurpose detector that exploits different materials as (anti)neutrino passive target, alternating with high-resolution tracker modules based on straw tubes (STT). The light target/tracker is complemented by a small liquid argon volume (GRAIN) and it is surrounded by an electromagnetic calorimeter, within a magnetized volume. The tracker design allows for unique measurements using solid hydrogen. The internal tracking system, together with GRAIN, enables the collection of neutrino interactions on various nuclear targets including argon (Ar), polyethylene (CH2), and carbon (C). This extensive data will help improve neutrino-nuclei interaction models, reduce smearing from nuclear effects on reconstructed energy, and support a broader independent physics program.

In this context, my thesis focuses on developing a track reconstruction algorithm for SAND, leveraging the Extended Kalman Filter technique, suitable for non-linear systems such as particles moving in a magnetic field.

First, a model of a charged track moving across the SAND detector was implemented and then validated. This involved the reconstruction of ideal (no energy loss nor scattering) simulated trajectories of varying lengths within a magnetic field. Both the energy loss and multiple scattering effects were then integrated, to validate the algorithm within the detector geometry and assess the correct implementation of

these corrections. The performed test shown an agreement between the simulated and reconstructed energy losses within 15%.

Then, a test was performed on realistic simulated muon trajectories, including both the energy loss and the scattering. The results showed that the implemented algorithm was able to correctly predict the trajectories. The position and direction in the horizontal plane are predicted with bias compatible with 0 and resolution compatible with that expected of the real STT, 200 μm and 0.2 rad respectively. On the vertical plane, similar results are obtained for the particle direction, while the predicted position have a 7% bias. The source of this bias remains under study, with the main hypothesis being Coulomb scattering.

In the final stage of this study, a comprehensive simulation of the SAND detector using the GEANT4 toolkit was employed to evaluate the algorithm performance in reconstructing ν_μ CC events. For each simulated interaction, only muons, pions, and protons produced at the vertex were considered and selected requiring a minimum of 10 hits and containment of the vertex within the fiducial volume. For each selected particle, the starting point, direction and momentum were reconstructed by applying the KF algorithm. For all particle types, the position was reconstructed with a residual distribution having $\mu_{xy} < 4 \times 10^{-5}$ m and an RMS < 0.003. The direction on the horizontal plane was found to have a residual distribution with $\mu_{tan\lambda} < 0.004$ and RMS < 0.05, while the vertical direction has $\mu_\phi < 0.001$ rad and RMS < 0.04. The reconstructed momentum resolution depends, however, on the particle type and was found to be between 5% and 8%. A preliminary vertexing algorithm was then applied to the reconstructed trajectories to obtain the position of the vertex. A resolution <3 mm was found for the x and y coordinates, while the z coordinated has a resolution of about 5 mm.

Despite the results being within the STT requirements, further improvements and expansions are needed, with the primary ones being the removal of the use of MC information, and the addition of the reconstructed data of the other SAND components (GRAIN and ECAL) to perform a full reconstruction of the neutrino energy.

Appendix A

Results for π^+ and p

In this appendix, the plots of the recontructed position and direction of pions and muons are reported in Fig. A.1 and A.2 respectively. The left column shows each reconstructed quantity (x, y, $\tan\lambda$, ϕ) as a function of the corresponding true values. On the right column, the distributions of the residuals for the same quantities are instead shown. These plots refers to the results previously shown in Table REF.

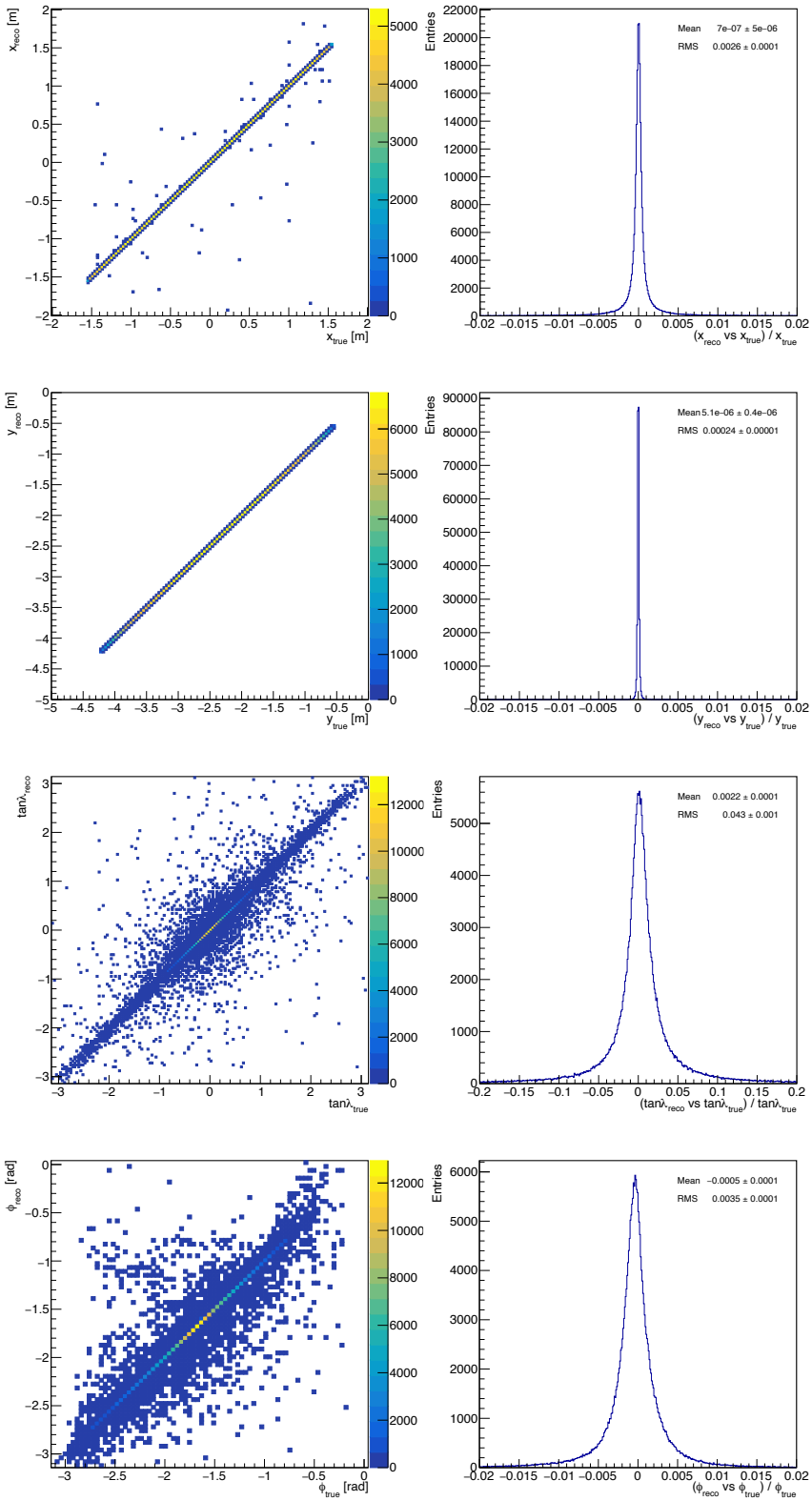

Figure A.1: From top to bottom: x, y, $\tan\lambda$, and ϕ reconstructed quantities for the selected pions. Left: reconstructed quantities as a function of the true ones. Right: relative residuals of each reconstructed quantity.

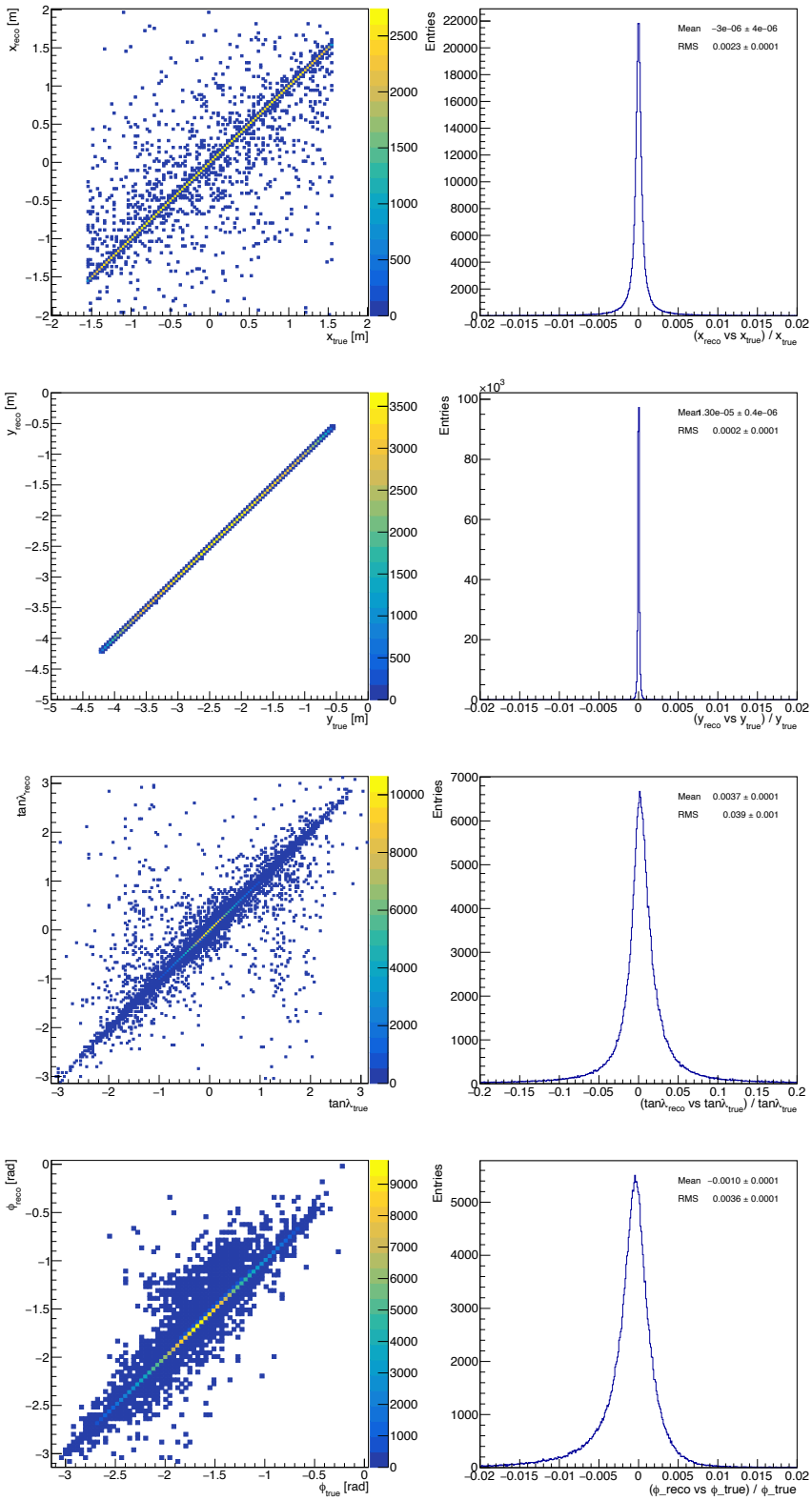

Figure A.2: From top to bottom: x, y, $\tan\lambda$, and ϕ reconstructed quantities for the selected protons. Left: reconstructed quantities as a function of the true ones. Right: relative residuals of each reconstructed quantity.

Bibliography

[1] B. Kaiser. "Neutrino Physics". In: *Proceedings of eConf C040802*. 2004. arXiv: hep-ph/0506165.

[2] *KATRIN experiment*. Accessed: 2024-05-31. URL: https://www.katrin.kit.edu/.

[3] M. Thomson. *Modern Particle Physics*. New York: Cambridge University Press, 2013.

[4] KamLAND Collaboration. "Measurement of neutrino oscillation with KamLAND: Evidence of spectral distortion". In: *Physical Review Letters* 94 (2005), p. 081801. arXiv: hep-ex/0406035.

[5] K.Abe et al. "The T2K experiment". In: *Nuclear Instruments and Methods in Physics Research Section A: Accelerators, Spectrometers, Detectors and Associated Equipment* 659.1 (2011), pp. 106–135. ISSN: 0168-9002. DOI: 10.1016/j.nima.2011.06.067. URL: http://dx.doi.org/10.1016/j.nima.2011.06.067.

[6] M. A. Acero et al. "Search for CP-violating Neutrino Non-Standard Interactions with the NOvA Experiment". In: (Mar. 2024). arXiv: 2403.07266 [hep-ex].

[7] K.Abe et.al. "Constraint on the matter–antimatter symmetry-violating phase in neutrino oscillations". In: *Nature* 580.7803 (Apr. 2020), pp. 339–344. ISSN: 1476-4687. DOI: 10.1038/s41586-020-2177-0. URL: http://dx.doi.org/10.1038/s41586-020-2177-0.

[8] *Deep Underground Neutrino Experiment (DUNE)*. Accessed: 2024-05-31. URL: https://www.dunescience.org/.

[9] L. Wolfenstein. "Neutrino oscillation in matter". In: *Physical Review D* 17.9 (1978), pp. 2369–2374.

[10] Michael S. Turner. *Cosmology and Particle Physics*. 1986.

[11] *Super-Kamiokande Experiments*. Accessed: 2024-05-31. URL: http://www-sk.icrr.u-tokyo.ac.jp/sk/index-e.html.

[12] *Sudbury Neutrino Experiment (SNO)*. Accessed: 2024-05-31. URL: https://sno.phy.queensu.ca/.

[13] Zhiyuan Chen. *Latest results from Daya Bay using the full dataset*. 2023. arXiv: 2309.05989 [hep-ex]. URL: https://arxiv.org/abs/2309.05989.

[14] J. et al. Ahn. "Observation of Reactor Electron Antineutrinos Disappearance in the RENO Experiment". In: *Physical Review Letters* 108.19 (2012). ISSN: 1079-7114. DOI: 10.1103/physrevlett.108.191802. URL: http://dx.doi.org/10.1103/PhysRevLett.108.191802.

[15] Bruce T. Cleveland and Raymond Davis et al. Timothy Daily. "Measurement of the Solar Electron Neutrino Flux with the Homestake Chlorine Detector". In: *The Astrophysical Journal* 496.1 (Mar. 1998), p. 505. DOI: 10.1086/305343. URL: https://dx.doi.org/10.1086/305343.

[16] *SAGE Gallium Solar Neutrino Experiment*. Accessed: 2024-05-31. URL: https://inspirehep.net/experiments/1109179.

[17] *GALLEX Experiment*. Accessed: 2024-05-31. URL: https://inspirehep.net/experiments/1109244.

[18] Oleg Kalekin and (on behalf ofthe ANTARES collaboration). "The ANTARES underwater neutrino telescope". In: *Journal of Physics: Conference Series* 160.1 (2009), p. 012036. DOI: 10.1088/1742-6596/160/1/012036. URL: https://dx.doi.org/10.1088/1742-6596/160/1/012036.

[19] A. Achterberg et. al. "First year performance of the IceCube neutrino telescope". In: *Astroparticle Physics* 26.3 (2006), pp. 155–173. ISSN: 0927-6505. DOI: https://doi.org/10.1016/j.astropartphys.2006.06.007. URL: https://www.sciencedirect.com/science/article/pii/S0927650506000855.

[20] M. et al. Ahn. "Measurement of neutrino oscillation by the K2K experiment". In: *Phys. Rev. D* 74 (Oct. 2006). DOI: 10.1103/PhysRevD.74.072003. URL: https://link.aps.org/doi/10.1103/PhysRevD.74.072003.

[21] P. et al. Adamson. "Combined Analysis of ν_μ Disappearance and $\nu_\mu \to \nu_e$ Appearance in MINOS Using Accelerator and Atmospheric Neutrinos". In: *Phys. Rev. Lett.* 112 (2014). DOI: 10.1103/PhysRevLett.112.191801. URL: https://link.aps.org/doi/10.1103/PhysRevLett.112.191801.

[22] N Tolich and the SNO collaboration. "Final results from SNO". In: *Journal of Physics: Conference Series* 375 (2012). DOI: 10.1088/1742-6596/375/1/042049. URL: https://dx.doi.org/10.1088/1742-6596/375/1/042049.

[23] *NuFit*. Accessed: 2024-05-31. 2024. URL: http://www.nu-fit.org/.

[24] B. Abi et al. *Deep Underground Neutrino Experiment (DUNE), Far Detector, Volume II: DUNE Physics*. Tech. rep. Jan. 2020. arXiv: 2002.03005.

[25] B. Abi et al. *Deep Underground Neutrino Experiment (DUNE) Near Detector Conceptual Design Report*. Tech. rep. Mar. 2023. arXiv: 2103.13910.

[26] B. Abi et al. *Deep Underground Neutrino Experiment (DUNE), Far Detector, Volume III: DUNE Far Detector Technical Coordination*. Tech. rep. Jan. 2020. arXiv: 2002.03008.

[27] B. Abi et al. *Deep Underground Neutrino Experiment (DUNE), Far Detector, Volume I: Introduction to DUNE*. Tech. rep. Jan. 2020. arXiv: 2002.02967.

[28] G.Adamov et al. *A Proposal to enhance the DUNE Near-Detector Complex*. 2019.

[29] D.E. Andrews et al. *Progress in the Design and Manufacture of the FLOE Solenoid for the DaΦne ring at Frascati*. Tech. rep. in proceedings of the 1997 Particle Accelerator Conference, pp. 3413-3415 vol. 3, 1997. DOI: 0.1109/PAC.1997.753226.

[30] DUNE Collaboration. *Deep Underground Neutrino Experiment (DUNE) Near Detector Conceptual Design Report*. Tech. rep. 2021. arXiv: 2103.13910.

[31] V.Pia. "Reconstruction of neutrino interactions in SAND with an innovative liquid Argon imaging detector". In: *JINST* 19.02 (2024), p. C02073. DOI: 10.1088/1748-0221/19/02/C02073.

[32] S. N. Gninenko. "MiniBooNE Anomaly and Heavy Neutrino Decay". In: *Physical Review Letters* 103.24 (2009). ISSN: 1079-7114. DOI: 10.1103/physrevlett.103.241802. URL: http://dx.doi.org/10.1103/PhysRevLett.103.241802.

[33] P. Abreu et al. "Performance of the DELPHI detector". In: *Nuclear Instruments and Methods in Physics Research Section A: Accelerators, Spectrometers, Detectors and Associated Equipment* 378 (1996), pp. 57–100. DOI: https://doi.org/10.1016/0168-9002(96)00463-9.

[34] Keisuke Fujii. *Extended Kalman Filter*.

[35] Matteo Tenti. *Extended Kalman Filter for SAND*.

[36] Gerald R. Lynch and Orin I. Dahl. "Approximations to multiple Coulomb scattering". In: *Nuclear Instruments and Methods in Physics Research Section B: Beam Interactions with Materials and Atoms* 58 (1991), pp. 6–10. ISSN: 0168-583X. DOI: https://doi.org/10.1016/0168-583X(91)95671-Y.

[37] M. Alam et al. *GENIE Production Release 2.10.0*. 2015. arXiv: 1512.06882.

[38] INFN Bologna. *edep-sim output*.

[39] *Fermilab*. Accessed: 2024-05-31. URL: https://www.fnal.gov/.

[40] C. Giunti and Chung W. Kim. *Fundamentals of Neutrino Physics and Astrophysics*. New York: Oxford University Press, 2007.

[41] V. Pia. "Study of the calorimetric performance of a liquid Argon detector based on a novel optical imaging concept". PhD thesis. Università di Bologna, 2023. DOI: 10.48676/unibo/amsdottorato/10933.

[42] B. Pontecorvo. "Neutrino Experiments and the Problem of Conservation of Leptonic Charge". In: *JETP* 26 (1968), pp. 984–988.

[43] V. Barger, D. Marfatia, and K. Whisnant. *The Physics of Neutrinos*. Princeton University Press, 2012. ISBN: 978-0-691-12853-5.

[44] C. Giganti and S. Lavignac. "Neutrino oscillation: the rise of PMNS paradigm". In: *Universe* 3.1 (2017), p. 27. arXiv: 1710.00715.

[45] L. Maiani and O. Benhar. *Relativistic Quantum Mechanics*. Cambridge University Press, 2005. ISBN: 978-0-521-52737-0.

[46] A. Bizzeti. "Dispense Oscillazione dei neutrini". PhD thesis. Università degli Studi di Modena, 2007.

[47] Aravind E Vijayan. *Introduction to Kalman Filter and Extended Kalman Filter*. 2014. DOI: 10.13140/2.1.4010.4648.

[48] N. et al. Agafonova. "Discovery of τ Neutrino Appearance in the CNGS Neutrino Beam with the OPERA Experiment". In: *Phys. Rev. Lett.* 115 (2015). DOI: 10.1103/PhysRevLett.115.121802. URL: https://link.aps.org/doi/10.1103/PhysRevLett.115.121802.